The University of Osaka
Institutional Knowledge Archive

Title	Calculation of Ship Hull Fatigue Damage caused by Local Ice Loads in Ice-covered Waters
Author(s)	韓, 月
Citation	大阪大学, 2018, 博士論文
Version Type	VoR
URL	https://doi.org/10.18910/70770
rights	
Note	

The University of Osaka Institutional Knowledge Archive : OUKA

https://ir.library.osaka-u.ac.jp/

The University of Osaka

Doctoral Dissertation

Calculation of Ship Hull Fatigue Damage caused by Local Ice Loads in Ice-covered Waters

Han　Yue

July 2018

Department of Naval Architecture and Ocean Engineering
Division of Global Architecture
Graduate School of Engineering
Osaka University

Abstract

Fatigue damage for ships navigating in ice-covered waters can pose a threat to the safety of human life and ship hull, and cause pollutant to the environment. The estimation method of fatigue damage due to ice actions has not been established. To date, fatigue damage evaluation is carried out based on field measurements of limited ship types and ice conditions. However, the field measurements are usually incomplete. For that reason, it is difficult to provide guidance for the design of new structural components or new ship routes. In order to solve this problem, numerical simulation can be used to evaluate fatigue damage due to ice actions, instead of field measurements. In the present research, simulation methods are developed to obtain time histories of ice-induced loads for ships operating in level ice, pack ice and ridge ice, which are applied to estimate fatigue damage. The thesis is composed of the following chapters.

Chapter 1 gives the literature review of ice loads and fatigue damage calculation methods for ice-going ships. Numerical methods to estimate time series of ice loads in level ice, ridge ice and pack ice, and fatigue evaluation method due to ice actions, have not been established. The objectives and significance of this study are shown.

Chapter 2 concerns the solution of ship motions using a step-by-step numerical integration. The coupling problem between ship motions and excitation forces and moments is solved by weak coupled iteration.

Chapter 3 deals with the numerical model for ship operating in level ice. The global and local loads on ship hulls are estimated by the proposed model, and statistic of ice-induced stress is obtained. The numerical model is validated by comparing the simulated results against field measurement stress. Instead of field measurements, the proposed model makes it possible to estimate the statistical distribution of ice-induced loads in level ice for fatigue damage calculation, based on numerical simulations.

Chapter 4 introduces a numerical method to predict the ice-induced loads on ice-going ships in ridged ice fields. Probabilistic ice fields are generated on the basis of field observation. A modified Rankine's plasticity model is proposed to achieve the ice-induced loads in ridge ice. The proposed numerical model has improved the earlier models of ship–ice interaction in ridge ice, which is only applicable to global ice loads. As a result, local ice loads, which is difficult to obtain by far, can be achieved.

Chapter 5 relates to numerical model for ship navigating in pack ice. The ice floes are represented as hundreds of circular disks with random sizes. Ship–ice collisions and ice–ice contacts are modeled with discrete element method. Global and local ice loads are obtained by the proposed model in various ice conditions (ice thickness, floe radius, ice concentration), and statistic of ice-induced stress is analyzed. The numerical model

is validated by comparing the simulated stress against field results. The statistical distribution of ice loads in pack ice for fatigue damage calculation can be estimated based on the proposed numerical method, instead of field measurements.

Chapter 6 conducts a case example of fatigue damage calculation based on the simulated ice loads obtained using the numerical models in Chapter 3 to Chapter 5. The long-term statistic of ice loads is approximated by the Weibull distribution. Fatigue stress between frames of plate structure at bow shoulder area due to distributed ice loads is found using structural beam theory. Ice loads in each stationary ice condition (level ice, ridge ice, and pack ice) are calculated. Fatigue damage is estimated based on the Palmgren–Miner cumulative damage rule. The fatigue damage result is validated by comparing with that calculated based on field measurements. As a result, it is clarified for the first time that fatigue damage of ship hull induced by ice loads can be estimated based on ice loads obtained from numerical simulations, instead of field data.

Chapter 7 summarizes the conclusions of the main points in this study, and provides several recommendations for future work.

Contents

Abstract 1

Nomenclature 6

1 Introduction 15

1.1 Background and motivation 15

1.2 Literature review 16

1.2.1 On numerical methods in level ice fields 16

1.2.2 On numerical methods in ridged ice fields 17

1.2.3 On numerical methods in pack ice fields 18

1.2.4 On fatigue damage calculation 18

1.3 Thesis outline 19

2 Solution of Motion Equations 21

2.1 Motion equations 21

2.1.1 Reference frames 21

2.1.2 Newmark-beta method 23

2.2 Excitation forces 24

2.2.1 Propeller and rudder forces 24

2.2.2 Hydrodynamic forces 25

2.2.3 Euler forces 26

2.2.4 Ice forces 27

3 Numerical Model of Ship Operating in Level Ice fields 29

3.1 Ship–ice interaction mechanics in level ice fields 29

3.1.1 Contact detection 31

3.1.2 Crushing force 33

3.1.2.1 Contact area 33

3.1.2.2 Pressure–area relation 37

3.1.3 Bending failure 37
3.1.3.1 Contact force analysis 37
3.1.3.2 Bending failure criterion 39
3.1.3.3 Geometry of ice wedge idealization 41
3.2 Numerical results of ice loads in level ice fields 42
3.2.1 Global ice loads and ship performance 42
3.2.2 Local ice-induced loads and statistical analysis 48
3.2.2.1 Local ice-induced loads 48
3.2.2.2 Statistical analysis 50
3.3 Summary 54
4 Numerical Model of Ship Operating in Ridged Ice Fields 55
4.1 Generating ridged ice fields 55
4.1.1 Geometry of sea ice ridges 55
4.1.2 Distribution of sail heights and ridge spacings 56
4.2 Ship–ice interaction mechanics in ridged ice fields 58
4.2.1 Theoretical formula of Keinonen 58
4.2.2 Theoretical formula of Mellor 62
4.2.3 Theoretical formula of Malmberg 64
4.2.4 A modified Rankine model in the present study 65
4.3 Numerical results of ice loads in ridged ice fields 68
4.3.1 Global ice loads and ship performance 68
4.3.2 Local ice-induced loads and statistical analysis 72
4.3.2.1 Local ice-induced loads 72
4.3.2.2 Statistical analysis 73
4.4 Summary 76
5 Numerical Model of Ship Operating in Pack Ice Fields 77
5.1 Ship–ice interaction mechanics in pack ice fields 77
5.1.1 Contact detection 77
5.1.2 Contact force 79
5.1.2.1 Ice–ice contact 79

5.1.2.2 Ship–ice contact 81
5.1.3 Motion of ice floes 81
5.2 Numerical results of ice loads in pack ice fields 81
5.2.1 Global ice loads and ship performance 82
5.2.2 Statistical analysis of local ice-induced loads 86
5.3 Summary 90
6 Fatigue Damage Calculation 91
6.1 Fatigue damage calculation 91
6.1.1 Structural response 91
6.1.2 Impact frequency 93
6.1.3 Fatigue damage expression 94
6.2 Case example 95
6.2.1 Ice data 95
6.2.2 Fatigue damage calculation 96
6.2.2.1 Local ice-induced stress 96
6.2.2.2 Calculation result of fatigue damage 102
6.3 Summary 106
7 Conclusions and Future Work 107
7.1 Conclusions 107
7.2 Future works 109
ACKNOWLEDGEMENTS 111
REFERENCES 112

Nomenclature

Symbols

A	added mass matrix	
A	projection of contact area on the water plane	m^2
A_c	critical area	m^2
A_{cr}	contact area	m^2
A_f	ice floe area	m^2
A_r	rudder area	m^2
a	side length of cells	m
B	damping matrix	
B	ship breadth	m
C	restoring force matrix	
C	ice concentration	
$C_D(x)$	drag coefficient for cross-flow at location x	
C_{D0}	surface friction	
C_d	drag coefficient of water	
C_d'	rotational drag coefficient	
C_f	empirical coefficient	
C_L & C_D	lift and drag coefficient of the rudder	
C_l	empirical parameter	
C_m	additional mass coefficient	
C_p	empirical parameter	
C_Q	resistance coefficient	
C_v	empirical parameter	
c	parameter for plotting position	
D	total fatigue damage	

$D(x)$	sectional draught at location x	m
D_j	fatigue damage in a stationary condition	
D_p	empirical parameter	
d	keep spacing	m
E	the Young's modulus of ice	MPa
$\mathbf{F}$	excitation forces and moments	
$\mathbf{F}^{\mathrm{brk}}$	icebreaking force	
$\mathbf{F}^{\mathrm{Euler}}$	Euler force	
$\mathbf{F}^{\mathrm{ice}}$	forces arising from ice	
$\mathbf{F}^{\mathrm{ow}}$	forces arising from open water	
$\mathbf{F}^{\mathrm{p}}$	forces arising from propeller and rudder	
$\mathbf{F}_{\mathrm{G}}$	buoyancy force	kN
$\mathbf{F}_{\mathrm{S}}$	shear friction resistance	kN
$\mathbf{F}\tau_0$	cohesion resistance	kN
$\mathbf{F}_{\mathrm{TOT}}$	force against the wall	kN
F_{cr}	crushing force	kN
F_d & M_d	water drag force and rotational drag moment of ice floe	
f_1	frictional force	kN
$\vec{f}$	external force	kN
h	wall height	m
h_{c}	cut-off height t of sail heights	m
h_{eq}	equivalent ice thickness	m
h_i	ice thickness	m
h_k	keel depth	m
h_L	ice thickness limit	m
h_l	load height	m
$h_r(x)$	ridge depth at location x	m
h_s	sail height	m
h_t	trapezium altitude	m

I	moment of inertia	kgm^2
I_x & I_y	integer cell numbers in the x and y directions	
$ICELL$	cell number of the current disk	
K & m	constants of S–N curve	
K_0	coefficient of lateral stress	
K_{ne}	normal contact stiffness	kN/m
K_{nv}	normal contact viscosity	kNs/m
K_p	passive pressure coefficient	
K_{te}	tangential contact stiffness	kN/m
k	shape parameter of loads distribution	
k_{pen}	a factor	
L_{bow}	bow length	m
L_c	crushing depth	m
L_H	length of trapezium base	m
L_h	crushing width	m
L_{par}	length of parallel midship	m
L_{WL}	ship waterline length	m
l	characteristic length of the ice	m
l_{br}	length	m
l_f	frame span	m
$\mathbf{M}$	mass matrix	
M_a	additional mass of ice floe	kg
m_0	boundary condition	
m_g	mass	kg
$\vec{m}$	external moment	kNm
N	a factor	
N_0	total number of stress amplitudes	
N_i	number of amplitudes to failure for a constant stress S_i	
$NCELL$	number of cells	
$\vec{n}$ & $\vec{\tau}$	unit vectors of the normal axis and tangential axis respectively	

n_i	number of stress amplitudes	
n_s	number of stress magnitudes	
$\dot{O}_i$ & $\dot{O}_j$	linear velocity for disks i and j	m/s
P_f	bearing capacity	kN
P_{ice}	the ice load	kN/m
p	porosity of ridges	
p_{av}	average crushing pressure	MPa
q & r	shape parameter and scale parameter of stress distribution	
$\boldsymbol{R}_b^n$	rotation matrix for linear velocity	
R	total horizontal force per unit width	kN/m
R'	normal force for an indeterminate stress state	kN/m
R_{B}	bending resistance	kN
R_{b}	total resistance on ship bow	kN
R_{C}	crushing resistance	kN
R_f & R_l	icebreaking radius at the first and last contact node	m
R_I	icebreaking radius	m
R_i and R_j	radius of disks i and j	m
R_{k}	total keel resistance	kN
R_{level}	level ice resistance	kN
R_{m}	midbody resistance	kN
R_{max}	maximum disk radius	m
R_n	Reynolds number	
R_{pB}	bottom frictional resistance	kN
R_{pS}	side frictional resistance	kN
R_{r}	total pure ridge resistance	kN
R_{s}	submersion component	kN
$R_{\gamma 1}$	upper shear plane force	kN
$R_{\gamma 2}$	lower shear plane force	kN
R_{ε}	end shear plane force	kN

$\mathbf{r}$	displacement vector	
S_{wet}	wetted surface area	m^2
S	ice-induced stress	MPa
s	frame spacing	m
$\boldsymbol{T}_{\Theta}(\boldsymbol{\Theta}_{nb})$	transformation matrix for angular velocity	
T	ship draft	m
T_B	bollard pull	t
T_{net}	net thrust	kN
t_k	the *kth* time step	
U	randomly generated number	
u	forward velocity component	m/s
$\boldsymbol{V}_i$ and $\boldsymbol{V}_w$	velocity vectors of ice floe and water	
V_{sub}	submerged area of the floe	m^2
$\boldsymbol{v}_{b/n}^{b}$	velocity vector in the body-fixed frame	m/s
$\boldsymbol{v}_{b/n}^{n}$	velocity vector in the earth-fixed frame	m/s
$v(x)$	transverse velocity component at location x	m/s
v_1	relative velocity component on the contact surface	m/s
v_f	flow velocity	m/s
v_{ow}	open water speed	m/s
v_{pen}	penetration velocity	m/s
$x_{\min}$ & $x_{\max}$	coordinate of extreme points of the cell domain on the x axis	
x_r	rudder location	m
$y_{\min}$ & $y_{\max}$	coordinate of extreme points of the cell domain on the y axis	
Z	section modulus	cm^3
Z'	ratio	
z	depth	m
α	normal frame angle of the ship hull	deg.
α'	attack angle	deg.
α_k	keel angle	deg.

α_s	sail angle	deg.
α_{stall}	stall angle	deg.
β	waterline angle	deg.
β_N	parameter	
γ	angle	deg.
γ'	inclination angle of rupture plane	deg.
γ_w	specific weight of water	kN/m^3
Δ_{ij}	distance between the two disk centers	m
δt	time interval	s
δ_n^i	normal indentation of overlap	m
$\dot{\delta}_n^i$	relative velocity of the two disks at normal direction	m/s
$\dot{\delta}_t^i$	relative velocity of the two disks at tangential direction	rad/s
ε	scale parameter of loads distribution	
η	stem angle	deg.
$\dot{\mathbf{\Theta}}_{nb}$	Euler rate vector	rad/s
θ, φ & ψ	Euler angles of pitch, roll and yaw respectively	rad
θ'	angle from x-axis to the vector $\vec{n}$	deg.
Λ	aspect ratio	
λ	shape factor of sail heights distribution	
λ_N	parameter	
μ	shape parameter of keel spacings distribution	
μ_i	friction coefficient	
μ_t & σ_t	mean value and standard deviation of ice thickness	
μ_c & σ_c	mean value and standard deviation of $ln(C)$	
υ	Poisson's ratio	
υ_d	number of events per nautical mile	1/nm
ξ	convergence criterion	
ρ_{ice}	sea ice density	kg/m^3

ρ_w	sea water density	kg/m^3
$\rho_\triangle$	difference of the densities of sea water and ice	kg/m^3
σ	normal stress	MPa
σ_b	bending strength	MPa
σ_{cr}	crushing strength	MPa
σ_f	flexural strength	MPa
σ_U	flexural strength of ice in upward bending	MPa
τ	actual shear strength	MPa
τ_0	cohesion	MPa
ϕ	opening angle of ice wedge	deg.
ϕ'	internal friction angle	deg.
ω	floe rotational velocity	rad/s
$\boldsymbol{\omega}_{b/n}^{b}$	angular velocity vector in body-fixed frame	rad/s
ω_i & ω_j	angular velocities of disks *i* and *j*	rad/s

Acronyms

2D	two-dimensional
3D	three-dimensional
CDF	cumulative distribution function
DOF	degree of freedom
DEM	discrete element method
FEM	finite element method
GEM	GPU-Event-Mechanics
PDF	probability density function

Subscript

1-6	corresponding degree of freedom
x, y, z	in *x*-, *y*-, *z*-directions, respectively

m	mean value
sd	standard deviation
n, τ	in normal and tangential directions, respectively

Chapter 1

Introduction

1.1 Background and motivation

Recently, increasing ships such as oil tankers and LNG carriers are navigating through the ice-covered oceans, due to the expected growth of oil and gas related activity in the cold regions. Different from open waters, the presence of ice poses the greatest challenge to the design and operation of ice-going ships, which has led to extensive research on better understanding of ship–ice interaction, vessels' performance and hull damages in ice-covered waters.

For ships navigating in ice-infested regions, ice loads represent the dominant loads. From the fatigue point of view, the sea ice and ship interact in a repetitive manner and ice-going ships are operating under cyclic impact loads caused by the ice. The ice loading potentially induces stress amplitudes that could give rise to micro-cracks. Damage can entail oil leakage or even catastrophic failure, threatening overall structural safety. The leakage of petroleum and natural gas would cause serious pollution to the environment in ice waters, because any contaminant decomposition process runs very slowly due to the extreme cold, extensive ice cover and reduced sunlight.

As mentioned above, fatigue damage because of ice actions is an important issue for ships operating in the harsh environment of ice-covered waters. Nevertheless, research into fatigue damage caused by ice action has not been developed well compared with wave action. To date, most studies of fatigue damage caused by ice-induced loads have been conducted using field measurements. However, the field measurements are usually considerably limited and incomplete. For that reason, it is difficult to evaluate fatigue damage correctly and to provide guidance for the design of new structural components or new ship routes. Compared to field measurements, the ice conditions and ship hull can be easily varied in a numerical simulation, which is useful to complement the lack of ice load data in some regions, or to predict the fatigue life for new structures when only ice condition data are needed. The numerical method appears promising to evaluate fatigue damage.

Ships navigating in ice-covered waters can encounter widely diverse ice conditions due to the possible operation over a large geographical area. Those ice conditions can include pack ice, level ice, ridged ice, etc. A typical sea ice field involving different ice

types is presented in Fig. 1.1.

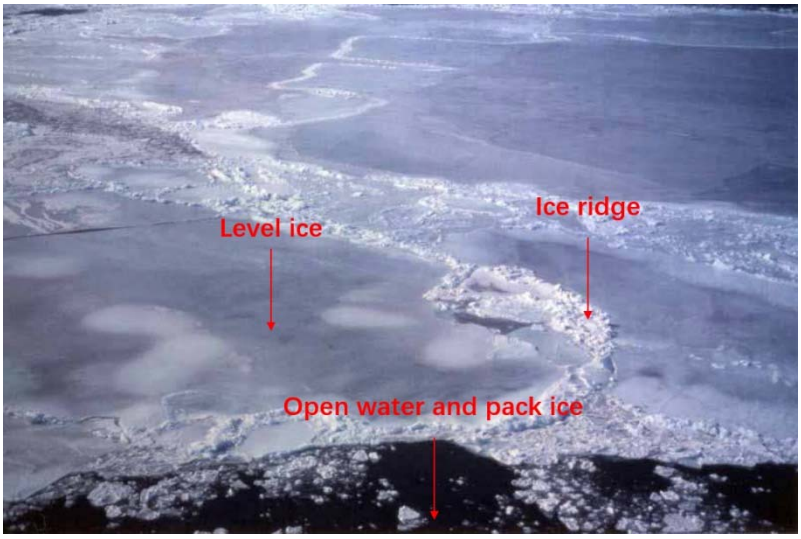

Fig. 1.1 A typical sea ice field including various ice types [1].

As a result, cases of fatigue damage calculation should also contain various ice conditions. Therefore, numerical programs for modeling ship–ice interaction process in different ice types are in demand in order to produce the required data for fatigue damage estimation. These numerical models should be developed as realistically as possible, and meantime, the computation efficiency needs to be considered as well. Ice-induced fatigue stress is achievable based on numerical simulations, and statistical analysis of ice stress can be made. Furthermore, by applying the long term conditional statistics, the prediction of accumulated fatigue damage in the local components of a ship hull can be performed.

1.2 Literature review

1.2.1 On numerical methods in level ice fields

It is challenging to predict the ice loads encountered by a ship transiting in an intact ice field. Early research on the level ice resistance was usually carried out based on break-displace process and the superposition of several force components to the total resistance was widely accepted. These models can be found for example in Enkvist [2], Lewis et al. [3], Lindqvist [4] and Riska et al. [5].

In the past decades, efforts have been made to improve the numerical model of ice–hull interaction in level ice from a time domain point of view. For instance, Izumiyama et al. [6] developed a simulation method for an advancing level ice acting on a fixed conical structure based on the plastic limit theory, and the sizes of the broken ice floes were assumed to be random, following a normal distribution. Wang [7] employed a similar strategy, and presented a numerical procedure using geometric grid method to simulate the continuous ice–cone contact based on the mechanics of crushing-bending failure

model. This approach was then followed by many researchers, such as Nguyen et al. [8], Sawamura et al. [9], and Zhou et al. [10]. Su et al. [11] [12] established a simulation program to reproduce the observed icebreaking patterns and the continuous ice loading processes in a uniform level ice and the ice with randomly varying thickness and strength properties, partly based on the empirical data. This model was conducted involving the surge, sway and yaw motions. Tan et al. [13] extended Su's planar model to a 6-degree-of-freedom (DOF) model. The fully coupled motions of the ship were considered for 6 DOFs together with the corresponding environmental forces. A further study on the effect of dynamic bending of level ice during ship–ice interaction was carried out with this 6-DOF model by Tan et al. [14]. Zhou and Peng [15] improved Su's 3-DOF numerical model, by taking the ice plate flexural deflection into consideration, and an adjustment factor of contact surface was derived.

Moreover, a numerical real-time simulator for ship–ice interaction was developed by Lubbad et al. [16]. In the presented model, level and broken ice features were studied. These updated state variables of ship model as well as the fragmenting ice are displayed by the Visual System.

Recently, the discrete element method (DEM) has also been applied in the numerical models in level ice. Lau et al. [17] conducted a wide range of ice–structure and ice–ship interaction simulations using a commercial code DECICE. Compared with experimental data, the simulations were found satisfactory in terms of accuracy and real-time simulation capability.

1.2.2 On numerical methods in ridged ice fields

The methods of calculating the ice loads induced by ridge keels have been based largely on ideas borrowed from theories of soil mechanics such as Coulomb's theory and Rankine's theory. Keinonen [18] considered ridges as unconsolidated with a constant thickness and proposed an analytical method to calculate the pure ridge resistance based on Coulomb's method. Mellor [19] employed Rankine's theory to achieve the ship resistance in thick brash ice, which is similar to the unconsolidated ridge considered by Keinonen [18]. In addition, the resistance formula derived by Malmberg [20] is used extensively in ridged ice section of transit models, which simulates the ship's performance in various ice conditions along specific routes. These analytical methods are used widely to obtain the global ice loads caused by ridge keels.

There have been a few studies of ridge interaction failure using the finite element method (FEM). For example, Sand and Horrigmoe [21] was devoted to the development of numerical simulation techniques by means of nonlinear finite element analysis to obtain ice ridge forces on upward and downward bending cones. The finite element spatial discretization procedure is adopted for the ice ridge and the surrounding ice sheet as well as the structure.

Furthermore, DEM is applied to model the interaction between ships and ice ridge in recent studies. In fact, the method is useful to obtain both global and local ice loads.

Hisette et al. [22] and Gong et al. [23] simulated the ship–keel interaction using a three-dimensional (3D) DEM with ice pieces represented by polyhedral particles, but such computations can be time consuming even for a single ice ridge. Based on the background presented above, it remains a very difficult task, both numerically and experimentally, to estimate the local ice load on ship hulls in ice fields containing multiple ridges.

1.2.3 On numerical methods in pack ice fields

DEM has attracted much attention in order to describe the interaction between ship hull and pack ice floes. For instance, Hansen and Løset [24] [25] proposed a two-dimensional (2D) DEM model for theoretical investigation of behavior of a mooring turret in broken ice. In the model, each ice floe is represented by a circular disk. Disk–disk or disk–structure collisions are modelled as linear viscous-elastic, or as a Coulomb friction contact in case of relative tangential sliding. Analogous approaches were adopted by Karulin and Karulina [26] and Dai and Peng [27] as well. Ji et al. [28] improved the previous method and modelled the ice floes with 3D dilated disk elements, and the ship hull was modelled with 3D disks with overlaps.

Daley et al. [29] [30] employed a GPU-Event-Mechanics (GEM) approach to assess vessel performance in pack ice, in which the ice floes were represented as 2D convex polygons and the vessel was treated as an auto pilot model with constant thrust. The parallel computing power of GPU enabled the computation of large scale system involving a large number of bodies.

A commercial DEM software of DECICE has also been extensively used to address the interaction problems in pack ice. It uses discrete elements in an explicit time domain solver. Each element undergoes rigid body translation and rotation according to Newtonian mechanics. Zhan et al. [31] applied the DECICE code to investigate the problems of turning circle and Zig-Zag maneuvers in pack ice. Zhan and Molyneux [32] later extended the algorithm into a DECICE 3D model.

Moreover, physics engines were used for simulation of the floater-ice interaction in broken ice. Physics engine generally means a software system to simulate the dynamics of generic multibody systems with contacts and friction. This approach was pioneered by Konno and Mizuki [33], which used the Open Dynamics Engine to simulate a model icebreaker in a broken-ice field. Metrikin et al. [34] adopted another physics engine Phys X to implement realistic, high fidelity 3D simulations of the ice-fluid-structure interaction process in broken ice. Metrikin et al. [35] further compared four publicly available physics engines (Ag X Multiphysics, Open Dynamics Engine, Phys X and Vortex) in terms of integration performance and contact detection accuracy.

1.2.4 On fatigue damage calculation

To date, fatigue damage of ship structure due to ice-induced loads has received relatively little attention. Only a few studies dealt with the fatigue damage evaluation

based on field measurement data. Zhang and Bridges [36] introduced a deterministic fatigue assessment procedure, the Ship Right FDA ICE Procedure, proposed by Lloyd's Register to assess fatigue damage of ship structure induced by ice loads. Two case studies of a LNG carrier and an oil tanker were presented. Suyuthi et al. [37] derived closed form expressions of the fatigue damage for several different statistical models of the stress amplitudes, i.e. the exponential, the Weibull, and the three-parameter exponential distributions. A particular example of fatigue damage calculation was presented, where data obtained from full scale measurement performed on board of the vessel KV Svalbard in the winter 2007 were utilized. Hwang et al. [38] analyzed fatigue damages and fatigue-life measurements on the side-shell in the bow thruster room of the Korean first icebreaking research vessel ARAON, based on the experiments during her actual voyages on August 2010 and August 2013.

1.3 Thesis outline

The primary aim of this thesis is to develop an evaluation method of fatigue damage for a ship navigating in ice-covered waters based on numerical simulations. To achieve this objective, numerical methods are developed to model ship–ice interaction in level ice, ridge ice and pack ice, respectively. Ice-induced loads of different ice conditions can be ascertained from a series of numerical simulations. The simulated results are validated preliminarily by comparison with published results of field measurements, model tests or empirical formulas. Statistical analysis is performed on ice stress, and with the knowledge of ice conditions data, an accumulated fatigue damage can be estimated based on Palmgren–Miner's rule. Numerical models can be a good candidate, instead of field measurements, in order to produce the required data for fatigue damage calculation.

The thesis is composed of the following chapters.

Chapter 1 gives the general background, motivation, state-of-the-art, objectives and organization of the study.

Chapter 2 concerns the solution of ship motions using a step-by-step numerical integration. Empirical calculation formulas for external forces and moments are introduced, and the coupling problem between ship motions and excitation forces is solved by iteration.

Chapter 3 deals with the numerical model for ship operating in level ice. A semi-empirical numerical procedure is developed to model the continuous-mode icebreaking process in level ice in 6 DOFs. The numerical global and local ice loads are discussed through results of a case study conducted in a series of different ice conditions. Ship performance and statistics of ice-induced frame loads are analyzed.

Chapter 4 introduces a numerical method to predict the ice-induced loads on ice-going ships in ridged ice fields. Probabilistic ice fields are generated according to the statistical distributions of ridge heights and spacings. A modified Rankine's plasticity

model is applied to achieve the keel loads.

Chapter 5 relates to a 2D DEM numerical model developed for simulating the interaction between drifting ice floes and a moving ship. The ice floes are represented as hundreds of circular disks with random sizes and positions. Both the ship–ice collisions and ice–ice contacts are modeled, and a viscous-elastic rheology is applied at contacts.

Chapter 6 conducts a case example of fatigue damage calculation. A Weibull statistical model is applied to represent the ice-induced stress process. The structural fatigue stress is found using structural beam theory. According to ice condition distribution (ice thickness, ice concentration, ridge properties, etc.) and a proper S-N curve, fatigue damage can be estimated based on the Palmgren–Miner cumulative damage rule.

Chapter 7 summarizes the conclusions of the main points in this study, and provides several recommendations for future work.

Chapter 2

Solution of Motion Equations

For ships navigating in ice-infested waters, ice loads represent the dominant loads, whereas aside from ice loads, ship hulls are also subjected to other excitation forces and moments, such as propeller and rudder forces, hydrodynamic forces, and fictitious forces induced by a non-uniformly rotating frame relative to the inertial frame. Ship motions and excitation forces are dependent on each other, and thus the interaction between them need to be considered in the simulation program. In this chapter, calculation formulas of the external forces and moments are introduced. Motion equations are solved by numerical integration, and the coupling problem between excitation forces and ship motions is settled by iteration at each time step until the accuracy is acceptable, by which ship–ice interaction can be modeled using a step-by-step procedure in time domain.

2.1 Motion equations

2.1.1 Reference frames

In the numerical procedure, the ship is treated as a rigid body, and two right-handed Cartesian reference frames are applied to express motions and state variables of ship and ice in the model, which are the earth-fixed coordinate system O_0–$x_0y_0z_0$ and the body-fixed coordinate system G–xyz, as illustrated in Fig. 2.1.

Earth-fixed reference frame: The coordinate plane, $x_0O_0y_0$, coincides with the calm water plane, with the z_0 axis pointing upwards. The trajectory of ship and edge geometry of ice sheet or locations of ice floes are expressed in this coordinate system. The top surface of ice is defined lying on the calm water plane for simplification. In fact, the top surface of ice is not consistent with the calm water because of the density difference between water and ice. However, the densities of sea ice and sea water are respectively set as 900 kg/m^3 and 1025 kg/m^3, consequently, the ratio of ice volume below the water to that above the water is about 9:1. The maximum ice thickness in the simulations is 1 m, and thus the error caused by this assumption is small.

Body-fixed reference frame: The hydrodynamic properties and inertial coefficients of

ship are constant with respect to this reference frame that is parallel to the principal axes of inertia of ship, and therefore, a body-fixed reference frame, *xyz*, is introduced in which the origin is aligned with the center of gravity *G* and the axes correspond to the longitudinal, transverse and vertical coordinates respectively. Linear and angular velocities and accelerations are expressed in this coordinate system.

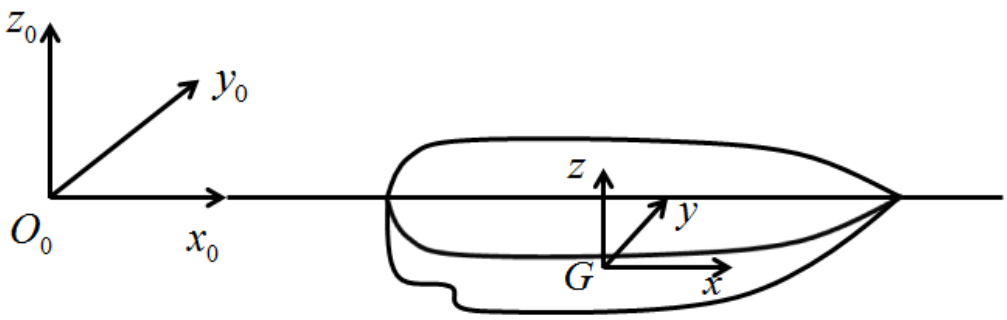

Fig. 2.1 Reference frames.

For the above reasons, the equations of motion can be solved in the body-fixed reference frame. However, it is convenient to express the position vector of ship and ice with respect to the earth-fixed reference frame, and consequently, transformations from the body-fixed frame to earth-fixed frame are necessary for modeling ship–ice interaction.

Linear velocity transformation can be written as

$$\boldsymbol{v}_{b/n}^{n} = \boldsymbol{R}_{b}^{n}\boldsymbol{v}_{b/n}^{b} \tag{2.1}$$

where $\boldsymbol{v}_{b/n}^{b}$ and $\boldsymbol{v}_{b/n}^{n}$ are the velocity vectors in the body-fixed and earth-fixed frames respectively, $\boldsymbol{R}_{b}^{n}$ represents the rotation matrix for linear velocity, which can be given by [39]

$$\boldsymbol{R}_{b}^{n}(\boldsymbol{\Theta}_{nb}) = \begin{bmatrix} \cos\psi\cos\theta & -\sin\psi\cos\varphi+\cos\psi\sin\theta\sin\varphi & \sin\psi\sin\varphi+\cos\psi\cos\varphi\sin\theta \\ \sin\psi\cos\theta & \cos\psi\cos\varphi+\sin\varphi\sin\theta\sin\psi & -\cos\psi\sin\varphi+\sin\theta\sin\psi\cos\varphi \\ -\sin\theta & \cos\theta\sin\varphi & \cos\theta\cos\varphi \end{bmatrix} \tag{2.2}$$

Therein, θ, φ, ψ are the Euler angles of pitch, roll and yaw respectively.

Angular velocity transformation can be expressed as

$$\dot{\boldsymbol{\Theta}}_{nb} = \boldsymbol{T}_{\Theta}(\boldsymbol{\Theta}_{nb})\boldsymbol{\omega}_{b/n}^{b} \tag{2.3}$$

In that equation, $\dot{\boldsymbol{\Theta}}_{nb}$ denotes the Euler rate vector, $\boldsymbol{\omega}_{b/n}^{b}$ stands for the body-fixed angular velocity vector, $\boldsymbol{T}_{\Theta}(\boldsymbol{\Theta}_{nb})$ signifies the transformation matrix for angular velocity, which is presented as [39]

$$\boldsymbol{T}_{\Theta}(\boldsymbol{\Theta}_{nb}) = \begin{bmatrix} 1 & \sin\varphi\tan\theta & \cos\varphi\tan\theta \\ 0 & \cos\varphi & -\sin\varphi \\ 0 & \sin\varphi/\cos\theta & \cos\varphi/\cos\theta \end{bmatrix} \tag{2.4}$$

2.1.2 Newmark-beta method

Ship motions, i.e. the components of velocities, accelerations, displacements and excitation forces, relating the body-fixed reference frame are governed by a general matrix form of the linear coupled differential motion equations as shown below.

$$(\mathbf{M}+\mathbf{A})\ddot{\mathbf{r}}(t)+\mathbf{B}\dot{\mathbf{r}}(t)+\mathbf{C}\mathbf{r}(t)=\mathbf{F}(t) \tag{2.5}$$

where **M**, **A**, **B**, and **C** respectively represent the mass, added mass, damping and restoring force matrices, **F** represents the excitation forces and moments, and **r** is the displacement vector of ship. No damping term is included in this simulation, for ice load is regarded as the greatest source of energy consumption, i.e. the damping coefficient **B** is assumed to be zero.

The excitation forces and moments can be decomposed into the following components as

$$\mathbf{F}=\mathbf{F}^{\text{ice}}+\mathbf{F}^{\text{p}}+\mathbf{F}^{\text{ow}}+\mathbf{F}^{\text{Euler}} \tag{2.6}$$

where superscripts 'ice', 'p', 'ow', and 'Euler' respectively designated the forces arising from the ice, propeller and rudder, open water, and a fictitious force induced using a non-uniformly rotating body-fixed frame.

A solution to equations of motion established above is obtained using a step-by-step numerical integration method. Newmark-beta method [40] is widely used to solve differential equations in numerical evaluation of the dynamic response of structures, based on an assumed variation of acceleration over a time step. The general integral equations are given by

$$\dot{\mathbf{r}}(t_{k+1})=\dot{\mathbf{r}}(t_k)+(1-\lambda_N)\ddot{\mathbf{r}}(t_k)\delta t+\lambda_N\ddot{\mathbf{r}}(t_{k+1})\delta t \tag{2.7}$$

$$\mathbf{r}(t_{k+1})=\mathbf{r}(t_k)+\dot{\mathbf{r}}(t_k)\delta t+(\frac{1}{2}-\beta_N)\ddot{\mathbf{r}}(t_k)\delta t^2+\beta_N\ddot{\mathbf{r}}(t_{k+1})\delta t^2 \tag{2.8}$$

Therein, δt stands for the time interval of numerical integration, t_k and t_{k+1} represent the *kth* and $(k+1)th$ time step respectively, the parameters β_N and λ_N are determined by the requirements related to stability and accuracy. Newmark [40] proposed that numerical damping might be introduced in the case of $\lambda_N > 1/2$, and instability can be caused in the case of $\lambda_N < 1/2$. Typically, the selection is $\lambda_N = 1/2$. In this study, the value of β_N is chosen as 1/6, which means a linear acceleration is assumed within each time interval. By the assumption of linear acceleration, the continuity of motion and state variables

of ship can be ensured, and meantime, a relatively high accuracy is achieved.

Substituting λ_N = 1/2 and β_N = 1/6 into Eqs. (2.7) and (2.8), the equations can be translated into

$$\dot{\mathbf{r}}(t_{k+1}) = \dot{\mathbf{r}}(t_k) + \frac{1}{2}\ddot{\mathbf{r}}(t_k)\delta t + \frac{1}{2}\ddot{\mathbf{r}}(t_{k+1})\delta t \tag{2.9}$$

$$\mathbf{r}(t_{k+1}) = \mathbf{r}(t_k) + \dot{\mathbf{r}}(t_k)\delta t + \frac{1}{3}\ddot{\mathbf{r}}(t_k)\delta t^2 + \frac{1}{6}\ddot{\mathbf{r}}(t_{k+1})\delta t^2 \tag{2.10}$$

According to Eq. (2.5), the acceleration term $\ddot{\mathbf{r}}(t_{k+1})$ at the (k+1)th time step can be expressed as below.

$$\ddot{\mathbf{r}}(t_{k+1}) = (\mathbf{M}+\mathbf{A})^{-1}(\mathbf{F}(t_{k+1}) - \mathbf{C}\mathbf{r}(t_{k+1})) \tag{2.11}$$

Inserting Eq. (2.11) into Eqs. (2.9) and (2.10), yields

$$\mathbf{r}(t_{k+1}) = (\frac{6}{\delta t^2}(\mathbf{M}+\mathbf{A}) + \mathbf{C})^{-1}(\mathbf{F}(t_{k+1}) + (\mathbf{M}+\mathbf{A})(\frac{6}{\delta t^2}\mathbf{r}(t_k) + \frac{6}{\delta t}\dot{\mathbf{r}}(t_k) + 2\ddot{\mathbf{r}}(t_k))) \tag{2.12}$$

In Eq. (2.12), the external forces $\mathbf{F}(t_{k+1})$ at the (k+1)th time step cannot be determined at the kth time step because of the interdependence between ship motions and external forces. Therefore, iterations are performed at each time step until the accuracy is acceptable. The convergence criterion is based on the increment of forces and moments from iteration step i to iteration step i+1.

$$\sqrt{\sum_{j=1,6}(F_j^{i+1} - F_j^i)^2} \Big/ \sqrt{\sum_{j=1,6}(F_j^i)^2} < \xi \tag{2.13}$$

where ξ is a small value, which is in the order of 10^{-3}.

By the Newmark's method and iterations, the motion and state variables can be updated and used as initial values for the next time step. Finally, the equations of motion can be solved step by step in time domain. The time interval δt needs to meet requirement to guarantee the stability of numerical integration, but this requirement is not significant because a much smaller time step is required for accurate representation of excitation and response.

2.2 Excitation forces

Ice forces and moments can be obtained from numerical models of ship–ice interaction, which are presented in detail in the following chapters. In this section, semi-empirical approaches are employed to determine the forces and moments caused by the propeller, rudder and ambient water. Euler forces are also derived.

2.2.1 Propeller and rudder forces

The evaluation of ship performance is usually quantified by determining the ship speed and energy consumed in transiting an ice-covered route. The basis for the calculation of ship speed for all route sections is the comparison of the net thrust available to the total ice resistance the ship encounters. In the navigation process, the net thrust available to overcome ice resistance can be estimated as [41]

$$T_{net} = T_B \left(1 - \frac{1}{3} \cdot \frac{u}{v_{ow}} - \frac{2}{3} \cdot \left(\frac{u}{v_{ow}} \right)^2 \right) \tag{2.14}$$

where T_B denote the bollard pull, u is the forward velocity component, v_{ow} stands for the open water speed.

The forces and moments induced by the propeller and rudder can be written as [41]

$$F_1^p(t) = T_{net} - \frac{1}{2} C_D \rho_w v_f^2 A_r \tag{2.15}$$

$$F_2^p(t) = \frac{1}{2} C_L \rho_w v_f^2 A_r \tag{2.16}$$

$$F_6^p(t) = \frac{1}{2} C_L \rho_w v_f^2 A_r \cdot x_r \tag{2.17}$$

Therein, C_L and C_D are the lift and drag coefficients of the rudder, ρ_w signifies the sea water density, v_f denotes the flow velocity, A_r represents rudder area, x_r is the location of the rudder.

C_L and C_D can be determined in wind tunnel tests or computations. For angles of attack α' smaller than stall angle α_{stall} (i.e. the angle of maximum C_L), the force coefficients may be approximated by the following formulas:

$$C_L = 2\pi \frac{\Lambda \cdot (\Lambda + 0.7)}{(\Lambda + 0.7)^2} \cdot \sin\alpha + C_Q \cdot \sin\alpha \cdot |\sin\alpha| \cdot \cos\alpha \tag{2.18}$$

$$C_D = \frac{C_L^2}{\pi \cdot \Lambda} + C_Q \cdot |\sin\alpha|^3 + C_{D0} \tag{2.19}$$

where Λ stands for the aspect ratio, C_Q denotes a resistance coefficient, $C_Q \approx 1$ may be used for rudders with a sharp upper and lower edge, C_{D0} approximates the surface friction, which can be given as

$$C_{D0} = 2.5 \cdot \frac{0.075}{(\log R_n - 2)^2} \tag{2.20}$$

In that equation, R_n represents the Reynolds number.

2.2.2 Hydrodynamic forces

The hydrodynamic forces because of ship motions relative to the ambient water are considered. According to Riska [5], since open water resistance is usually very small compared to ice resistance, the coupling between them can be neglected without causing significant error. Thus, the open water resistance and the pure ice resistance are separable. Moreover, the effect of ambient current is incorporated by using relative velocities, whereas the effect of waves is ignored because the ambient water is assumed to be totally covered by ice.

The hydrodynamic forces can be calculated by the cross-flow theory presented in Faltinsen [42]. The drag force F_1^c on the ship in the longitudinal direction is mainly induced by frictional forces, which can be approximated by the following formula.

$$F_1^c(t) = \frac{0.075}{\left(\log_{10} R_n - 2\right)^2} \cdot \frac{1}{2} \rho_w S_{wet} u |u| \tag{2.21}$$

where S_{wet} denotes the wetted surface of the ship.

The transverse viscous current force F_2^c and current yaw moment F_6^c can be evaluated using the cross-flow principle, which assumes that the flow separates due to cross-flow past the ship, that the longitudinal current component cannot influence the transverse forces on a cross-section, and that the transverse force on a cross-section is mainly due to separated flow effects on the pressure distribution around the ship. This means that the transverse current force and the yaw moment can be calculated as

$$F_2^c(t) = \frac{1}{2} \rho_w \int_{L_{WL}} C_D(x) D(x) v(x) |v(x)| dx \tag{2.22}$$

$$F_6^c(t) = \frac{1}{2} \rho_w \int_{L_{WL}} C_D(x) D(x) v(x) |v(x)| x dx \tag{2.23}$$

Therein, L_{WL} stands for the ship waterline length, $C_D(x)$ signifies the drag coefficient for cross-flow past an infinitely long cylinder with the cross-sectional area of the ship at the longitudinal coordinate x, $D(x)$ is the sectional draught, $v(x)$ represents the transverse velocity component.

2.2.3 Euler forces

Newton's second law can be expressed in terms of conservation of both linear momentum and angular momentum with respect to the inertial frame. For translational motions, the linear momentum conservation can be expressed as

$$\vec{f} = \frac{{}^n d}{dt}(m_g \vec{v}_{b/n}) = \frac{{}^b d}{dt}(m_g \vec{v}_{b/n}) + m_g \vec{\omega}_{b/n} \times \vec{v}_{b/n} \tag{2.24}$$

where $\vec{f}$ stands for the external force, excluding Euler force, m_g denotes the mass of ship, $\frac{{}^n d}{dt}$ and $\frac{{}^b d}{dt}$ represent time differentiation in the earth-fixed and body-fixed frame

respectively.

The vectors can be expressed in the body-fixed reference frame such that the translational motion becomes

$$m_g(\dot{\boldsymbol{v}}_{b/n}^b + \boldsymbol{\omega}_{b/n}^b \times \boldsymbol{v}_{b/n}^b) = \boldsymbol{f} \tag{2.25}$$

It can be seen from Eq. (2.25) that, the forces induced by a non-uniformly rotating frame can be obtained as $-m_g(\boldsymbol{\omega}_{b/n}^b \times \boldsymbol{v}_{b/n}^b)$.

Following a similar approach, for rotational motions, the angular momentum conservation can be expressed as

$$\vec{m} = \frac{{}^n d}{dt}(I\vec{\omega}_{b/n}) = \frac{{}^b d}{dt}(I\vec{\omega}_{b/n}) + \vec{\omega}_{b/n} \times (I\vec{\omega}_{b/n}) \tag{2.26}$$

In that equation, $\vec{m}$ denotes the external moment, I signifies the moment of inertia.

Eq. (2.26) can be written in the body-fixed reference frame as below.

$$\boldsymbol{I}\dot{\boldsymbol{\omega}}_{b/n}^b - (\boldsymbol{I}\boldsymbol{\omega}_{b/n}^b) \times \boldsymbol{\omega}_{b/n}^b = \boldsymbol{m} \tag{2.27}$$

From Eq. (2.27), we can observe that the moments caused by a non-uniformly rotating frame can be expressed as $(\boldsymbol{I}\boldsymbol{\omega}_{b/n}^b) \times \boldsymbol{\omega}_{b/n}^b$.

2.2.4 Ice forces

The ice forces and moments can be achieved from the numerical procedures in different ice types, whereas the ice forces induced by the displacing process, i.e. the turning, submerging and sliding process, can be calculated by the empirical formula proposed by Lindqvist [4]. The submergence resistance is caused by broken ice pieces passing beneath the ship, which is assumed to be distributed uniformly over the parallel midbody. The formulas are expressed as below.

$$F_1^{sbmg}(t) = R_s\left(1 + 9.4\frac{v_{b/n}^b}{\sqrt{gL_{WL}}}\right) \times \frac{u}{v_{b/n}^b} \tag{2.28}$$

$$F_2^{sbmg}(t) = R_s\left(1 + 9.4\frac{v_{b/n}^b}{\sqrt{gL_{WL}}}\right) \times \frac{v}{v_{b/n}^b} \tag{2.29}$$

where R_s is the submersion component of ice resistance, which is given by

$$\begin{aligned} R_s = {} & (\rho_w - \rho_{ice}) \cdot g \cdot h_i \cdot B\left(T\left(T+B\right)/\left(B+2T\right) + \right. \\ & \left. \mu_i\left(0.7L - T/\tan\eta - B/4\tan\beta + T\cos\eta\cos\gamma\sqrt{1/\sin\eta^2 + 1/\tan\beta^2}\right)\right) \end{aligned} \tag{2.30}$$

Therein, ρ_{ice} denotes the sea ice density, h_i stands for ice thickness, B and T are the breadth and draft of ship respectively, μ_i signifies the friction coefficient, η represent the stem angle, β is the waterline angle, γ can be obtained by

$$\gamma = \arctan(\frac{\tan\eta}{\sin\beta}) \tag{2.31}$$

Chapter 3

Numerical Model of Ship Operating in Level Ice fields

In ice infested waters, ship can navigate in various ice regions, among which level ice is the simplest type of ice field to consider, as it is undeformed, characterized only by one parameter of ice thickness. It is important to estimate both global and local ice loads on ship hulls. The global ice load governs the ship overall performance in ice, whereas the local ice loads are useful to evaluate structural safety in relation to a local part of ship hull. In this chapter, a semi-empirical numerical procedure is developed to model the continuous-mode icebreaking process in level ice in 6 DOFs. The numerical global and local ice loads are discussed through results of a case study conducted in a series of different ice conditions. Ship performance and statistics of ice-induced frame loads are analyzed. Comparisons are made of the simulated results against published results of numerical models and field measurements or empirical formula in level ice.

3.1 Ship–ice interaction mechanics in level ice fields

Many semi-empirical methods were proposed to estimate the resistance of a ship navigating in ice, as stated in Chapter 1. In this study, it is assumed that the repeating cycles of contact, crushing, and bending constitute a continuous breaking process of an intact level ice by an advancing ice-going ship. When a ship advances into level ice fields, contacts can occur between the instantaneous ship waterline and the ice cover edge. The vertical force component increases as the ship continues to penetrate into the ice plate. When it exceeds the bearing capacity of the ice edge, bending failure will occur and a circular ice floe will be broken from the ice plate. The advance of ship forces the ice floes to turn on edge until parallel with the ship hull. Subsequently, a new ice edge develops and the icebreaking process cycle repeats as the ship travels further. The overall process is shown in Fig. 3.1. The ice loads over the contact-crushing-bending period can be numerically computed, whereas the ice loads induced by the displacing process are calculated by the empirical formulas Eqs. (2.28) and (2.29). The global ice load is an integrated effect of local ice loads over the hull area. For a particular frame, the local line load [kN/m] is calculated by dividing the ice force on this frame by the frame spacing. The flow chart for the numerical implementation of the algorithm is illustrated in Fig. 3.2.

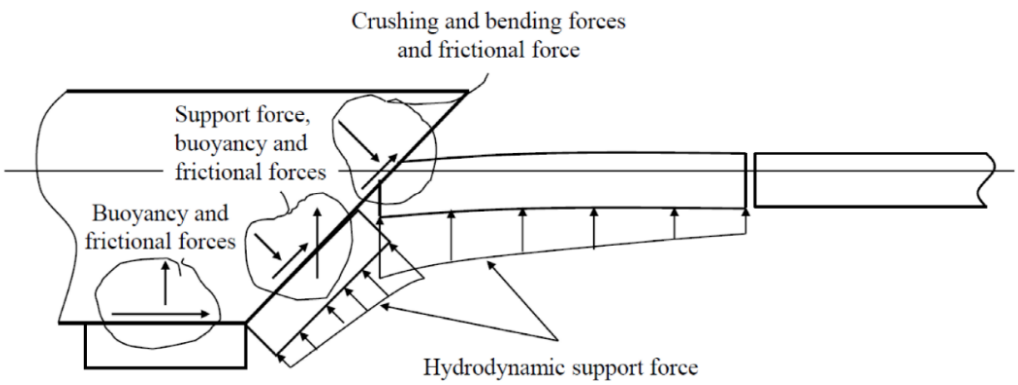

Fig. 3.1 The overall process of ship–ice interaction in level ice [43].

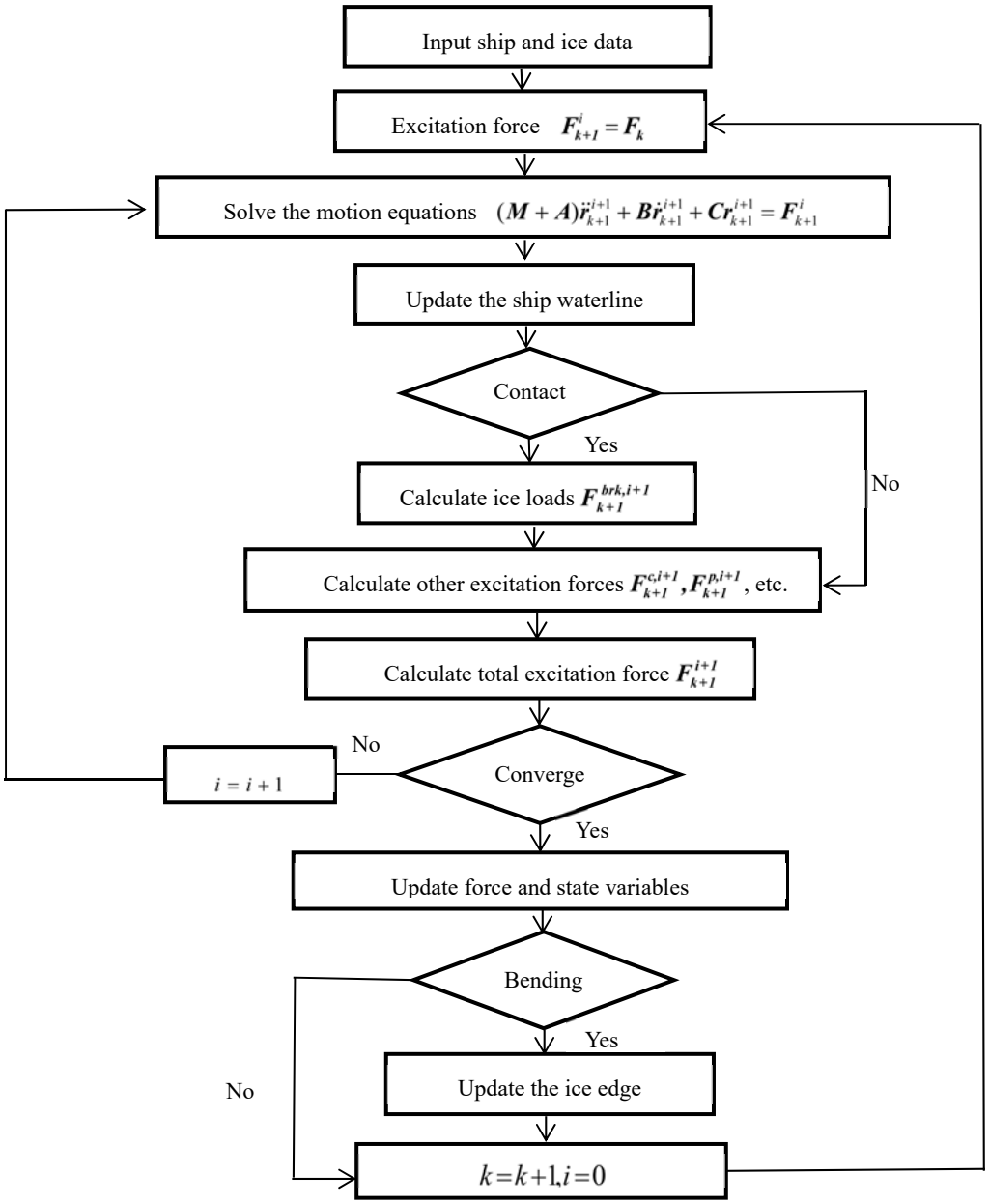

Fig. 3.2 Flow chart of numerical procedure.

3.1.1 Contact detection

In order to determine contact zones, first, the ship hull and ice edge are discretized into a number of nodes in the simulation program, where the ship waterline is discretized as a closed polygon, and ice edge is discretized as broken lines, as portrayed in Fig. 3.3. For ship motions in 6 DOFs, the instantaneous ship waterline need to be updated at each time step, by searching for the intersection between the ship hull and the water plane based on the ship current position and orientation.

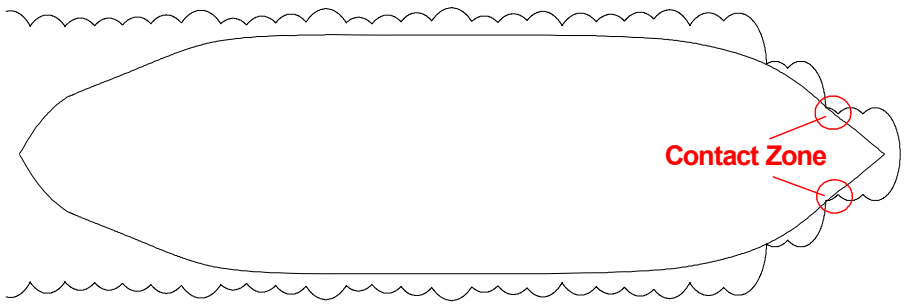

Fig. 3.3 Discretization of ice edge and ship waterline.

Contact is the first step in icebreaking process, and thus to identify the contact zones precisely is an important issue for determining the icebreaking force. In this study, a point-in-polygon computer geometric method [44] is adopted to check whether an ice edge node is inside the waterline polygon. The detailed algorithm is presented as below.

For a general polygon, the algorithm for determining if a point P is inside involves analyzing the intersections of the polygon and a ray whose origin is P and whose direction is (1,0). As a ray is traversed starting from P, each time an edge is transversely crossed, a switch is made from inside to outside or vice versa. An implementation keeps track of the parity of the crossings. Odd parity means P is inside, even parity means it is outside, which is illustrated in Fig. 3.4.

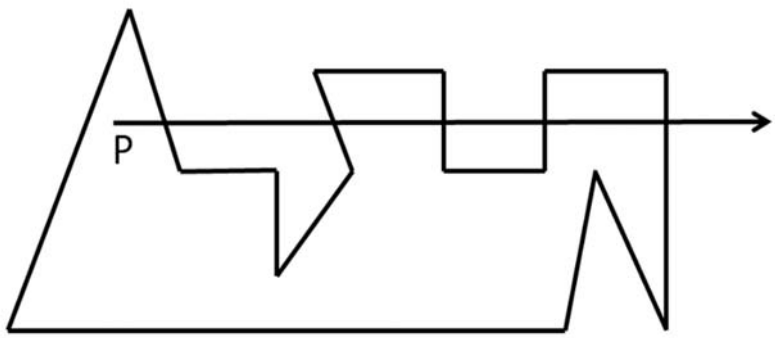

Fig. 3.4 Point-in-polygon test by counting intersections of ray with polygon.

Aside from the general case presented in Fig. 3.4, special cases that polygon edges are

coincident to the ray for P and that polygon vertices are on the ray can occur as well, as shown in Fig. 3.5.

The problem at the polygon vertex 1 is that the ray transversely intersects the polygon boundary at that vertex, so the intersection should count as only one crossing. However, the two edges sharing the vertex are processed separately, each edge indicating that the crossing at the vertex is transverse. The result is that the vertex is counted twice as a crossing, incorrectly reversing the current parity for the intersection count. Vertex 2 has a slightly different problem. The ray is inside the polygon slightly to the left of the vertex and is inside the polygon slightly to the right. The crossing at vertex 2 should be ignored since the ray does not transversely cross the polygon boundary. Processing the edges separately leads to the correct result because both edges report a transverse crossing by the ray at the common vertex 2.

The problem with the coincident polygon edge 〈5,6〉 is that it appears as if it is a single vertex, if vertex 5 were to be relocated at vertex 6, the inside/outside count would not change. Consider the coincident edge 〈3,4〉, if vertex 3 were to be relocated at vertex 4, the v-junction gets counted just like the one at vertex 2, so it is not a transverse crossing.

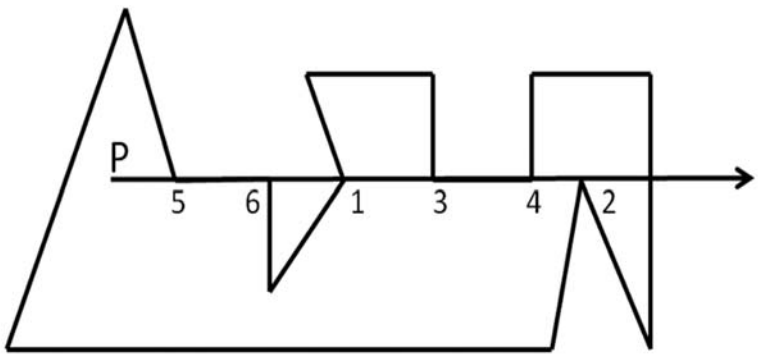

Fig. 3.5 Special cases for point-in-polygon test.

Preparata and Shamos [45] mention how to deal with these configurations. An edge is counted as a crossing of the ray with the polygon if one of the end points is strictly above the ray and the other end point is on or below the ray. Using this convention, coincident edges are not counted as crossing edges and can be ignored. Two edges above the ray that share a common vertex on the ray both count as crossings. If two edges below the ray share a common vertex on the ray, neither edge is counted. If one edge is above and one edge is below the ray, both sharing a vertex on the ray, the edge above is counted but the edge below is not.

In terms of mathematical expression of the above algorithm, set the coordinates of two vertexes on a polygon edge as (x_1, y_1) and (x_2, y_2), and the coordinate of P is (x_p, y_p). If this edge is transversely crossed by the ray, the coordinates must satisfy either of the following equations.

$$\begin{cases} y_1 > y_p \geq y_2 \\ x_p < x_1 + (y_p - y_1)(x_2 - x_1)/(y_2 - y_1) \end{cases} \tag{3.1}$$

or

$$\begin{cases} y_2 > y_p \geq y_1 \\ x_p < x_1 + (y_p - y_1)(x_2 - x_1)/(y_2 - y_1) \end{cases} \tag{3.2}$$

As the point-in-polygon method discussed previously, ice edge nodes inside the instantaneous ship waterline can be checked on the basis of the parity for the intersection count.

3.1.2 Crushing force

As the hull contacts with ice edge in level ice sheet, local crushing occurs at the contact zones. In each contact zone, a crushing force F_{cr} acts on the ship hull, which is normal to the contact surface. In addition, F_{cr} can be determined as the product of average crushing pressure p_{av} and contact area A_{cr}.

$$F_{cr} = p_{av} A_{cr} \tag{3.3}$$

3.1.2.1 Contact area

In order to calculate the crushing force, the contact area needs to be obtained. According to the previous sub-section, the contact zones between ship hull and ice edge on the water plane can be ascertained, based on which the contact area can be determined. After a contact zone is found, interpolations are applied to identify the intersections of ship waterline and ice edge. The edge of a contact zone can be regarded as a closed polygon, which is comprised of ice nodes that enter ship waterline, hull nodes that enter ice plate and intersections, as shown in Fig. 3.6. The polygon area, i.e. the projection of contact area on the water plane can be calculated as [44]

$$A = \frac{1}{2} \sum_{i=0}^{n-1} (x_i y_{i+1} - x_{i+1} y_i) \tag{3.4}$$

where n denotes the total number of vertexes, (x_i, y_i) represents the coordinate of an arbitrary vertex of the closed polygon.

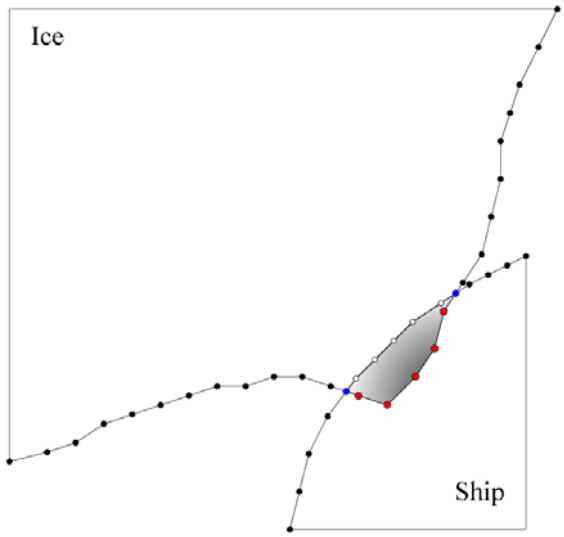

Fig. 3.6 A typical contact zone.

Contact surface is assumed to remain flat during crushing, in order to calculate every contact area. As the ship advances against the ice sheet after initial contact, the contact surface is regarded as a triangle plane. When the minimum bending force required to create the bending failure has not been reached before the crushing height becomes equal to the ice thickness, the contact geometry changes from a triangle to a trapezium. We first calculate the projection of contact area on the water plane A_c, when the crushing height is as high as the ice thickness. The contact geometry can be then identified by comparing A_c against the area A given in Eq. (3.4).

In this critical case, the crushing depth L_c and crushing width L_h are obtainable as

$$L_c = \frac{h_i}{\tan\alpha} \tag{3.5}$$

$$L_h = 2L_c \tan(\frac{\phi}{2}) \tag{3.6}$$

Therein, α denotes the normal frame angle of the ship hull, ϕ simplifies the opening angle of ice wedge.

Then the contact area is calculatable as below.

$$A_c = \frac{1}{2} L_c L_h = (\frac{h_i}{\tan\alpha})^2 \tan(\frac{\phi}{2}) \tag{3.7}$$

Case 1: A_c is greater than A, which means the contact geometry is a triangle, and thus the contact area can be achieved based on the projection on the water plane.

$$A_{cr} = \frac{A}{\cos\alpha} \tag{3.8}$$

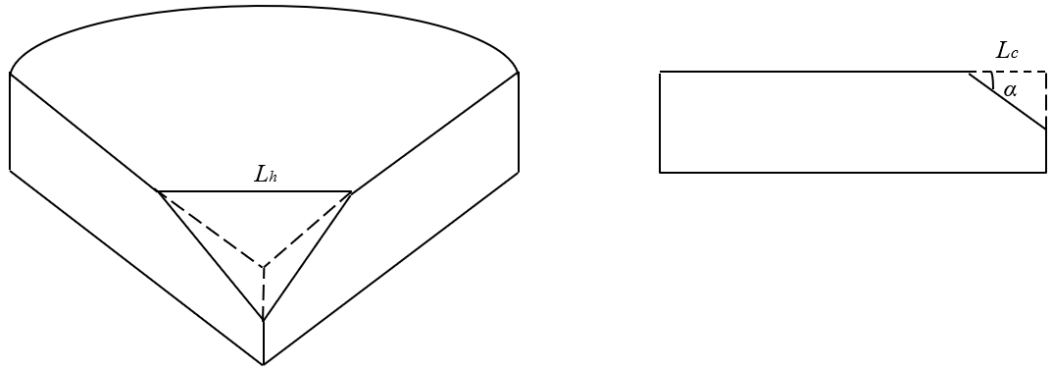

Fig. 3.7 Case1: contact surface.

Case 2: A_c is smaller than A, when further crushing happens after the crushing height has reached the ice thickness. The contact surface changes to a trapezium plane. The altitude of trapezium h_t can be obtained by

$$h_t = \frac{h_i}{\sin\alpha} \tag{3.9}$$

The crushing depth L_c now is

$$L_c = \sqrt{\frac{A}{\tan(\frac{\phi}{2})}} \tag{3.10}$$

The lengths of each base of the trapezium L_h and L_H can be calculated as

$$L_h = 2\sqrt{A\tan(\frac{\phi}{2})} \tag{3.11}$$

$$L_H = 2(L_c - \frac{h_i}{\tan\alpha})\tan(\frac{\phi}{2}) \tag{3.12}$$

Consequently, the contact area can be expressed as

$$A_{cr} = \frac{1}{2}(L_h + L_H)h_t = (2\sqrt{A\tan(\frac{\phi}{2})} - \frac{h_i}{\tan\alpha}\tan(\frac{\phi}{2}))\frac{h_i}{\sin\alpha} \tag{3.13}$$

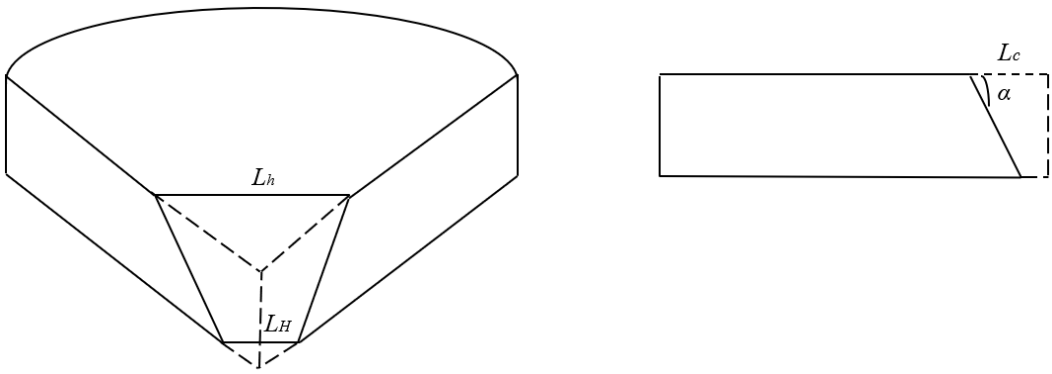

Fig. 3.8 Case2: contact surface.

Case 3: since the slope angle of the parallel mid-body tends to be vertical, when the numerical model is conducted in 6DOFs, the mid-ship hull may contact the bottom surface of the ice sheet first due to roll motions. If the contact geometry is a trapezium, then the contact area is calculatable based on the projection area on the water plane, which is similar to the calculation process of case 2.

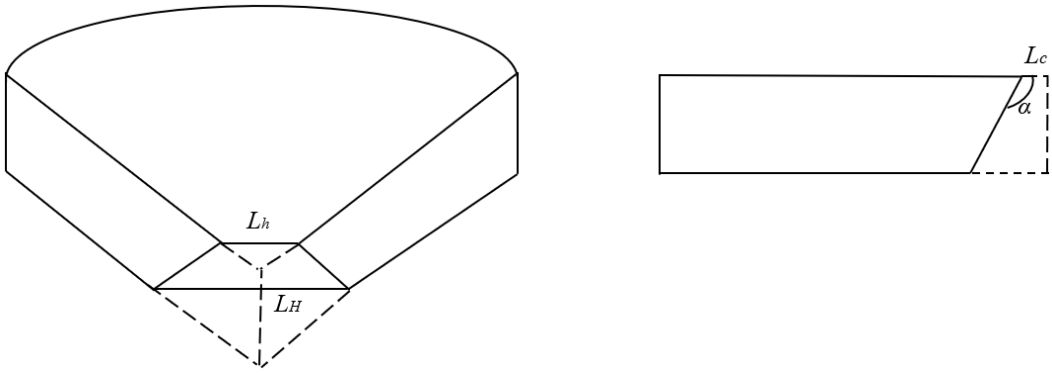

Fig. 3.9 Case 3: contact surface.

Case 4: if the mid-ship hull contacts the bottom surface first and the contact geometry is a triangle, then the contact zone cannot be found on the water plane, and the contact detection needs to be performed in 3 dimensions (3D), which is extremely complicated. In the present study, this case has not been considered in the simulation procedure.

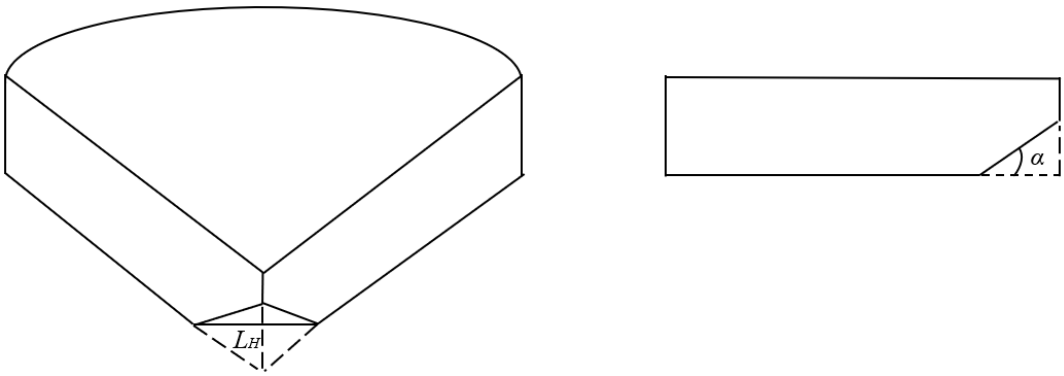

Fig. 3.10 Case 4: Contact surface.

3.1.2.2 Pressure–area relation

To calculate the crushing force in Eq. (3.3), for simplicity, it is typically assumed that p_{av} can be represented by the crushing strength σ_{cr} of sea ice. Nevertheless, the pressure during crushing may not be a constant due to the mechanical properties of ice. A large amount of in-service data demonstrates a decrease of average pressure with increasing contact area [46] [47]. A relationship between the pressure and the area has been determined as the following form.

$$p_{av} = C_p A_{cr}^{D_p} \tag{3.14}$$

In that equation, C_p and D_p are empirical parameters, C_p is positive, D_p is negative.

Palmer [48] proposed a simple mathematical model which quantified the *p–a* relation based on combination of fracture mechanics model of fragment breaking and fractal hierarchical distribution of fragment size. Palmer's model took the values of C_p and D_p as 1.7 and -0.25 respectively, Eq. (3.14) can be then written as

$$p_{av} = 1.7 A_{cr}^{-0.25} \tag{3.15}$$

Consequently, the crushing force is given by the pressure multiplied by the area,

$$F_{cr} = p_{av} A_{cr} = 1.7 A_{cr}^{0.75} \tag{3.16}$$

3.1.3 Bending failure

3.1.3.1 Contact force analysis

Aside from the local crushing force normal to the contact surface, the ship hull is also subjected to vertical and horizon tal frictional forces caused by the tangential relative motions. A local coordinate system, denoted as τnz, is introduced to transform the rigid body velocities to the hull nodal velocities, as shown in Fig. 3.11(a). Presumably, no vertical (bending) displacement of the ice wedge exists during crushing. Therefore, frictional forces f_1 and F_τ are proportional to the relative velocity components, which can be calculated as

$$f_1 = \mu_i F_{cr} \frac{v_1}{\sqrt{v_1^2 + v_\tau^2}} \tag{3.17}$$

$$F_\tau = \mu_i F_{cr} \frac{v_\tau}{\sqrt{v_1^2 + v_\tau^2}} \tag{3.18}$$

where v_1 and v_τ are the relative velocity components on the contact surface, as illustrated in Fig. 3.11(c).

On the A–A plane as shown in Fig. 3.11(b), v_1 is obtainable as

$$v_1 = v_{n,1} + v_{z,1} = v_n \cos\alpha + v_z \sin\alpha \tag{3.19}$$

where v_z is the velocity component on the z_0 axis of the earth-fixed frame.

The normal velocity component v_n and tangential velocity component v_τ can be calculated as below.

$$v_n = v_x \cos\beta + v_y \sin\beta \tag{3.20}$$

$$v_\tau = v_x \sin\beta - v_y \cos\beta \tag{3.21}$$

Therein, v_x and v_y are the velocity components on the x_0 axis and y_0 axis of the earth-fixed frame, β represents the waterline angle at the current node.

Based on the force analysis as presented in Fig. 3.11, the following components can be derived.

$$F_n = F_{cr} \sin\alpha + f_1 \cos\alpha \tag{3.22}$$

$$F_z = F_{cr} \cos\alpha - f_1 \sin\alpha \tag{3.23}$$

$$F_x = -F_n \cos\beta - F_\tau \sin\beta \tag{3.24}$$

$$F_y = F_n \sin\beta - F_\tau \cos\beta \tag{3.25}$$

where F_x, F_y and F_z are the icebreaking force components expressed in the earth-fixed frame. Nevertheless, the motion equations are solved in the body-fixed frame, and therefore these force components need to be transformed from the earth-fixed frame to the body-fixed frame by using the inverse of rotational matrix.

$$\mathbf{F}^{\mathrm{brk}} = \boldsymbol{R}_b^n(\boldsymbol{\Theta}_{nb})^{-1}\mathbf{F} \tag{3.26}$$

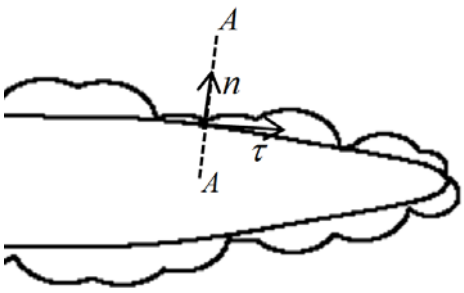

(a) Local coordinate system *τnz*

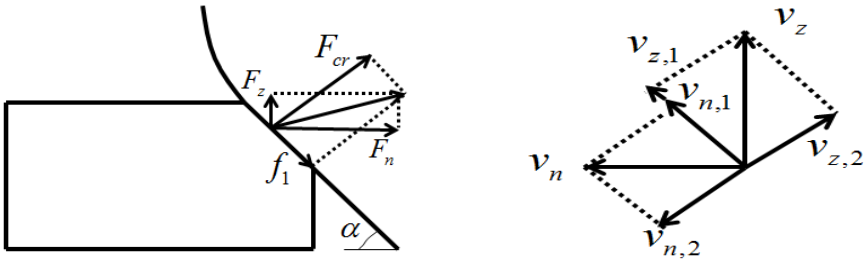

(b) Local contact force on A–A plane

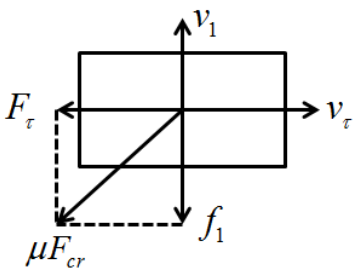

(c) Local contact force on the contact surface

Fig. 3.11 Contact force.

3.1.3.2 Bending failure criterion

Kashtelian [49] (see Kerr [50]) predicted the breaking load of edge-loaded sea ice plate with ship weight as the vertical load, based on the observation of the carrying capacity when the ice wedges initially break off, as presented in Fig. 3.12. The bearing capacity for an ideal wedge with an opening angle ϕ is calculable as below.

$$P_f = C_f \left(\frac{\phi}{\pi}\right)^2 \sigma_f h_i^2 \tag{3.27}$$

In that equation, σ_f is the flexural strength of ice plate, C_f is an empirical coefficient, which is obtainable from some measurements. Kashtelian proposed that the constant C_f equals a small value, which is close to 1, whereas a value of 4.5 was used and validated by the empirical ice resistance formula in Nguyen [8]. Su [11] chose the value of 3.1 for C_f, which is adopted in the present study.

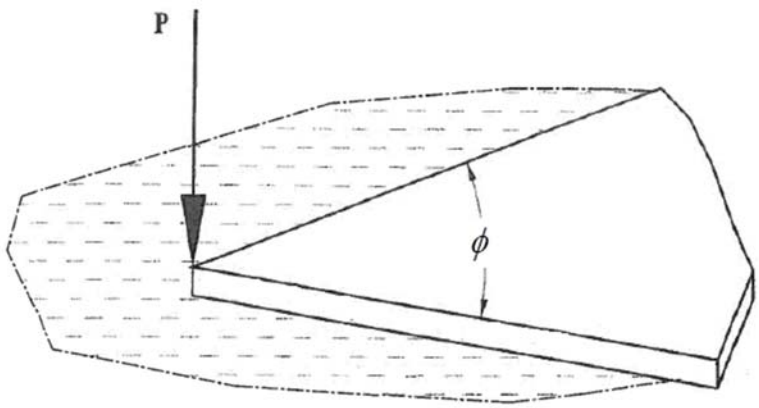

Fig. 3.12. An ice wedge subjected to a load P at its apex. [50].

Observation in the field indicate that, for an ice wedge with a large opening angle, several radial cracks form and propagate before the formation of a circumferential crack that causes final failure, as portrayed in Fig. 3.13.

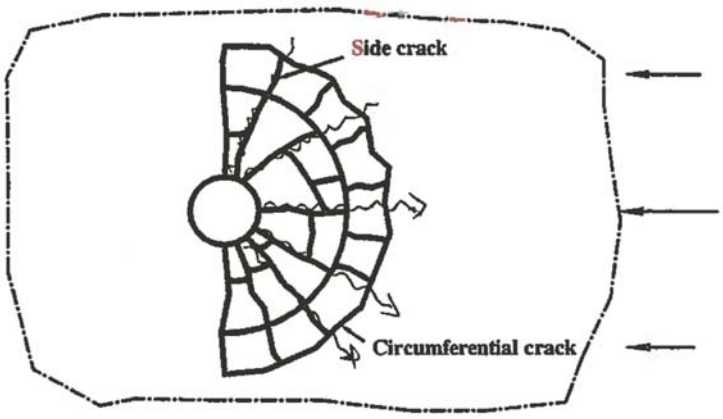

Fig. 3.13 Cracks for ice wedge with a large opening angle [7].

It is assumed that n is the number of radial cracks and that the n formed wedges are all of equal opening angle ϕ_n, i.e. $\phi_n = \phi/n$, and thus the failure load can be obtained as a summation of that for the n small wedges, which can be expressed as

$$P_f = nC_f(\frac{\phi}{n\pi})^2\sigma_f h_i^2 = \frac{1}{n}C_f(\frac{\phi}{\pi})^2\sigma_f h_i^2 \tag{3.28}$$

Form this equation, it can be seen that the bearing capacity P_f is inversely proportional to the number of radial cracks n, which means that more small ice wedges are assumed, then the failure load could become lower. From the perspective of structural safety, in this study, $n = 2$ is used when the opening angle is larger than 120°, in order to achieve a relatively conservative value of failure load, which can be calculated as

$$P_f = \frac{1}{2}C_f(\frac{\phi}{\pi})^2\sigma_f h_i^2 \tag{3.29}$$

If the vertical component of the contact force between ice and hull F_z, given in Eq. (3.23) exceeds the bending failure load of ice cover P_f, the ice wedge would be broken

from the ice edge. Otherwise, only local crushing occurs on the contact surface.

3.1.3.3 Geometry of ice wedge idealization

The ice wedges formed in the icebreaking process are determined by bending cracks, which are idealized and described by a single parameter, namely the icebreaking radius. The geometrical idealization of the ice wedge in contact with the ship hull is illustrated in Fig. 3.14, where the bending crack is determined by the interpolation of the icebreaking radius at the first and last contact node (i.e. R_f and R_l). The icebreaking radius R_I is derived from the expression given in Wang [7], on the basis of information from Enkvist [2] and Varsta [51].

$$R_I = C_l l(1.0 + C_v v_n^{rel}) \tag{3.30}$$

where v_n^{rel} is the relative normal velocity between the ice and the hull node, C_l and C_v are two empirical parameters obtained from field measurements, C_l having a positive value 0.32 and C_v is a negative value -0.25 referring to Enkvist [2], l is the characteristic length of the ice, i.e. the distance between the point of load to the location where the crack deformation occurs at the ice plate, which can be formulated according to the thin plate theory as follows,

$$l = \left(\frac{E h_i^3}{12(1-\upsilon^2)\rho_i g} \right)^{\frac{1}{4}} \tag{3.31}$$

Therein, E represents the Young's modulus of ice, υ stands for Poisson's ratio.

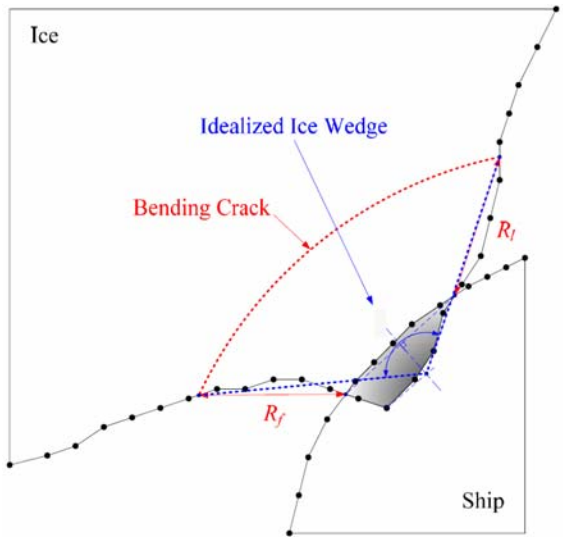

Fig. 3.14 Geometrical idealization of the ice wedge.

The radius obtained from the formula mentioned above is a deterministic crack size, however, cracks of various sizes are observed in an icebreaking run, as introduced in Su et al. [11]. Consequently, in this study, the crack size is defined by a random crack radius. In a numerical simulation of ice–cone interaction, Izumiyama et al. [6] assumed that the crack size followed a normal distribution. The size of the crack is defined by

the radius R_I of the approximated circular arc and the ratio Z' of the crack radius to the length l_{br}, given by:

$$l_{br} = (\sigma_U h_i / \gamma_w)^{0.5} \tag{3.32}$$

where σ_U is the flexural strength of ice in upward bending, γ_w is the specific weight of water. The distribution has a mean z'_m of 0.94 and a standard deviation z'_{sd} of 0.27, which were determined based on the observed crack pattern in the model test.

There has been no reliable theory on the crack size distribution until now, whereas Izumiyama' method seems a reasonable estimate based on the experimental data. Therefore, a normal distribution is used and the ratio between the standard deviation R_{Isd} and the mean crack radius R_{Im} is assumed to be the same as the value of z'_{sd}/z'_m mentioned above. Herein, the mean crack radius is calculated by the deterministic method Eq (3.30). A random crack radius can then be generated by using:

$$\begin{aligned} &F(R_I) = \frac{1}{\sqrt{2\pi}\sigma}\int_0^{R_I} \exp\left(\frac{-(s-R_{Im})^2}{2R_{Isd}^2}\right)ds \\ &U \sim U(0,1) \\ &R_I = F^{-1}(U) \end{aligned} \tag{3.33}$$

where $F(R)$ is the cumulative distribution function (CDF) of the crack radius, $F^{-1}(U)$ is the inverse CDF, and U is a uniformly distributed random number between 0 and 1.

3.2 Numerical results of ice loads in level ice fields

3.2.1 Global ice loads and ship performance

The numerical method introduced above is implemented to model a full-scale ship navigating in level ice. The continuous ice loading processes in transiting operation in a uniform level ice of different thickness are reproduced by the simulation program. The principal dimensions of the ship and the ice properties are listed in Tables 3.1 and 3.2 respectively.

Table 3.1 Ship characteristics

Length between perpendiculars	149.26 m
Breadth	22.36 m
Draught	8 m
Displacement	21000 t
Moment of inertia I_{xx}	1.39×10^8 kg m^2
Moment of inertia I_{yy}	2.44×10^9 kg m^2
Moment of inertia I_{zz}	2.57×10^9 kg m^2
Waterline angle β	23.6°
Stem angle η	21.8°

Table 3.2 Ice properties

Young's modulus E	3500 MPa
Poisson ratio υ	0.3
Flexural strength σ_f	0.55 MPa
Frictional coefficient μ_i	0.15
Density of sea water ρ_w	1025 kg/m^3
Density of sea ice ρ_i	900 kg/m^3

Fig. 3.15 and Fig.3.16 give the simulated time histories of global icebreaking loads which excludes ice submersion force, driven by constant thrust in level ice thicknesses of 0.2 m and 1.0 m respectively. The calculated ice loading process consists of numerous spike-like peaks. The magnitude of ice loads in 1.0 m thick ice is much higher than that in the ice of 0.2 m thickness. Moreover, from these two figures, it can be observed that in the case of 0.2 m ice thickness, the loading series shows relative regularity, whereas in the case of 1.0 m thick ice, the process seems more dynamic. It can be for the reason that the breaking force is considerably small compared to the propulsion power in thin ice, however, the ice loads are comparable to and sometimes even higher than the thrust in thick ice. Consequently, the ice loading history in 1.0 m thick ice is apparently irregular.

The mean values in 0.2 m and 1.0 m ice thickness are 8.6465 KN and 477.28 KN respectively. Nevertheless, the peak value in 0.2 m thick ice can reach more than 200 KN, and the load amplitude in 1.0 m thick ice is up to nearly 6000 KN, compared to which, the mean values are significantly small. It can be explained that in an icebreaking cycle, after the bending failure is initiated, ice wedges drop from the ice plate and a channel forms for the ship to transit. No contact occurs between ship and ice in the channel, and therefore the breaking force would decline to zero until subsequent contact, which causes low mean value.

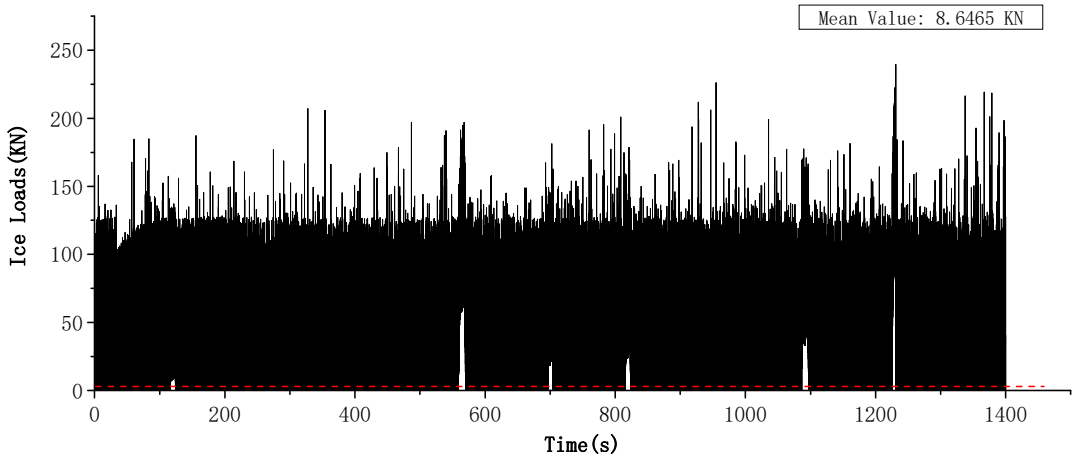

Fig. 3.15 Simulated time histories of global icebreaking loads in 0.2 m thick ice.

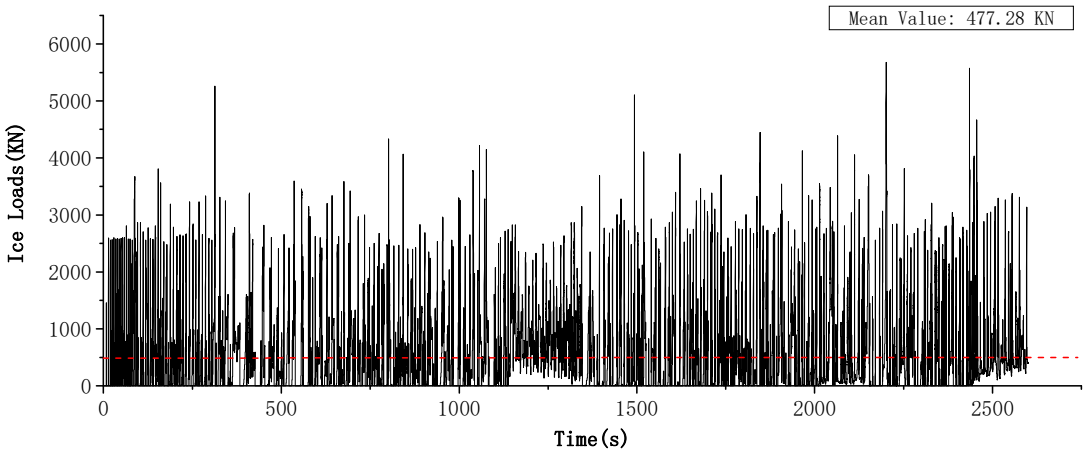

Fig. 3.16 Simulated time histories of global icebreaking loads in 1.0 m thick ice.

In order to validate the present numerical codes, the simulated results are compared to the ship performance data from numerical procedure in Su et al. [11]. Su carried out a numerical analysis of icebreaker AHTS/IB Tor Viking II, and verified the computed results by comparison with the ice trials. The peak value of ice loads in 0.5 m thick ice is close to 1400 KN with a constant ship speed of 5 m/s in Su's model, and the mean value is 356 KN. By contrast, with the same ice thickness and ship speed, the peak loads by the present model can reach as high as 4000 KN, and the mean value is 1257 KN, which is much higher than those results of Su. It can be attributed to the different dimensions of ship models used in the two programs. The length of icebreaker AHTS/IB Tor Viking II is 75.2 m, whereas that of the present model is 149.26 m. Considering the larger scale of ship used in this study, the numerical result seems reasonable.

The simulated speed time series in 0.2 m thick ice and 1.0 m thick ice are presented in Fig. 3.17 and Fig. 3.18 respectively.

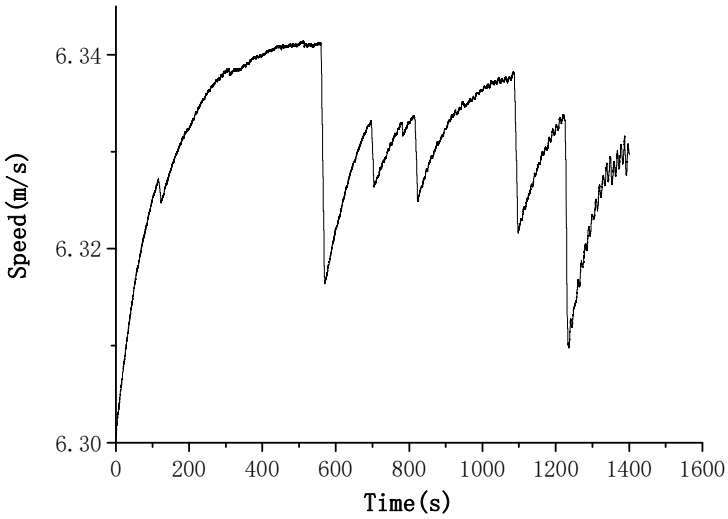

Fig. 3.17 Simulated speed time series in 0.2 m thick ice.

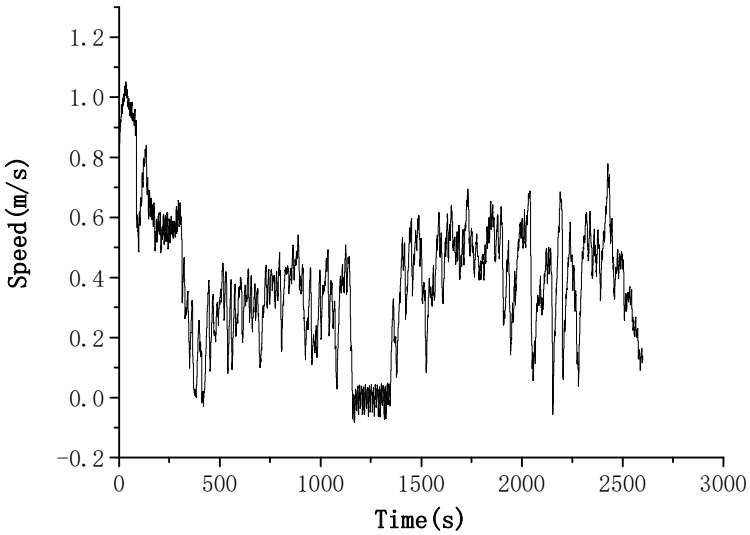

Fig. 3.18 Simulated speed time series in 1.0 m thick ice.

It can be seen that the speed achieved in 0.2 m thick ice is quite stable, varying in a small range from 6.30 m/s to 6.34 m/s, which corresponds to the regular loading process presented in Fig. 3.15. The speed in the case of 1.0 m ice thickness varies relatively obviously. During the period between 1100s and 1300s, the speed decreases and starts to oscillate around zero value, due to the high loads of this duration. We can see from Fig. 3.16 that the ship experiences continuous contact with the ice sheet in this period, which cause that the breaking force increase again before drop to zero.

Ice resistance is defined as the time average of all longitudinal forces due to ice acting on the ship. Estimation of ice resistance is a significant issue because it is closely related to propulsion and determines the engine power of the ship. An empirical formula proposed by Lindqvist [4] based on the full scale tests in the Bay of Bothnia is a simple way to estimate the ice resistance, which consists of three resistance terms: crushing of ice at the bow, bending of ice at the bow, and submergence resistance along the parallel midbody. Each of these terms is multiplied by a speed dependent term to form the total

level ice resistance as below.

$$R_{\text{level}} = (R_{\text{C}} + R_{\text{B}})(1 + 1.4\frac{v_{b/n}^{b}}{\sqrt{gL_{WL}}}) + R_s\left(1 + 9.4\frac{v_{b/n}^{b}}{\sqrt{gL_{WL}}}\right) \tag{3.34}$$

Therein, R_s signifies the submergence resistance as stated in Chapter 2, R_C denotes the resistance due to crushing at the bow, R_B is the resistance induced by bending and breaking of ice at the bow. R_C and R_B are given as

$$R_{\text{C}} = 0.5\sigma_b h_i^2(\tan\eta + \mu_i\cos\eta/\cos\gamma)(1 - \mu_i\sin\eta/\cos\gamma) \tag{3.35}$$

$$R_{\text{B}} = 0.003\sigma_b B h_i^{1.5}(\tan\gamma + \mu_i\cos\eta/\sin\beta\cos\gamma)(1 + 1/\cos\gamma) \tag{3.36}$$

where σ_b represents the bending strength of the ice.

Verification of the simulation routine and Lindqvist ice resistance formulation with a constant ship speed of 5 m/s is presented in Fig. 3.19. In the cases of 0.2 m, 0.3 m, 0.4 m and 0.8 m thick ice, the numerical results are quite consistent to Lindqvist resistance. In the cases of 0.5 m, 0.6 m and 0.7 m ice thickness, the numerical values are higher than Lindqvist results, whereas in 0.9 m and 1.0 m thick ice, the simulated resistance are lower. However, the fitted exponential curve of numerical results by the present model shows good agreement with that computed by the empirical formula.

Furthermore, it can be observed that the ice resistance calculated by Lindqvist formula increases with ice thickness, but some deviations occur in the simulation results. It can be attributed to the different icebreaking pattern. Take the cases of 0.7 m and 0.8 m thickness as an example, the resistance value in 0.8 m thick ice is smaller, even if the ice plate is thicker. Fig. 3.20 and Fig. 3.21 show the breaking patterns in 0.7 m and 0.8 m thick ice respectively. Compared with the case of 0.8 m thickness, some contact zones occur at the parallel midbody in 0.7 m thick ice, where the frame angle is nearly vertical, as portrayed in the boxes of Fig. 3.20, and consequently, the vertical component of contact force is not sufficient to induce a bending failure. The crushing area could progressively increase, which leads to severe icebreaking force.

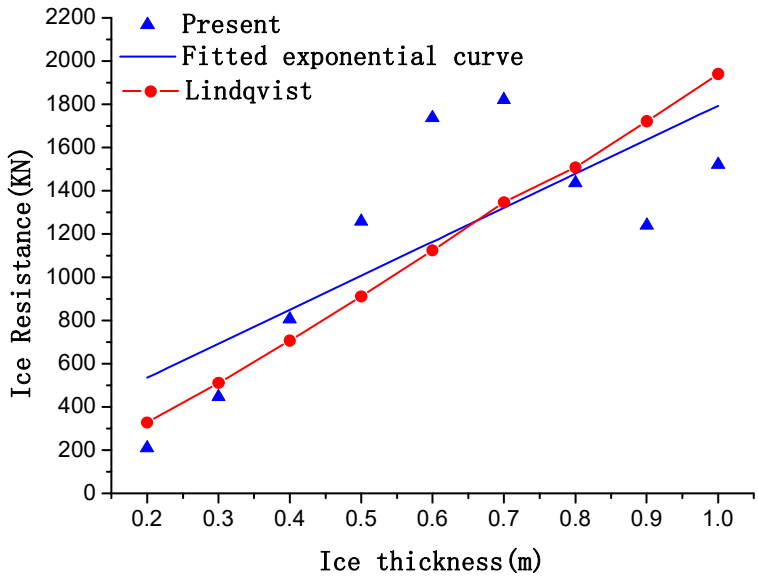

Fig. 3.19 Simulated ice resistance in level ice and the Lindqvist's ice resistance.

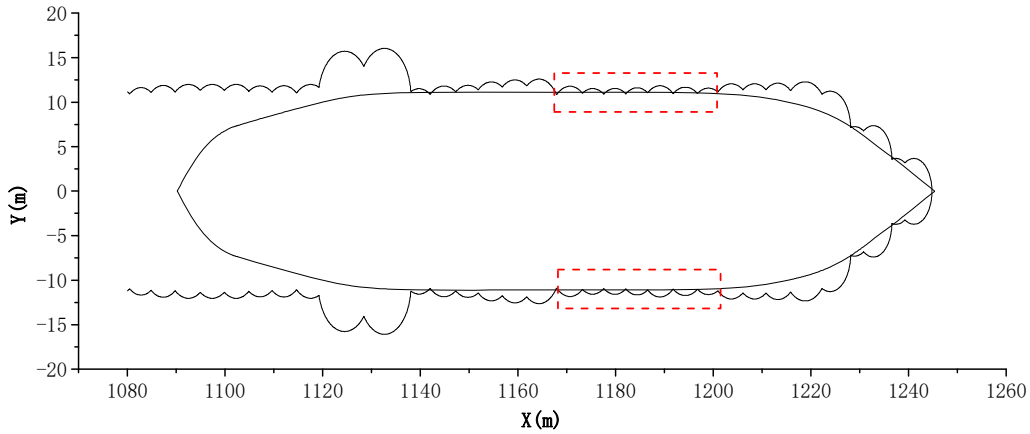

Fig. 3.20 Icebreaking pattern in 0.7 thick ice.

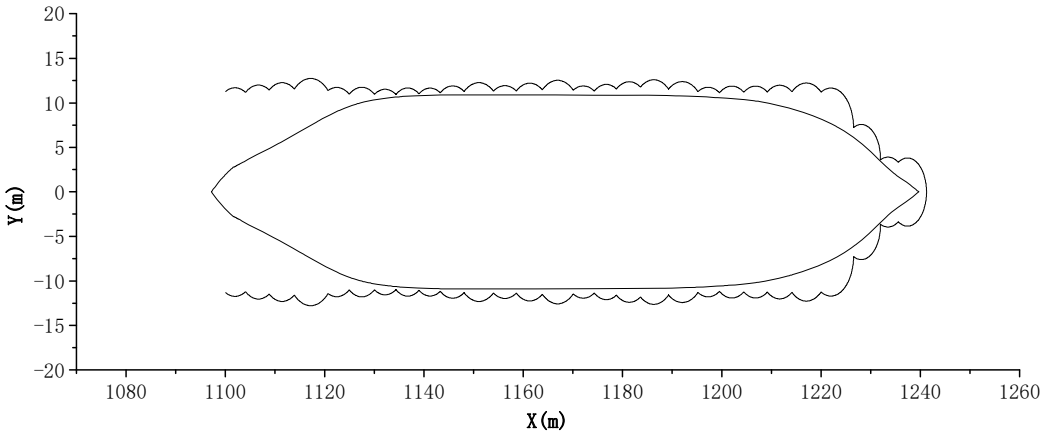

Fig. 3.21 Icebreaking pattern in 0.8 thick ice.

Ship performance is usually described by a plot of ice thickness versus the forward speed that can be attained at full propulsion power, i.e. the *h*–*v* curve. Fig. 3.22

illustrates the curves obtained in the present simulation and Su's numerical program [11]. We can see that the attainable speeds of the present ship model are lower than those of Su's model, due to the higher loads level caused by a larger scale. Nevertheless, the downward trend with ice thickness and the drop rate are quite consistent between the two models.

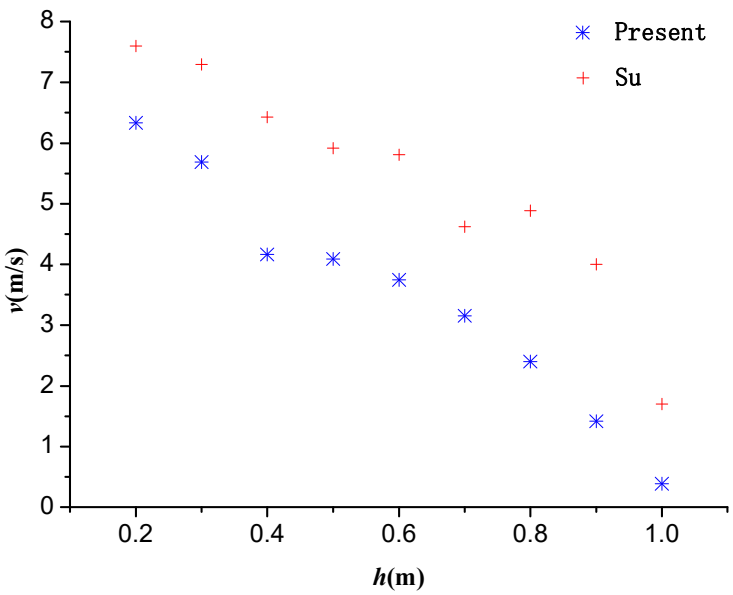

Fig. 3.22 The *h*–*v* curve.

3.2.2 Local ice-induced loads and statistical analysis

3.2.2.1 Local ice-induced loads

Aside from global ice loads, the line load on a specified frame can be obtained from the numerical simulation. Because the ice sheet is crushed continuously by bow shoulders, the icebreaking forces become more severe at these areas. Therefore, a frame on the bow shoulder area is selected for this study. Its location is marked as presented in Fig. 3.23.

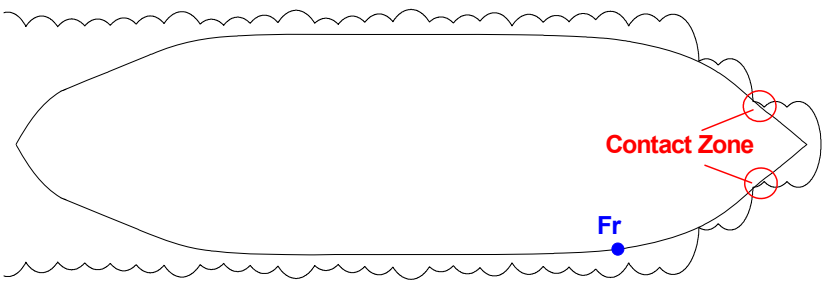

Fig 3.23 The location of calculated frame at bow shoulder area.

The local ice-induced loads with different ice thickness and initial ship speed are discussed in this study. Fig. 3.24 shows the frame loads in various thickness. It can be observed that the local loads level increase with the increasing thickness generally, and

the load values are sensitive to ice thickness, because the icebreaking pattern is heavily dependent on the factor of ice thickness.

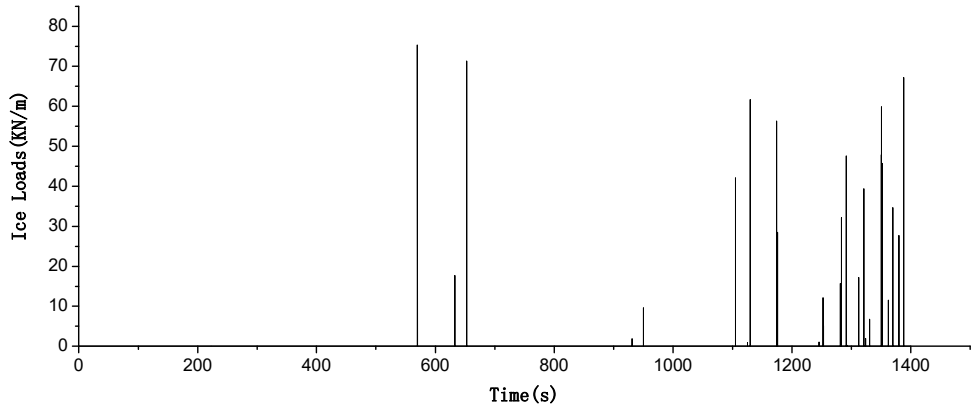

(a) ice thickness = 0.2 m

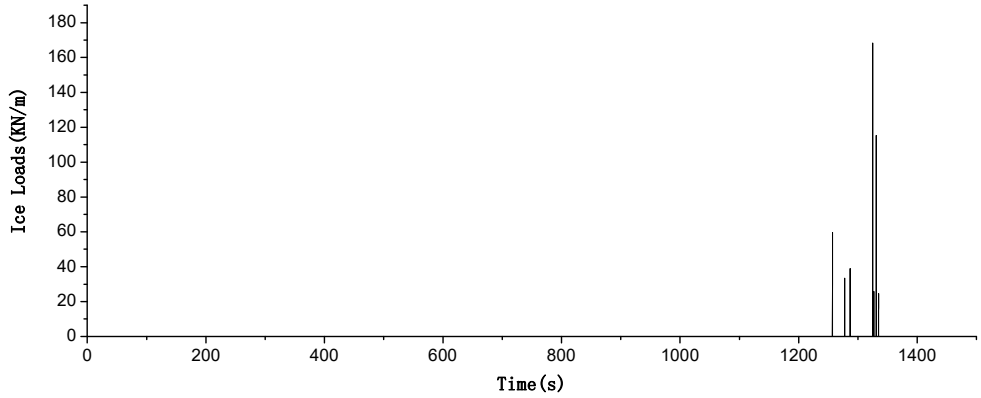

(b) ice thickness = 0.3 m

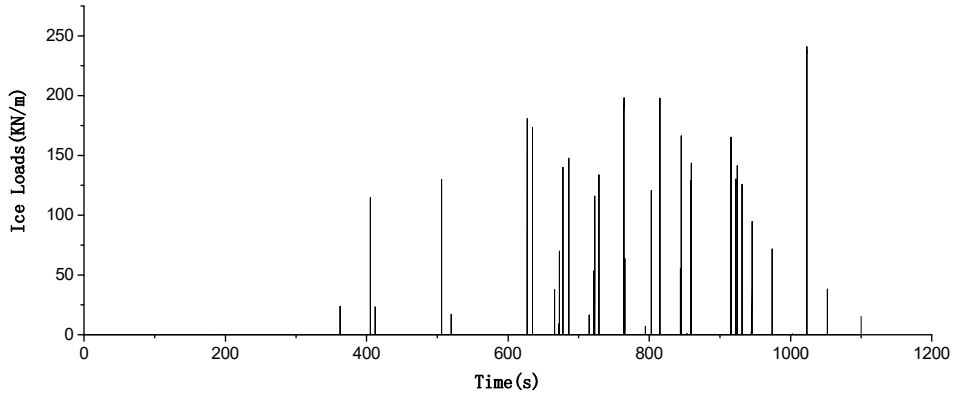

(c) ice thickness = 0.4 m

Fig. 3.24 The calculated frame loads with different ice thickness.

The frame loads in 0.2 m thick ice with various initial ship speeds are presented in Fig. 3.25. The initial speeds are set around the attainable one at full propulsion power, and close to each other, as 6.29 m/s, 6.30 m/s and 6.31 m/s respectively. Although the global ice loads tend to be regular and stable, the simulated frame loads are sensitive to the

initial speed. Both the magnitude and frequency of local loads show some discrepancy among these cases.

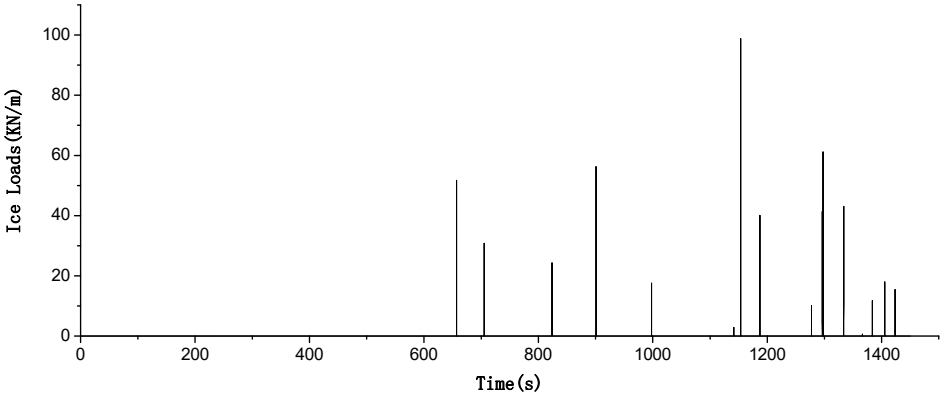

(a) initial speed = 6.29 m/s

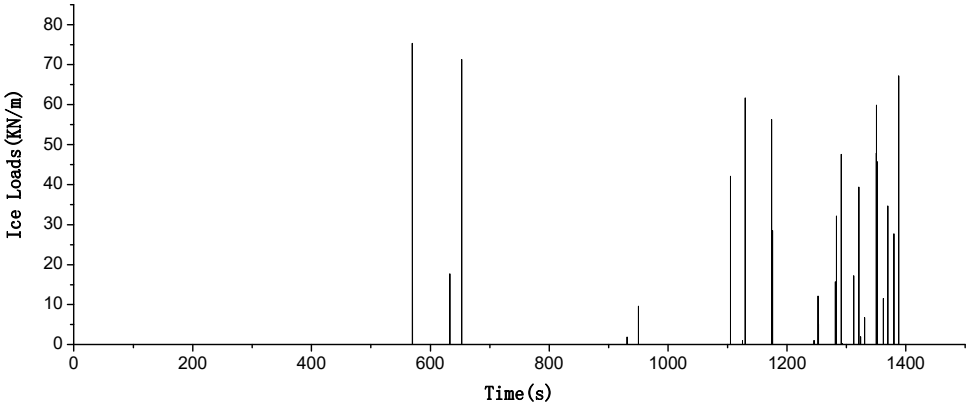

(b) initial speed = 6.30 m/s

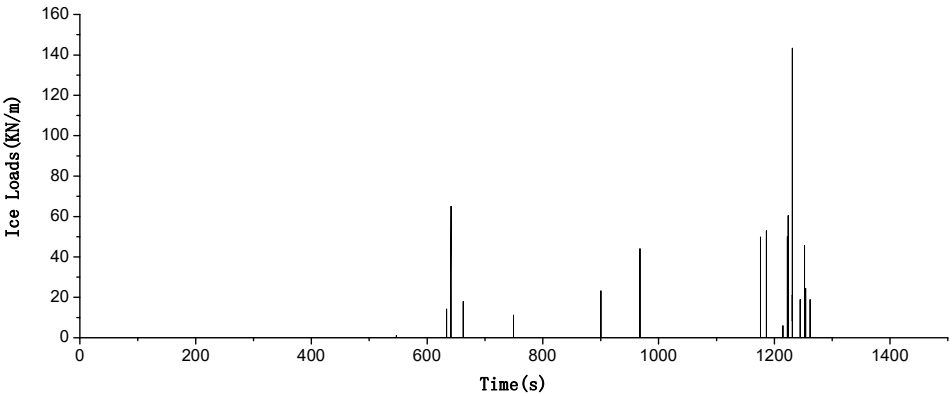

(c) initial speed = 6.31 m/s

Fig. 3.25 The calculated frame loads with different initial speed in 0.2 m thick ice.

3.2.2.2 Statistical analysis

Individual ice loads must be separated when studying ice load statistics. Before probability plotting, a Rayleigh separation is applied to identify load peak values x_1, x_2, …, x_n, as introduced in Kujala et al. [52]. A proper value of the separator is chosen

initially. The Rayleigh separation method seeks the first peak value of the time history. The next peak value cannot be found until the time history signal decreases below the value of the Rayleigh separator chosen previously. If the time series signal does not decrease below this limit, but instead later increases above the first value, the first value is abandoned and a new value is selected as the first peak value. Fig. 3.26 shows how the Rayleigh method operates when the separator value is set as 1/4. In this figure, "+" and "-" signify the maximum and minimum respectively. Because the value at the point of "1-" is smaller than that at the point "1+" times the separator 1/4, the "1+" maximum is identified as a peak value. Similar cases also happen at the points of "3+", "4+", and "5+". Nevertheless, the value at the point of "2-" is greater than that at the point "2+" times the separator 1/4, and the maximum at "3+" point is larger than that at "2+" point, thus the "2+" maximum is abandoned. Circles show the peak values of Rayleigh-separated ice loads.

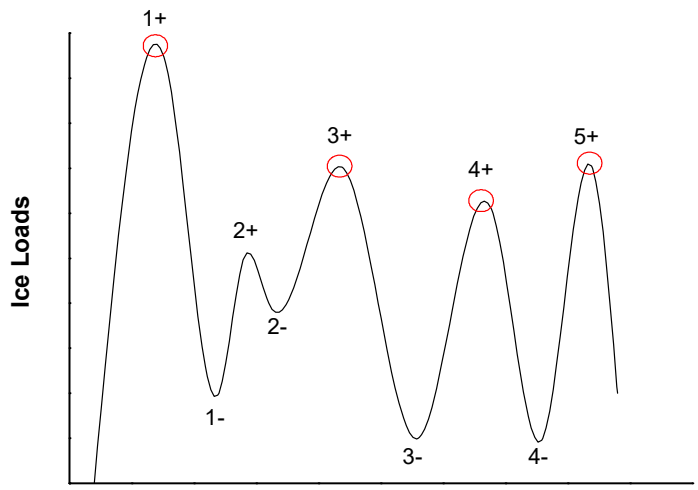

Fig. 3.26 Peak values according to Rayleigh method.

Since the local loads are sensitive to initial conditions, and the specified frame is even never in contact with the ice plate during the icebreaking pattern in some cases, therefore, 10 numerical simulations of ice-induced frame load processes with different initial speeds for each ice condition are conducted and deal with Rayleigh separation. The order statistic of peak loads is $x_{(1)}, x_{(2)}, \ldots, x_{(n)}$, where $x_{(1)} \leqslant x_{(2)} \ldots \leqslant x_{(n)}$, then the empirical CDF is generally defined as [53]

$$F(x_{(i)}) = \frac{(i-c)}{n-2c+1}, \text{ for } 0 \le c \le 1 \tag{3.37}$$

where c is a parameter for plotting position.

Generally, the distribution of local ice load peaks might be described approximately using a Weibull distribution based on statistical analysis of field measurement data of ice loads [54] [55]. Its CDF can be expressed as

$$F(x) = 1 - \exp\left\{ (\frac{x}{\varepsilon})^k \right\} \tag{3.38}$$

where ε represents the scale parameter and k stands for the shape parameter of the ice load distribution. To ascertain the proper values for the parameters of the Weibull distribution underlying the ice load process, a probability paper can be employed. According to the empirical CDF, the parameters of Weibull distribution can be estimated by fitting using least squares method.

Fig. 3.27 shows that the ice load peaks on a specified frame in various ice thickness are presented in the Weibull distribution. The cumulative distributions of ice load peak are shown as a function of the load level on the logarithmic axis [$ln(x)$] and cumulative occurrence probability on the twice logarithmic axis [$-ln(-ln(1-F))$]. The peak values are observed to form nearly a straight line, which means that the ice load peaks of the numerical simulation fit the Weibull distribution well.

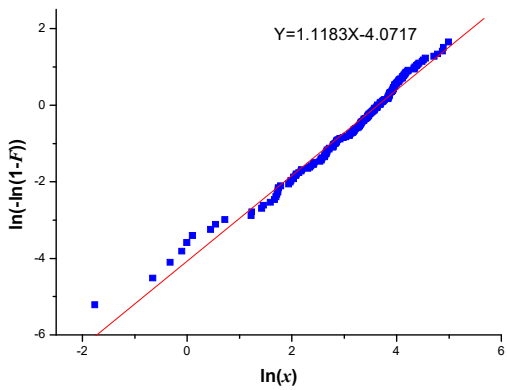

$h_i = 0.2$ m

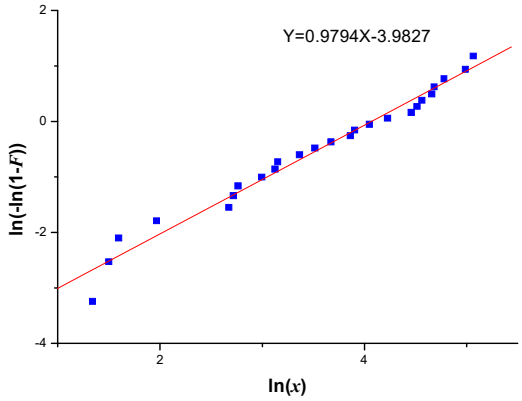

$h_i = 0.3$ m

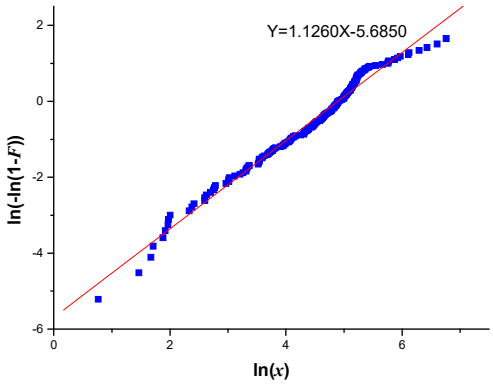

$h_i = 0.4$ m

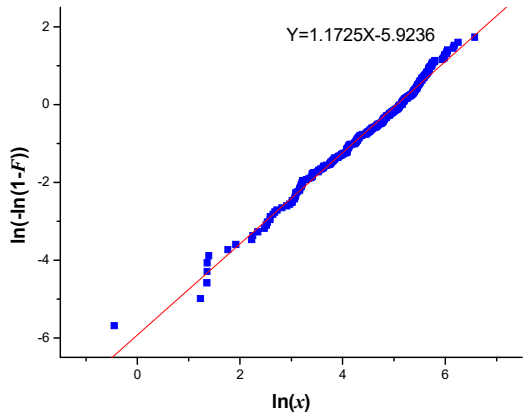

$h_i = 0.5$ m

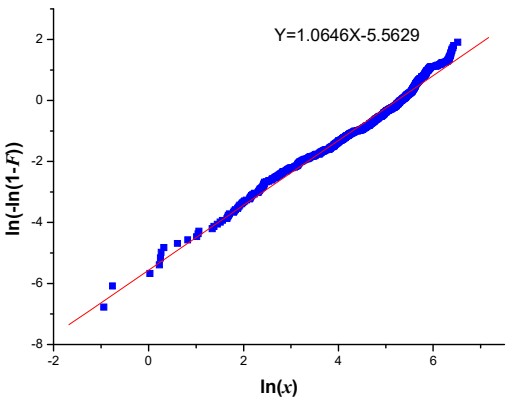

$h_i = 0.6$ m

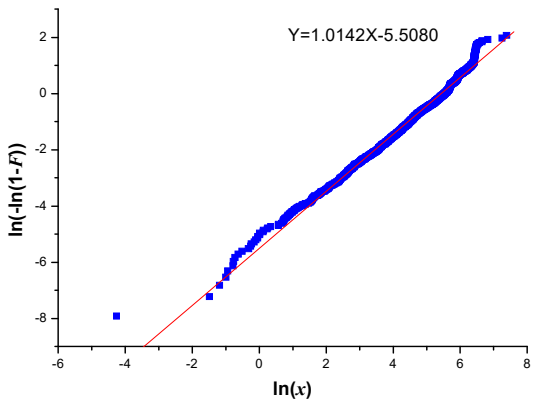

$h_i = 0.7$ m

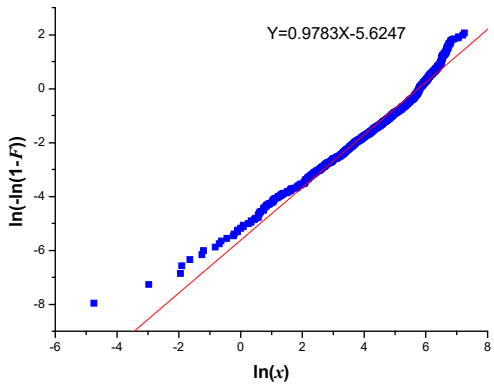

$h_i = 0.8$ m

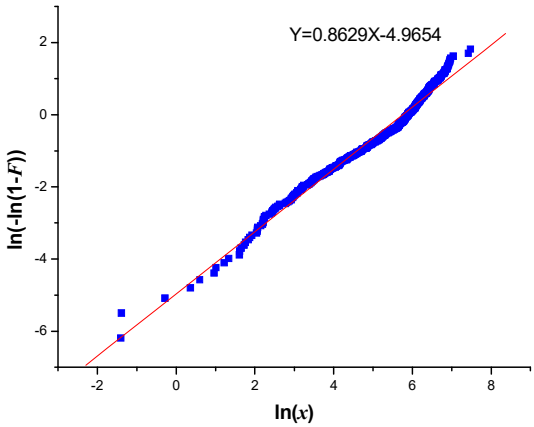

$h_i = 0.9$ m

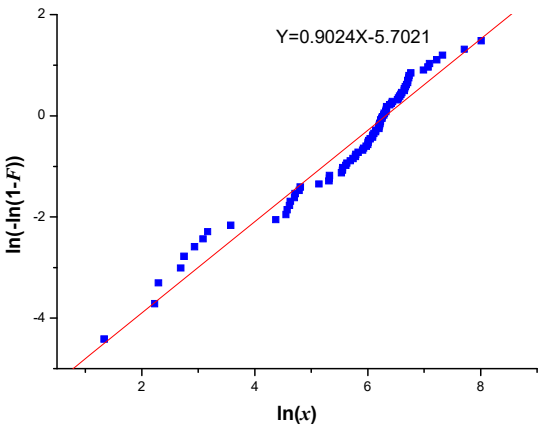

$h_i = 1.0$ m

Fig. 3.27 The calculated load peak distribution in level ice fields and fitted line of Weibull distribution in the ice thickness from 0.2 m to 1.0 m.

The statistical distribution parameters of numerical load peaks in level ice fields are shown in Table 3.3 in different ice conditions. The shape parameters vary in the range 0.8629 < k < 1.1725. From statistical analysis of field measurement data, the shape parameter is found to be generally $0.7 < k < 1.0$ [55]. By comparison, considering the

different ship models used in the field measurements and numerical simulations, the shape parameter value of the simulated peak distribution, i.e. the slope of the fitted line, is reasonable.

Table 3.3 Distribution parameters of the Weibull model for load peaks of various ice thicknesses in level ice fields

h_i	Shape parameter k	Scale parameter ε
0.2 m	1.1183	38.1235
0.3 m	0.9794	58.3409
0.4 m	1.1620	133.2572
0.5 m	1.1725	156.3743
0.6 m	1.0646	185.9776
0.7 m	1.0142	228.3294
0.8 m	0.9783	314.1205
0.9 m	0.8629	315.5513
1.0 m	0.9024	554.8377

3.3 Summary

A semi-empirical numerical procedure for predicting ship performance in level ice is established. The icebreaking process can be well reproduced as cycles of contact, crushing, and bending. The global ice loads and ship performance tend to be stable as the ship travels deep into ice sheet, and not significantly affected by the initial conditions. The simulated ice resistance compares well with that calculated by Lindqvist empirical formula. The icebreaking pattern has a great effect on the ice loads, which might induce higher loads in thinner ice plate. The downward trend and drop rate of h–v curve by the present model are quite consistent with the published results of Su's numerical model. The local ice loads are sensitive to ice thickness and initial conditions. The local load peaks can be modeled as a Weibull distribution. The shape parameters of the Weibull model representing numerical ice loads process agree well with statistical results of field measurement data.

Chapter 4

Numerical Model of Ship Operating in Ridged Ice Fields

Ice ridges are common ice features, appearing especially in dynamic ice conditions. Ice ridges constitute a significant obstacle and often control the design load levels for ships operating in ice-covered waters. Sometimes the ridge depth can exceed the ship draft. In such cases, much energy is consumed by displacing ice blocks. For that reason, it is important to predict the ice-induced loads on ice-going ships in ridged ice fields in terms of structural safety and overall operation. In this chapter, a numerical model is introduced to investigate both global and local ice-induced loads on ship hulls in ridge fields. Probabilistic ice fields are generated according to the statistical distributions of ridge heights and spacings. A modified Rankine's plasticity model is applied to achieve the keel loads, and the simulated results are compared with model tests, field measurements and earlier numerical results in ridged ice fields.

4.1 Generating ridged ice fields

4.1.1 Geometry of sea ice ridges

Ridges are complex structures with a wide variability in shape and size, which are formed when level ice floes are compressed and sheared by environmental driving forces such as wind and currents. Piling up of broken ice rubble occurs above and below the parent ice sheet. Sea ice ridges are generally formed of three parts, which are illustrated in Fig. 4.1.

The ice pile-up on the surface is called the sail and it is composed of ice blocks that can be relatively unconsolidated, or partially refrozen together. The voids between blocks are filled with air or snow [56].

The underwater part of the ridge is called the keel and it is also comprised of a large number of ice blocks. The ice rubble above and below the waterline is in hydrostatic equilibrium, and consequently the dimension of the keel is substantially larger than that of the sail. The keel is usually 4–5 times thicker than the sail [57].

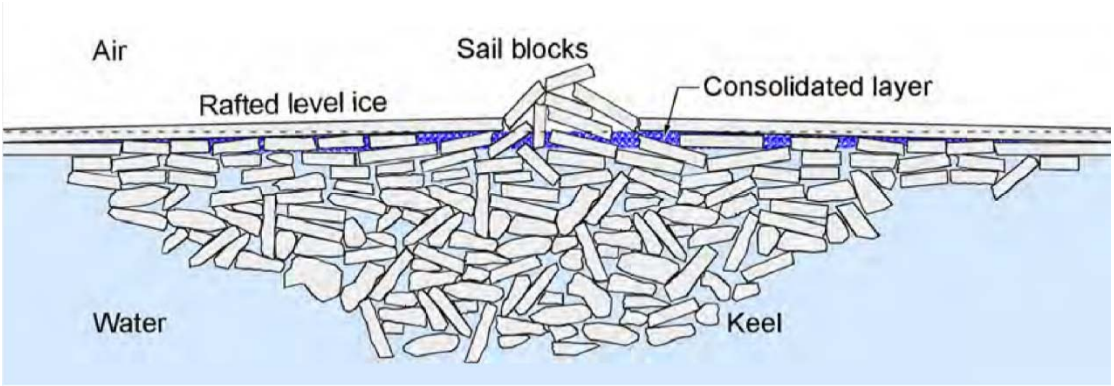

Fig. 4.1 Typical illustration of a first-year sea ice ridge [58].

With aging water filling the pores between ice pieces often refreezes, forming a consolidated layer downward. Its growth rate is higher than that of the surrounding level ice. The consolidated layer has a varying thickness that is on average 1.5–1.7 times the surrounding level ice thickness [59].

Ice ridges are often modeled by triangles or trapezes and characterized by their thickness, widths and angles. In this study, ridges are modelled in the simplest form as having triangular sails and keels. The model characterizes a ridge with sail height h_s, keel depth h_k, slope angles for sail and keel, α_s and α_k respectively as well as porosity, p. An idealized ice ridge is presented in Fig. 4.2. Typical values for the keel slope angle are reported to be 25–30° [19]. Strub-Klein and Sudom [56] give the average ratio of keel depth to keel width to be 4.85, which leads to α_k = 22° assuming a triangular cross section of the keel. Porosity of ridge keels varies between 0.25–0.4.

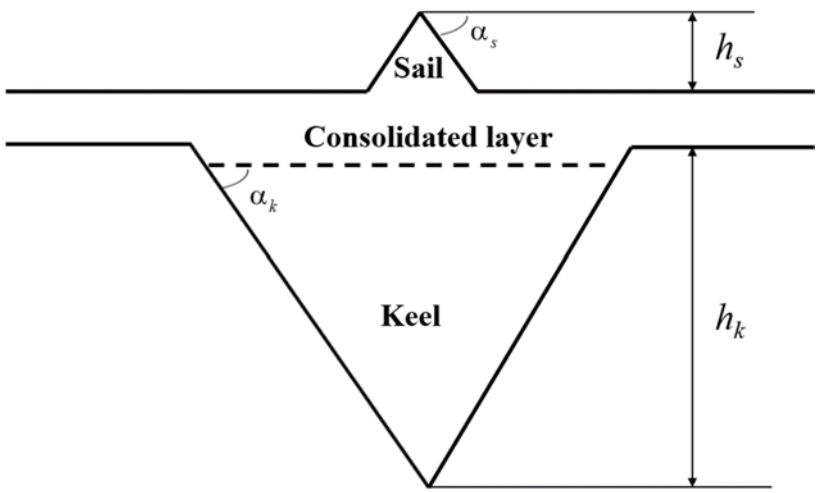

Fig. 4.2 Illustration of an idealized ice ridge.

4.1.2 Distribution of sail heights and ridge spacings

A ridged ice field consists of ice ridges, separated by stretches of level ice sections. In transit simulations, two methods are usually used to generate the ridged ice fields. The method presented by La Prairie et al. [60] contains a random number of ridges which

corresponds to the input ridge density and the ice field can be modelled quite realistically. The method presented by Kotovirta [61] flattens ridges to cover the whole ice field, i.e., whole field consists of level ice and ridges with solved equivalent thickness and therefore is faster for simulations. In this study, the ice conditions are approximated as realistically as possible. A ridge generator presented by La Prairie et al. is used for modelling the ridge field. Input data for the generator is ridge density per kilometer and mean ridge thickness. As the description of the ridge field is stochastic, and therefore the Monte Carlo method is used in the routine to create the ridges along the ridged ice route section.

Sail heights and keel depths of sea ice ridges can be modelled to be distributed according to the exponential distribution [62]. The probability density function (PDF) for ridge sail heights can be expressed as

$$p(h_s; h_c, \lambda) = \lambda \exp(-\lambda(h_s - h_c)) \tag{4.1}$$

where h_s represents sail heights, h_c denotes a cut-off height of sail heights, λ stands for the shape factor of the distribution i.e. the inverse of mean height of sails higher than h_c. The cut-off height is needed to distinguish ridges from the noise of the measurement system used to observe sail heights and keel depths for determination of λ. Presumably, the ridge keel depth is, on average, related to sail height. Therefore, the sail height distribution is useful to describe keel depths as well. As described herein, the ratio of keel depth to sail height is set as 5.

Similarly, keel spacings, i.e. distance between two adjacent ridges can be modelled as an exponential distribution [63].

$$p(d; \mu(h_c)) = \mu(h_c) \exp(-\mu(h_c) d) \tag{4.2}$$

Therein, μ is the shape parameter i.e. the expected number of keels per kilometer.

To obtain estimates of ship performance in ridged ice conditions, several random realizations of ridge field geometries are generated for each ice condition, by drawing random samples of distributions of ridge keel depths and spacings. The first ridge starts at $x = d$, where d is a random distance distributed according to Eq. (4.2). If generated ridges overlap, then the union of the overlapping keels is the used geometry, for completely overlapping ridges, the smaller ridge is thus discarded. Ridges are generated until a pre-set length of ridge field is full. The output of two keel distributions in ridged ice fields for 1 km with the same input ($\lambda^{-1} = 0.2$ and $\mu = 11$) is portrayed in Fig. 4.3.

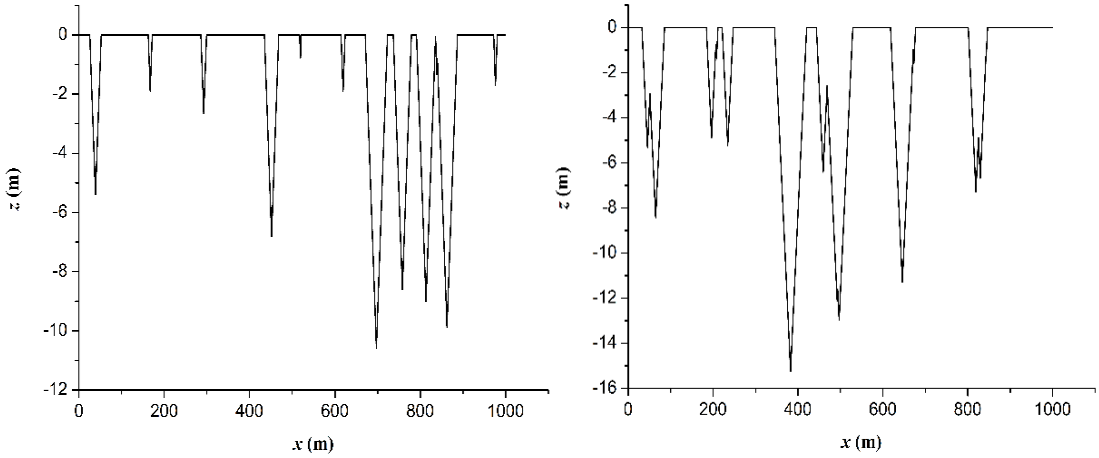

Fig. 4.3 Two simulated ridged ice fields with same input parameters.

4.2 Ship–ice interaction mechanics in ridged ice fields

Most analytical models of ridge failure divide a ridge into three components as mentioned before: the sail, keel, and consolidated layer. Total loads are obtained as a summation of them because of each section of the ridge. In practical calculations, the effects of ridge sails on ship resistance are neglected because they are assumed to be much smaller than the forces related to breakage of the consolidated layer and displacement of the keel rubble. The consolidated layer sometimes exerts the greatest forces on structures during ridge–structure interaction. Timco et al. [1] reported that, during a ridge interaction, the consolidated layer is usually assumed to fail in a manner similar to a level ice sheet (i.e. the influence of the sail and keel on the behavior are ignored). Therefore, modelling of interaction between the ship and the consolidated layer resembles that in level ice discussed in Chapter 3. In the present study, the consolidated layer of ridges is assumed to be 1.5 times the thickness of the surrounding level ice. Keel loads include two components, friction at the midship and displacement of the ridge keel at the bow. The methods of calculating the ice loads induced by ridge keels have been based largely on ideas borrowed from soil mechanics theory such as Coulomb's theory and Rankine's theory. The details of models on the basis of soil mechanics are presented in subsections 4.2.1–4.2.3. Moreover, DEM is also applied to model the interaction between ships and ice ridges in some recent studies. Discrete models can provide a relatively realistic simulation of the interaction conditions between ice blocks. However, they need to use very large numbers of elements in order to deal with any problem of practical interest. The computation with DEM is quite time consuming. In this study, ice loads arising from ridge keels are calculated with a modified Rankine's plasticity model as an integral of loads per unit width, taking account of the effects of ship movement and the inertial force of ice accumulation in front of the ship bow.

4.2.1 Theoretical formula of Keinonen

Keinonen [18] proposed an analytical method to calculate the pure ridge resistance. Penetration of ridges by a ship is a complicated and extensive problem, if the whole process is considered, and therefore a number of simplifications and idealizations are made in Keinonen's model. The ice mass in ridge keel is assumed to behave like soil under a passive pressure, which means that external pressure is applied on the mass. The consideration of ridge field is limited to a structurally homogeneous floating sheet of granular material with a constant thickness, i.e. a uniform ridge field. The ship is idealized with either a landing craft bow or a simple inclined wedge.

Keinonen's model employed Coulomb theory for analyzing the breaking forces in ship–ice interaction in ice ridges. The method of Coulomb is based on an assumption of the breaking of the mass in a plane, when the mass is loaded with a wall. The breaking condition is solved by using a force balance calculation in possible breaking planes. The actual breaking plane where the breaking conditions are first reached is found by derivation. The method for a vertical frictionless wall is shown in Fig. 4.4. BC is the rupture plane with an inclination γ' from the horizon. $\mathbf{F}\tau_0$, $\mathbf{F}_G$, $\mathbf{F}_{TOT}$ and $\mathbf{F}_S$ represent cohesion resistance, buoyancy force, force against the wall and shear friction resistance respectively. In the figure it can be seen that the action lines of the forces pass through a single point, which lies in the rupture plane. The limit equilibrium equation for projections of the forces onto the L–L line normal to $\mathbf{F}_S$ is

$$F_G \sin(\gamma' + \phi') + F_{\tau_0} \cos\phi' - F_{TOT} \cos(\gamma' + \phi') = 0 \tag{4.3}$$

where ϕ' stands for the internal friction angle of the mass.

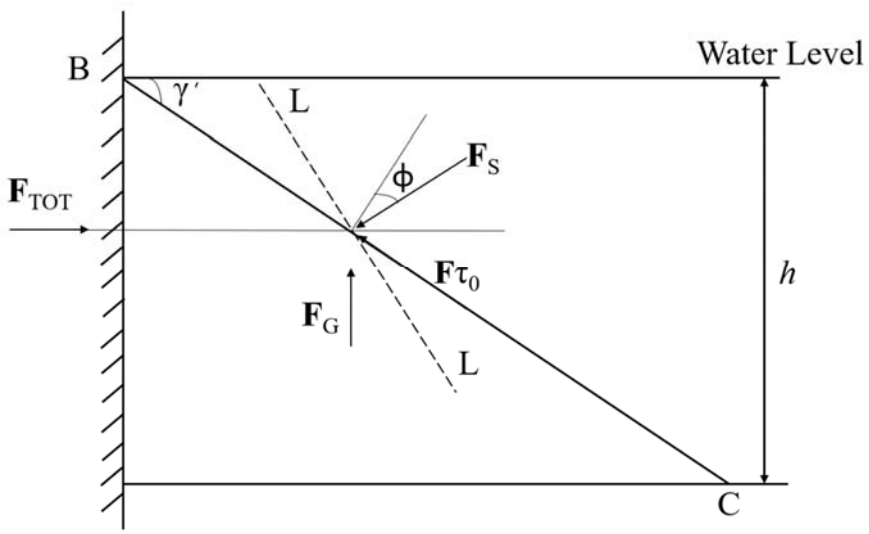

Fig. 4.4 Coulomb's method.

Ridge material follows the Coulomb failure model with

$$\tau = \tau_0 + \sigma \tan\phi' \tag{4.4}$$

Therein, τ_0 is the cohesion (the shear strength at zero normal load) of the mass and σ is

the normal stress. τ is the actual shear strength.

And for a wall with a height h, $F\tau_0$ is determined as

$$F_{\tau_0} = \tau h / \sin\gamma' \tag{4.5}$$

Then the formula for F_{TOT} per unit width can be obtained from Eqs. (4.3)–(4.5).

$$F_{\mathrm{TOT}} = \frac{(1-p)\rho_{\Delta} g h^2 \tan(\gamma' + \phi')}{2\tan\gamma'} + \tau h \frac{\cos\phi'}{\sin\gamma' \cos(\gamma' + \phi')} \tag{4.6}$$

where $\rho_{\triangle}$ denotes the difference of the densities of sea water and ice.

When a minimum for this equation is searched for by varying γ' the breaking condition is determined. The minimum is found from the first derivative. For the vertical frictionless wall, the solution is $\gamma' = (\pi/4 - \phi'/2)$.

Keinonen's model was developed with Coulomb's method, i.e. limit equilibrium analysis to calculate the resistance as stated previously, but the inclined wall and friction against the wall can cause one or several of the action lines of the forces to change. Initial resistance is divided into two cases, thin ridge when the thickness of the ridge may not reach below the ship draught, and thick ridge when the ridge height is larger than the draught. A–A plane is a cross section on the ship bow. In case of thin ridge, breaking occurs on one rupture plane, as depicted in Fig. 4.5. In contrast, an additional lower rupture plane is introduced in case of thick ridge, as portrayed in Fig. 4.6. This model also paid particular attention to the development of the ice rubble profile around the vessel. Fig. 4.7 shows the development for a landing craft bow.

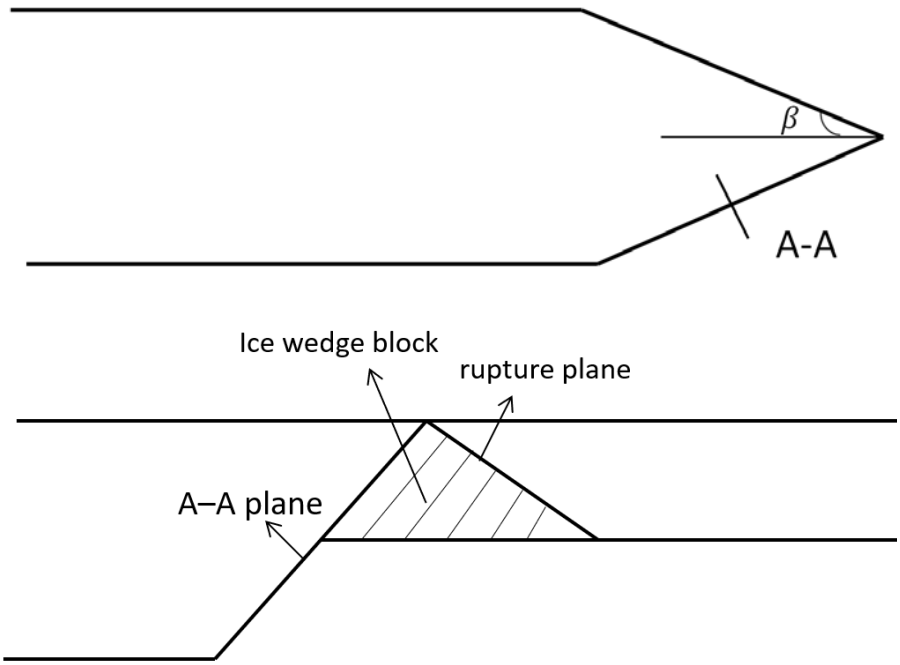

Fig. 4.5 Rupture plane when the ridge height is less than the draught.

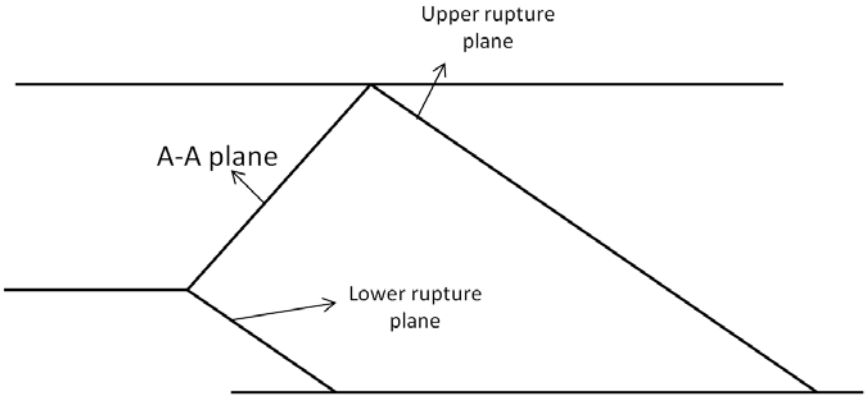

Fig. 4.6 Rupture planes when the ridge height is larger than the draught.

For both initial resistance and developed resistance, force geometry need to be analyzed in each condition. The total pure ridge resistance can be calculated as a summation of the following components,

$$R_{\mathrm{r}} = R_{\gamma 1} + R_{\gamma 2} + R_{\varepsilon} + R_{\mathrm{pB}} + R_{\mathrm{pS}} \tag{4.7}$$

In that equation, $R_{\gamma 1}$, $R_{\gamma 2}$, R_{ε}, R_{pB} and R_{pS} represent upper shear plane force, lower shear plane force, end shear plane force, bottom frictional resistance and side frictional resistance respectively. The equations for each of the terms would be too long to present here. The details can be referred to in Keinonen [18].

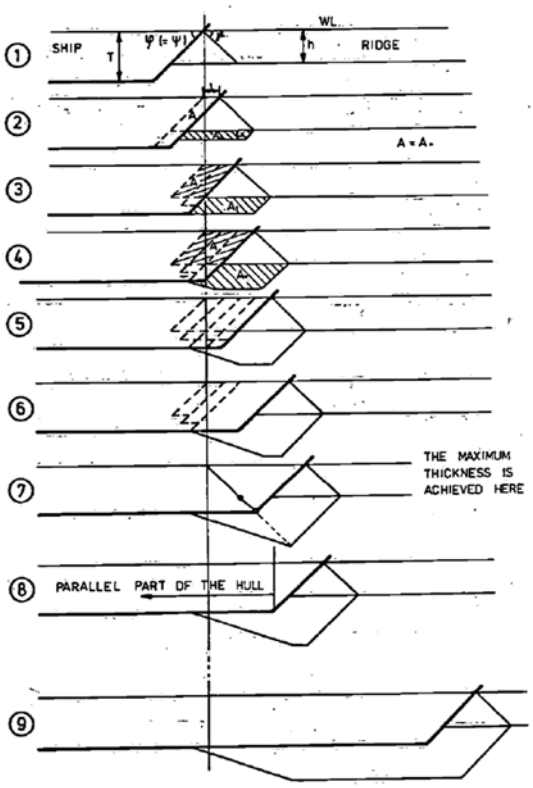

Fig. 4.7 Development of ridge profile around a landing craft bow [18].

4.2.2 Theoretical formula of Mellor

Mellor [19] developed a formula to solve the ship resistance of Great Lakes bulk carriers in brash ice, which is taken to be a floating accumulation of reasonably equant fragments. The characteristics of brash ice is similar to that of the unconsolidated ridge considered by Keinonen [18].

Mellor's model was built on the basis of Rankine theory, which considers the state of stress in ice rubble mass when the condition of plastic equilibrium has been reached. The effect of intrinsic cohesion between ice blocks is not likely to be significant, and thus ignored. Consider a smooth vertical plate pushing slowly against a uniform layer of cohesionless brash, as presented in Fig. 4.8, then there will be lateral compression of the ice mass and the horizontal stress σ_x will increase until a state of plastic equilibrium is reached. Consequently, all ice elements which are close to the plate are in the passive stress state. For this condition, σ_x is the major principal stress, and the vertical stress σ_z is then the minor principal stress. According to Mohr-Coulomb failure criterion [64], the angle of slip planes to the vertical is ($\pi/4+\phi'/2$).

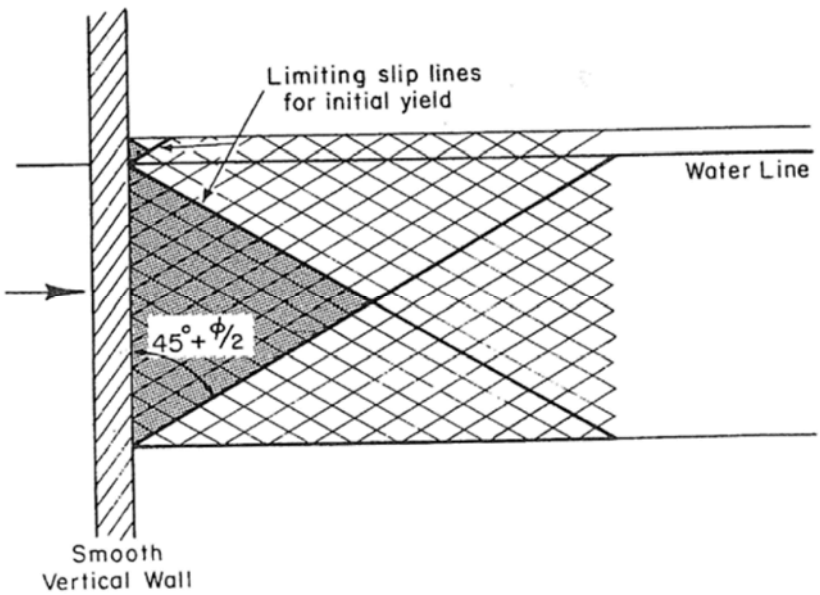

Fig. 4.8 Illustration of slip lines for cohesionless brash ice pushed by a smooth, vertical and wide plate [19].

Since no external applied forces or displacements act on the mass, the vertical stress σ_z can be determined by the buoyancy of the fragments.

$$\sigma_z = (1-p)\rho_\Delta g(h_k - z) \tag{4.8}$$

where z is the depth.

Based on classical Rankine theory, the passive pressure coefficient K_p equals $(1+\sin\phi')/(1-\sin\phi')$, and therefore σ_x can be expressed as

$$\sigma_x = K_p \sigma_z = (\frac{1+\sin\phi'}{1-\sin\phi'})\sigma_z \tag{4.9}$$

Combining Eqs. (4.8) and (4.9) and integrating the passive stress σ_x with regard to the depth from $z = 0$ to $z = h_k$, then the total horizontal force per unit width on the plate can be obtained by

$$R = \frac{1}{2}(\frac{1+\sin\phi'}{1-\sin\phi'})(1-p)\rho_\Delta g h^2 \tag{4.10}$$

Under the condition of cohesionless ice fragments, the force based on Rankine theory in Eq. (4.10) is actually the same to that obtained by Coulomb method in Eq. (4.6).

The vessels of most concern in Mellor's model are bulk carriers, the sides of which are essentially vertical near the water line, and the horizontal dimensions are much larger than the thickness of a typical brash layer, so Eq. (4.10) can be used to achieve the normal component of bow resistance.

The ship bow is subjected to normal crushing force, coupled with tangential frictional force, as portrayed in Fig. 4.9. Taking the local bow angle β for any given vertical strip of width ds, the component of the normal force Rds in the x direction is ($R\sin\beta$ds). If the normal distance from the ship centerline to the strip element is y, then $\sin\beta = \mathrm{d}y/\mathrm{d}s$ and hence the forward force component can be expressed as Rdy. Similarly, the forward component of corresponding tangential friction force equals ($\mu_i R\mathrm{d}x$), where μ_i is the frictional coefficient. The total resistance on ship bow R_b is given by the sum of the forward components for the elementary strips along the bow section,

$$R_\mathrm{b} = 2\int_0^{B/2} R dy + 2\int_0^{L_{bow}} \mu_i R dx = BR + 2\mu_i L_{bow} R \tag{4.11}$$

Therein, L_bow signifies the bow length.

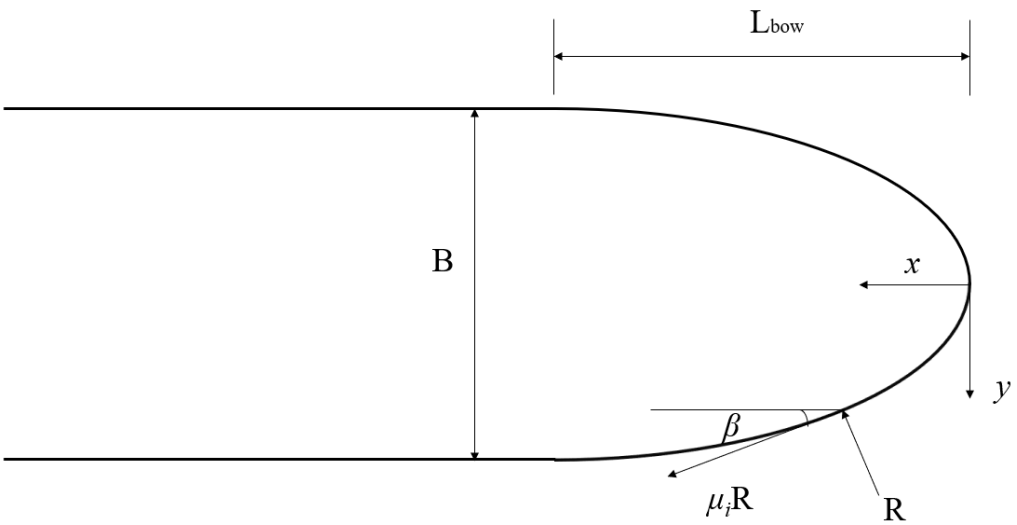

Fig. 4.9 Ship bow crushing resistance and frictional resistance.

The midbody resistance R_m is assumed to consist only frictional resistance which is

tangential to the ship.

$$R_{\mathrm{m}} = 2\mu_i L_{par} R' \tag{4.12}$$

where L_{par} is the length of parallel midship, R' represents the normal force per unit width for an indeterminate stress state. The relationship between R' and R is regarded as linear,

$$R' = NR \tag{4.13}$$

In that equation, N is a factor, with the value varying from 0.06 to 0.13.

Combining Eqs. (4.11) and (4.12), the total keel resistance R_{k} can be calculated by summing up the bow resistance and the midbody resistance.

$$R_{\mathrm{k}} = R_{\mathrm{b}} + R_{\mathrm{m}} = BR + 2\mu_i L_{bow} R + 2\mu_i L_{par} NR \tag{4.14}$$

4.2.3 Theoretical formula of Malmberg

Malmberg [20] applied Rankine's plasticity model to study a ship displacing the ridge material as well. In Malmberg's model, the normal force on ice pile in the passive state around the bow is considered, as shown in Fig. 4.10. The ridge resistance is a combination of resistance due to displacing the ridge keel at the bow, and frictional resistance on the parallel midbody sides and bottom.

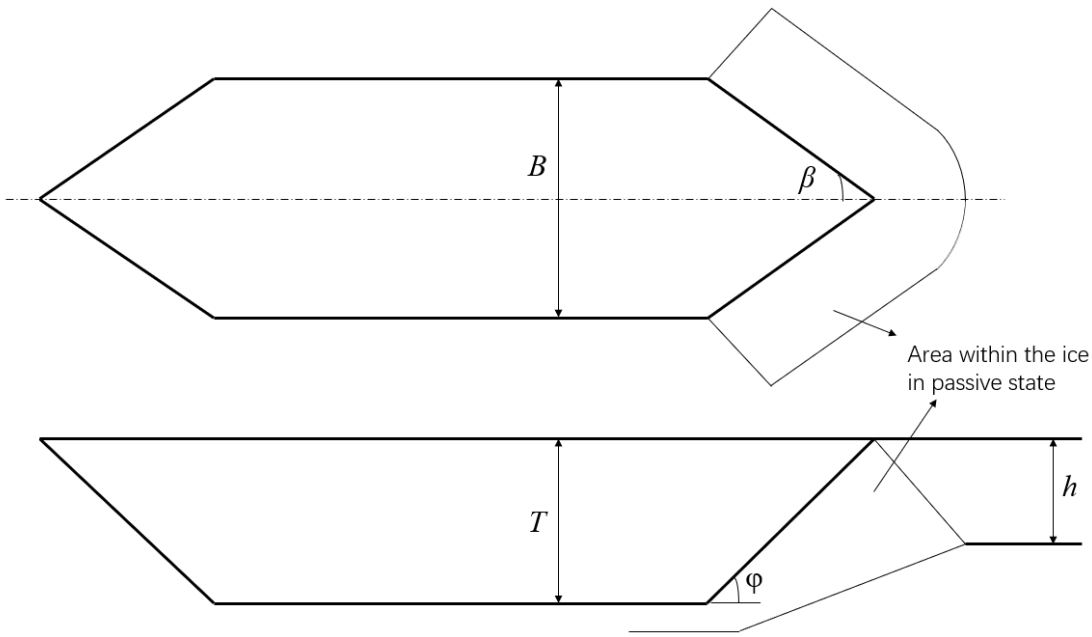

Fig. 4.10 Basic assumption in Malmberg's model.

The component of bow resistance, taken as a point force applied at ship shoulder, is calculated by

$$R_{\mathrm{b}=}\rho_{\Delta} g T h_k (1-p)(\frac{1+\sin\phi'}{1-\sin\phi'})(0.5B + h_k \tan\gamma\cos\beta)(\mu_i \cos\eta + \sin\beta) \quad (4.15)$$

The midship frictional resistance component arises with increasing penetration of the ship into the ridge, which is given by

$$R_{\mathrm{m}} = \rho_{\Delta} g T (1-p)\mu_i \int_{L_{par}} (K_0 h_k + (\frac{h_k}{T} - 0.5)B)dx \quad (4.16)$$

Therein, the factor (h_k/T-0.5) is non-negative, i.e. taken as zero when $h_k < 0.5T$, K_0 is the coefficient of lateral stress, which can be calculated by the following equation

$$K_0 = 1 - \sin\phi' \quad (4.17)$$

4.2.4 A modified Rankine model in the present study

Those analytical models presented in previous subsections are used widely to obtain the global ice loads caused by ridge keels. However, it is difficult to achieve the local ice loads by these methods. DEM is applicable to calculate the local loads, but such computations can be time consuming even for a single ice ridge. It would be more inefficient to estimate the local ice loads in ice fields containing multiple ridges. Furthermore, ridged ice fields in those previous models are assumed to be a uniform layer of broken fragments with a constant thickness, while in this study, the fields are modeled more realistically as having triangular keels. In order to tackle these problems, a modified Rankine model is proposed in this chapter to obtain both global ice loads and local ice loads on ship hulls in ridge fields.

The midship component is achieved by the Malmberg's resistance formula Eq. (4.16), which is useful to calculate global loads as an integral along the whole midship part, and to calculate the local loads as an integral on a specified frame at midship. Replacing the constant thickness h_k in Eq. (4.16) with variable keel height, the following expression is obtainable.

$$R_{\mathrm{m}} = \rho_{\Delta} g T (1-p)\mu_i \int_{L_{par}} (K_0 h_r(x) + (\frac{h_r(x)}{T} - 0.5)B)dx \quad (4.18)$$

where $h_r(x)$ represents the ridge depth beneath a point along the midship at any moment.

The bow component is calculated as an integral of loads per unit width with this model, including consideration of the effect of ship movement and inertia force of ice accumulation in front of ship bow.

The Rankine model is limited to the conditions of a vertical pushing plate and a horizontal or semi-infinite sloping surface, like the model of bulk carriers in Mellor [19], for instance. However, 1) for this study, the keel opening angle and the waterline half-angle are not large (keel angle $\alpha_k = 22°$, and waterline half-angle $\beta = 23.6°$ are set in the simulation). Therefore, the slope angle of ridge surface normal to cross sections (A–A plane) is less than 10°. Consequently, it presumably does not introduce too much

inaccuracy to treat the ridge surface normal to A–A plane as horizontal. In addition, 2) undertaking the ship bow as a slender wedge, the ice will simply pile up against the plate until the resistance reaches the value for a vertical plate. Based on those two reasons above, it is reasonable to assume that Rankine's plasticity model can be available for the interaction of each A–A plane and the ice ridge surface.

As introduced in subsection 4.2.2, Mellor derived the bow resistance per unit width attributable to normal force as shown in Eq. (4.10) when the ridge height at a certain point is less than the draught. When the ridge height at a certain point is larger than the draught, a second lower rupture plane is introduced, as demonstrated by Keinonen [18], who applied Coulomb model, i.e. limit equilibrium analysis to calculate the resistance. Although the ridge height in contact with ship bow is the draught, from the perspective of Coulomb model, resistance results from the area of the ice wedge block, which is subjected to buoyancy and to forces from the ship bow and rupture planes. This area is approximately proportional to the draught and the ridge height. Therefore, for simplification, a modification is made on Eq. (4.10), by which the bow resistance because of normal force at a certain point with height greater than the draught can be translated into

$$R = \frac{1}{2}(1-p)\rho_{\Delta} g \frac{1+\sin\phi'}{1-\sin\phi'} h_r(x) T \tag{4.19}$$

Aside from the normal crushing force, friction occurs as a result of the relative lateral motion of the ship hull and ice blocks. The friction runs tangential to the bow. The ridge keel is triangular. Therefore, the ridge height in contact with each A–A plane is varied gradually along the ship bow. Considering the tangential frictional force additionally, the global loads on the bow can be expressed as an integral along the ship bow.

$$R_{\mathrm{b}} = \int_{L_{bow}} R(\tan\beta + \mu_i) / \tan\alpha_k dh_r \tag{4.20}$$

Regarding local loads on a specified frame, for any point at depth z, the vertical component of normal stress is $(1-p)\rho_{\Delta} g(h_r-z)$. Therefore, according to Rankine theory, the horizontal stress can be ascertained as the coefficient of passive stress $(1+\sin\phi')/(1-\sin\phi')$ times the normal stress. The ice loads on the specified frame at A–A plane are calculable as an integral of horizontal stress along the contact height with ice ridge. The resultant local ice loads are an accumulation of the A–A plane along the frame spacing.

Myland [65] performed the ridge ramming model tests of two ship models with systematically varied keel depths in HSVA's large ice model basin, and reported that an increase of resistance with growing penetration velocity can be assumed to be proportional based on the model test results of ridge penetration, as presented in Fig. 4.11. Therefore, the total keel loads can be expressed as shown below.

$$R_{\mathrm{k}} = \frac{k_{pen} v_{pen}}{\sqrt{g h_r(x)}} R_{\mathrm{b}} + \left(\frac{R_{\mathrm{m_max}}}{R_{\mathrm{b_max}}}\right) \frac{k_{pen} v_{pen}}{\sqrt{g h_r(x)}} R_{\mathrm{m}} \tag{4.21}$$

Therein, k_{pen} is a factor that depends on the ship model's ridge breaking capability and the number of ram repetitions necessary to break the ridge. It is 1.3–2.0; also, v_{pen} is the penetration velocity.

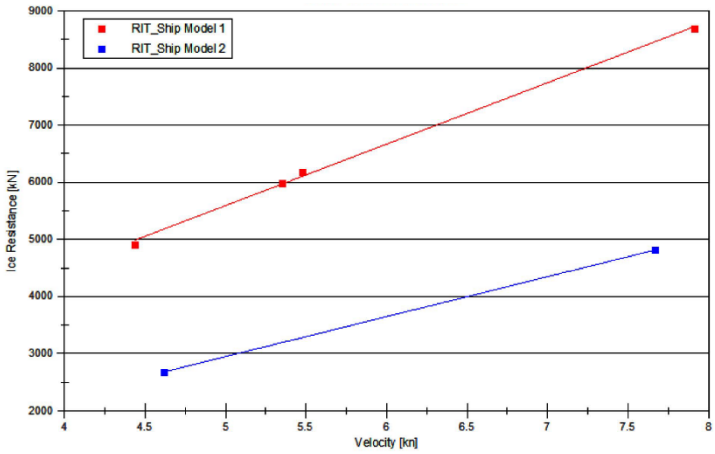

Fig. 4.11 Average ice resistance for varying keel depth vs. average penetration velocity [65].

The inertia force of ice accumulation in front of each A–A plane can be considered. Two parts of the ice blocks contribute to the total inertia force: the ice pile below ridge surface in front of A–A plane and the ice wedge block between A–A plane and rupture plane, as portrayed in Fig. 4.12.

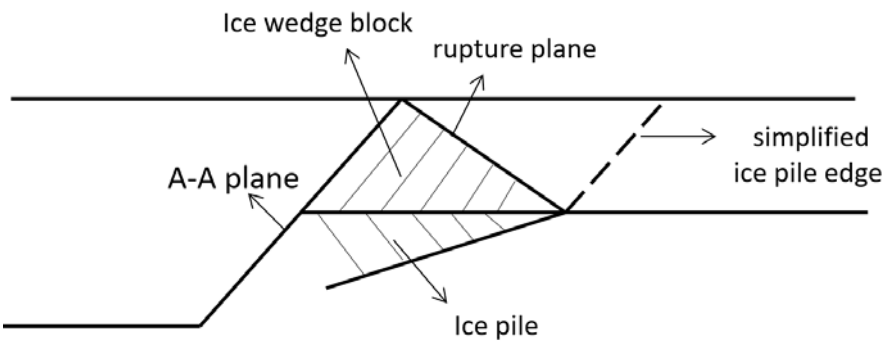

Fig. 4.12 Inertia force assumption.

In fact, the ice pile acceleration is the same as the ship acceleration. For the ice wedge block, the acceleration varies at different points. A reasonable assumption of inertia distribution is required. Nevertheless, the ice pile shape is difficult to predict using analytical method. For that reason, a simplified ice pile edge parallel to the A–A plane is introduced in this study, by which the inertia force of the ice pile can be compensated with that of ice blocks between the rupture plane and the simplified ice pile edge. Moreover, the acceleration is assumed to vary linearly from zero at the edge in contact with the unmoved ridge to ship acceleration at the edge in contact with the A–A plane. The total global or local inertia force is calculable as an integral at each A–A plane along the ship bow or frame spacing.

4.3 Numerical results of ice loads in ridged ice fields

4.3.1 Global ice loads and ship performance

Numerical simulations are conducted in different ice conditions with level ice thicknesses of 0.2–1.0 m. The ridge porosity was 0.25–0.4. The internal friction angle varied: 47°–58°. For this study, 0.3 and 52.5° were used as the two parameters, as referred from a report by Kuuliala et al. [66]. In transit simulations, the values of cut-off height and the inverse of shape parameter of sails height distribution were set respectively as 0.4 and 0.2 [67]. The expected number of keels density per kilometer was set as 11 [62]. Characterized by the mean ridge keel depth, ridge density, and level ice thickness, random ridged ice fields can be modeled according to Eqs. (4.1) and (4.2). An example of ridged ice field for 1 km is portrayed in Fig. 4.13. Sea ice ridges are difficult impediments to navigation in ice. Ships are usually unable to pass through them in a continuous mode. If the ship stops in the ridge, then it backs out into its own broken channel and rams the ridge again until the ship has passed through the ridge. In such cases, keel loads along the mid-ship because of friction are the only resistance term considered. The main characteristics of the calculated ship and the material properties of level ice sections are identical to those in Chapter 3.

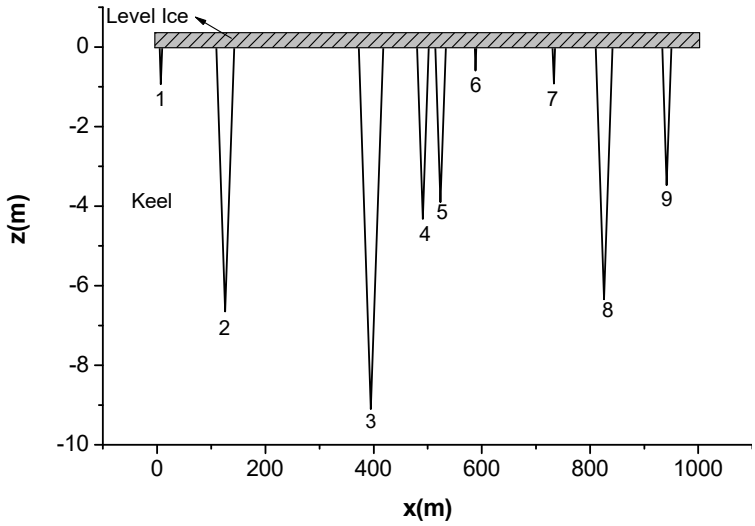

Fig. 4.13 A ridged ice field model.

In numerical simulations, the ship model is driven by constant thrust. The initial velocity of a ship transiting through ridged ice fields is set as the mean velocity in level ice of equal thickness. Under the keel conditions shown in Fig. 4.13, simulated time histories of global ice loads in level ice thicknesses of 0.2 m and 1.0 m are shown respectively in Fig. 4.14 and Fig. 4.15. It is apparent that the ice-induced load resembles a sequence of spikes. For 0.2 m ice thickness, the pure ice ridge force dominates. For 1.0 m ice thickness, the ice load induced by breaking the consolidated layer dominates. That result is explainable from two factors, 1) according to Eq. (3.27), the ice plate bearing capacity is proportional to the square of level ice thickness. Thus, the

consolidation loads in 1.0 m level ice thickness are much higher than those in 0.2 m thickness. 2) Based on Eq. (4.21), the keel loads are proportional to the penetration velocity. Because the transiting speed in lower ice thickness is higher, even in the same keel distribution, the keel loads in the case of 0.2 m ice thickness are larger than the other ones. This phenomenon has also been observed in field trials. Based on field measurement data, Keinenon [68] found that resistance attributable to consolidation might be the major resistance component for small ridges and for heavily consolidated ridges.

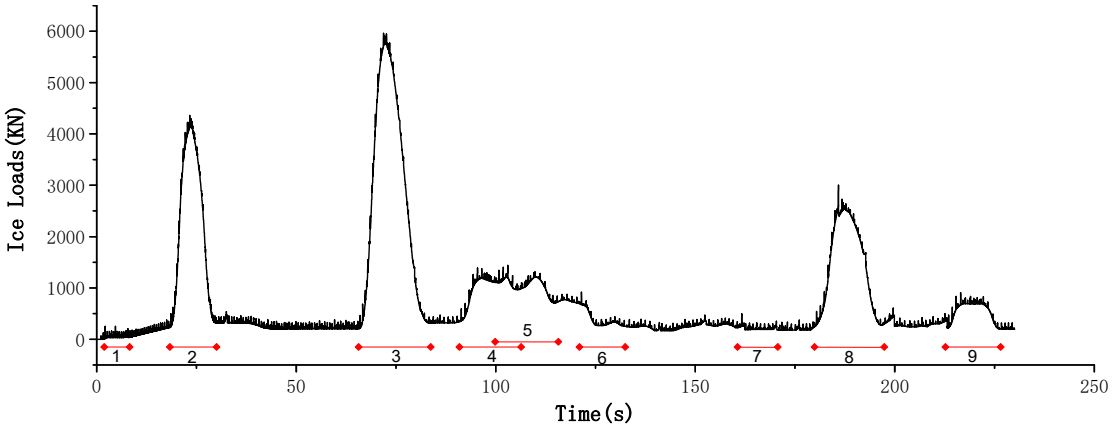

Fig. 4.14 Simulated time histories of global ice loads in level ice thickness of 0.2 m.

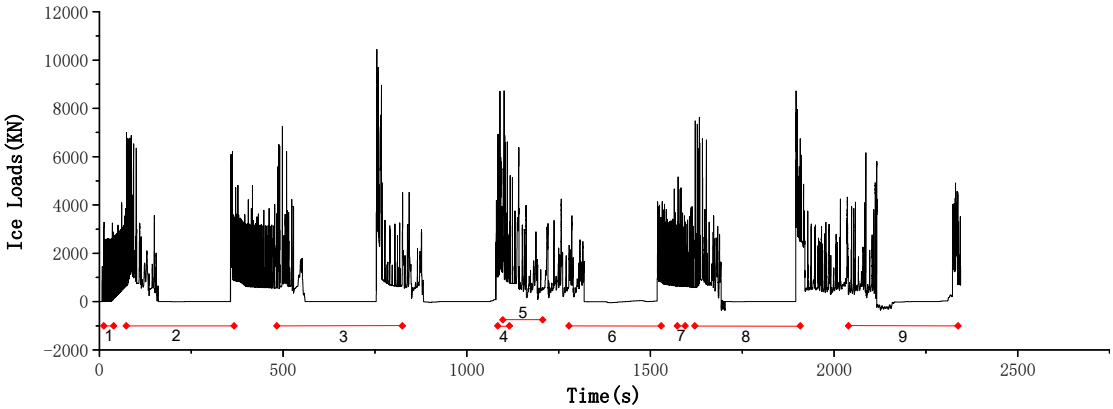

Fig. 4.15 Simulated time histories of global ice loads in level ice thickness of 1.0 m.

Fig. 4.16 and Fig. 4.17 present the simulated speed time series in level ice thicknesses of 0.2 m and 1.0 m respectively, corresponding to the global ice loads in Fig. 4.14 and Fig. 4.15. The ship forward speed drops sharply from the initial velocity, i.e. the mean velocity in level ice of the same thickness, because of the high loads caused by the consolidated layer and ridge keels. In the case of 0.2 m ice thickness, the ship transits the ridged ice field continuously without ramming. By contrast, six rams must be used to pass through an ice field with 1 m level ice thickness, when the ship speed value turns negative. The value of the global ice loads during the ramming period in Fig. 4.15 are nearly zero because the ship backs into level ice stretches that have already been broken. For that reason, no contact with the ice edge occurs. Only friction between the mid-ship and ice ridges might occur. Nine ridges exist in all in this realization of ridge

fields. The segment ends in Fig. 4.14–Fig. 4.17 represent time points at which the ship bow begins to penetrate into and has completely gone through each ridge. It is apparent that in the case of 1 m level ice thickness, rams are necessary for transiting the large ridges. Sometimes rams even happen in level ice sections such as that behind the third ridge or in small ridges such as the sixth ridge because the ship slows dramatically after passing through the previous large ridge. It cannot maintain forward speed.

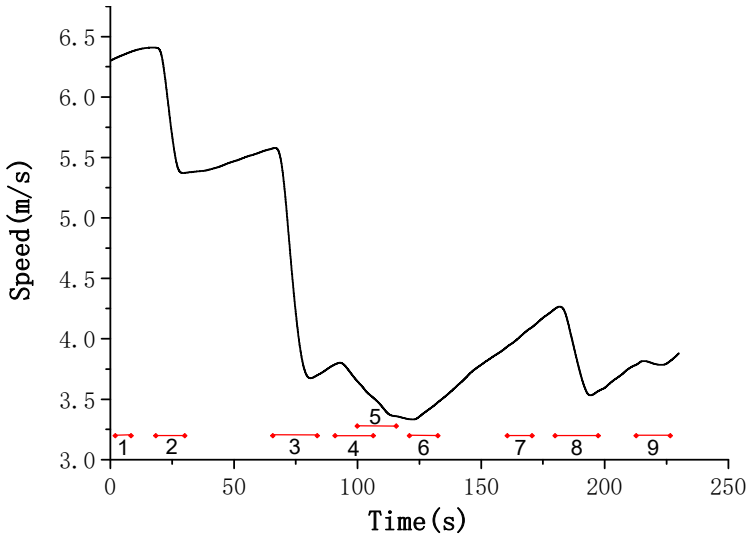

Fig. 4.16 Simulated speed time series in level ice thickness of 0.2 m.

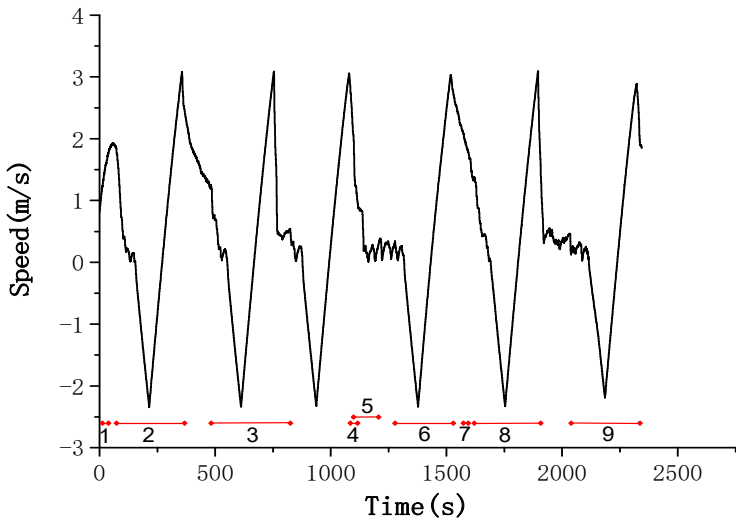

Fig. 4.17 Simulated speed time series in level ice thickness of 1.0 m

To validate the numerical calculation method of ice loads in ridged ice fields presented in this chapter, simulations of transiting a single ice ridge were conducted and were compared to results of ridge ramming model tests with systematically varied keel depths performed in an earlier study using HSVA's ice model basin by Myland [65]. Several ice conditions resembling model tests were simulated using a numerical model, for example, in the No. 3010 test run of Myland's study, the keel depth scaled to full scale was 7.6 m. The level ice thickness of 0.05 m was tested with a scale factor equal to 22. A similar case of 7.6 m ridge keel depth and 1.1 m level ice thickness was set in

the numerical simulation, but other ice properties such as ice strength might be not exactly the same. The full scale maximum load value in the model test is 4.5 MN, whereas the numerical result is 6 MN. This slightly larger value in numerical simulation can be attributed to the larger scale of the numerical ship model (the length between perpendiculars of the ship model in the No. 3010 test run was 126.6 m). The numerical load values are of the same order of magnitude as the model test results.

Ice resistance is also calculated for variable ice conditions, as shown in Fig. 4.18. Considering the random nature of ridged ice, 50 simulations were performed for each ice condition in this study. Fig. 4.18 presents the ice resistance increasing concomitantly with the increasing level ice thickness for constant ship speed of 5 m/s. The present resistance is higher and it increases faster than Lindqvist's ice resistance at the same speed because of the effects of keels and consolidated layers.

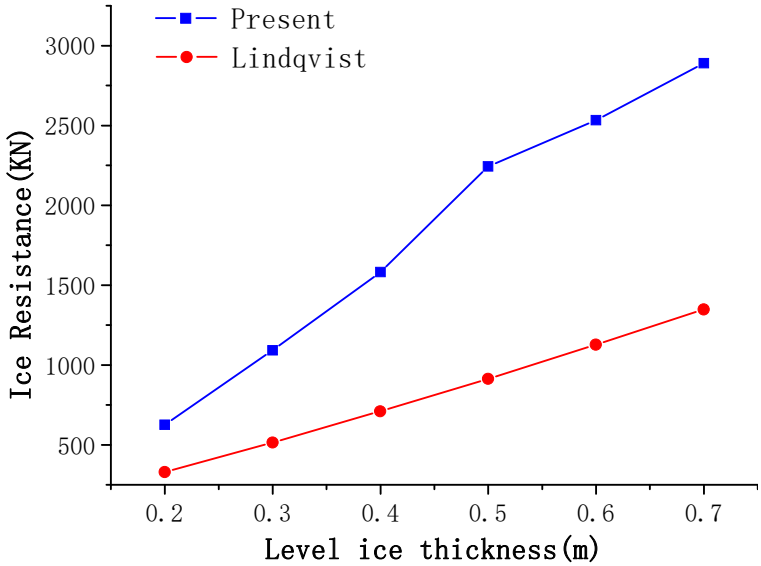

Fig. 4.18 Ice resistance in various ice thicknesses with a constant speed of 5m/s.

Fig. 4.19 shows mean speeds obtained for variable ice conditions in the present study and in Kuuliala's transit simulation model [66]. The ridge density is set the same in the two simulations as 11 per kilometer. The mean ridge thickness in Kuuliala's model is 3 m, whereas the same value of 3 m and a larger value of 6.67 m are used for this study for comparison with Kuuliala's results. Consequently, an obviously lower mean speed is obtained with 6.67 m mean ridge depth in the same level ice thickness. For 0.3 m level ice thickness, the speed value with 3 m mean ridge depth in the present simulation closely approximates Kuuliala's numerical value, but the mean speed decreases faster as the level ice thickness increases in this study. Kuuliala's numerical results show that the expected values of mean speed decrease almost linearly with increasing ice thickness. An approximately linear relation between mean speeds and level ice thickness is also observed in cases of 6.67 m and 3 m mean ridge depth in this study. Moreover, the slopes of these two cases are quite consistent. They are larger than that in Kuuliala's simulation. As a result, the present numerical results are comparable with those found from Kuuliala's study, in spite of some slight differences.

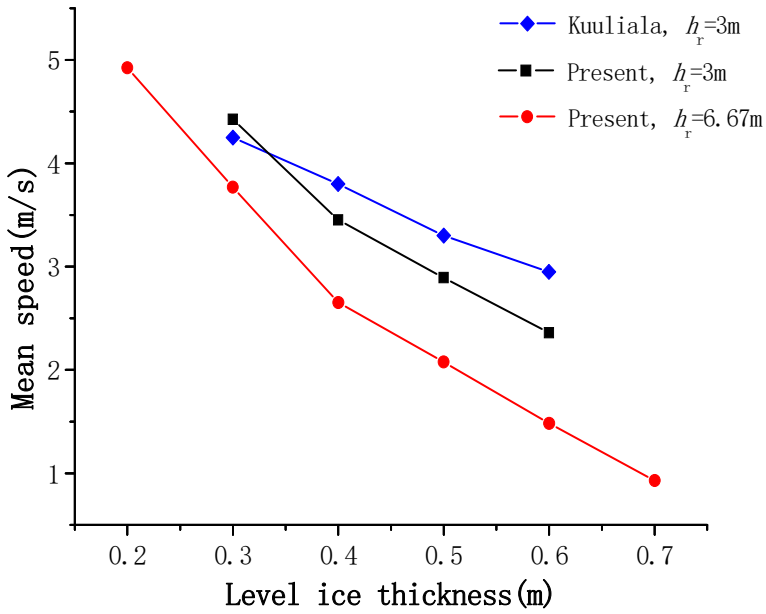

Fig. 4.19 Simulated mean speeds in various ice thicknesses by constant thrust.

4.3.2 Local ice-induced loads and statistical analysis

4.3.2.1 Local ice-induced loads

The same location of frame at the bow shoulder area is selected to calculate the local ice loads, as presented in Fig. 3.23. Fig. 4.20 and Fig. 4.21 show the simulated time histories of local ice loads on this frame with the keel distribution in Fig. 4.13 in level ice thickness of 0.2 m and 1.0 m respectively. The maximum numerical load peaks in 1 m ice thickness can reach 1400 KN/m, which is comparable to measurements published in the final report of the ARCDEV project [69]. In this ARCDEV report, a duration of 10 min time history when the ice tanker M/T Uikku went through an ice ridge is recorded during measurement No. 35. The level ice thickness samples consist of four tenths in the interval of 0.3 m–0.7 m, five tenths in the interval of 0.7 m–1.2 m, and one-tenth in the interval greater than 1.2 m. The ridge depth distribution is one-half in the range of 1.0 m–1.5 m and another half in the range of 1.5 m–2.0 m. The scale of M/T Uikku is close to the numerical ship model, of which the length between perpendiculars is as long as 150 m. The maximum signal value from bow shoulder area is up to 1000 KN/m.

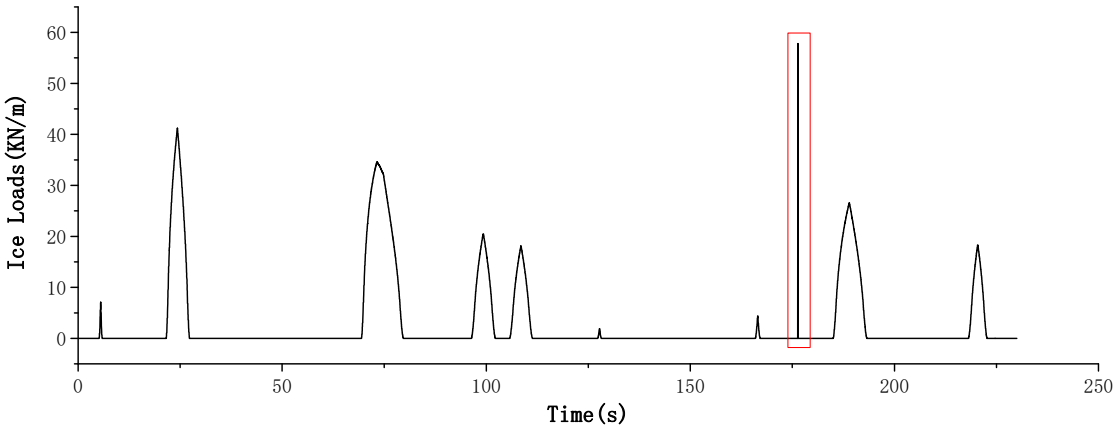

Fig. 4.20 Simulated time histories of local ice loads in level ice thickness of 0.2 m.

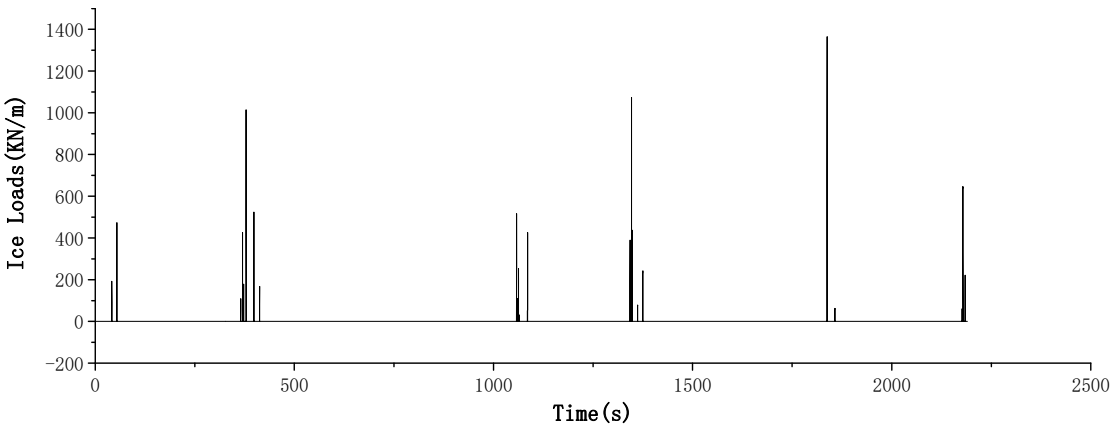

Fig. 4.21 Simulated time histories of local ice loads in level ice thickness of 1.0 m.

From Fig. 4.20 and Fig. 4.21, it is apparent that in the case of 0.2 m ice thickness, contacts between the frame and ice edge of level ice or consolidated layer rarely occur. The only occurrence is emphasized in the box. Compared to that, the impulse caused by the keel loads lasts for a longer duration required for a ship to pass through the present ridge. Load values of these two kinds are in the same level. However, for 1.0 m ice thickness, the frame loads caused by displacing keel blocks are much smaller than those because of the breaking level ice and the consolidated layer. That is true because that 1) the frame spacing is only 0.35 m in the simulations, less than one percent of the ship bow length, and ridge keels are treated as homogeneous and isotropic. Therefore, the frame keel loads account for a very small share of the global keel load. 2) ship–level ice or ship–consolidated layer interaction happens at local contact zones as presented in Fig. 3.3. Therefore, if contact occurs on the specified frame, it will cause a high local load. Consequently, even though both the keel loads and level/consolidation loads contribute greatly to global ice loads, the keel effect is not important for local frame loads. It can be ignored in high level ice thickness. In ARCDEV research, instantaneous impulses rising from the nearly zero value are dominant, which means that the local loads induced by keels are quite small and nearly negligible.

4.3.2.2 Statistical analysis

The 50 numerical simulations of ice-induced frame load processes for each ice condition deal with Rayleigh separation, and then the peak loads are described using a Weibull model, as introduced in Chapter 3. Fig. 4.22 shows that the ice load peaks on a specified frame in different level ice thickness are presented in the Weibull distribution. With the high ice thickness of 1 m, peak values are observed to form nearly a straight line, which means that the ice load peaks of the numerical simulation fit the Weibull distribution well, whereas in the low ice thickness of 0.2 m, some deviations from the straight line occur in upper tail because in this case the loads attributable to the level ice section are low and the ridge keel effect might be more readily apparent, but it is still acceptable to model it using a Weibull distribution.

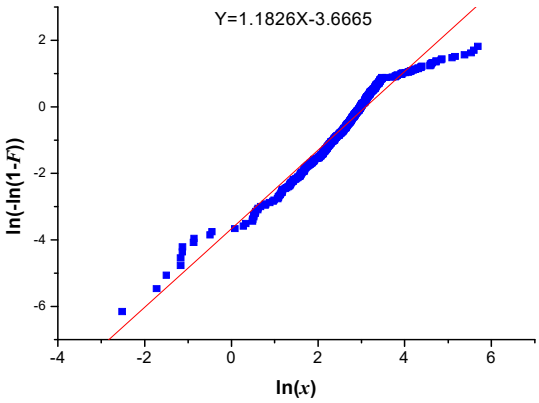

$h_i = 0.2$ m

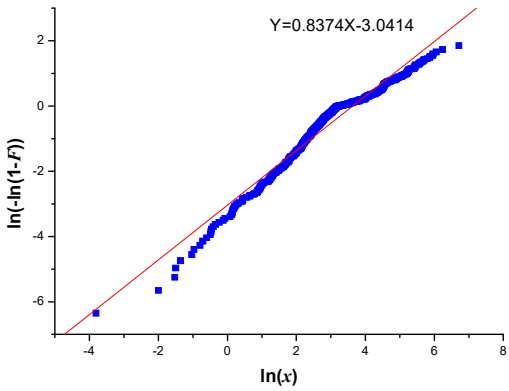

$h_i = 0.3$ m

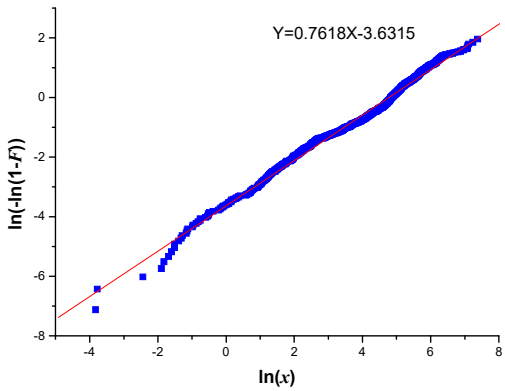

$h_i = 0.4$ m

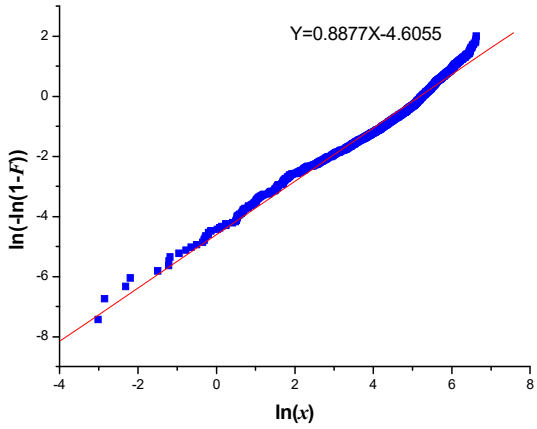

$h_i = 0.5$ m

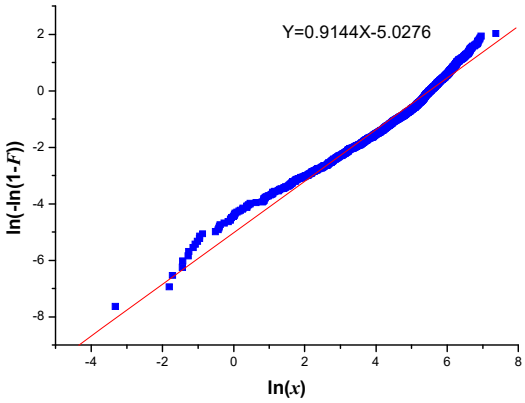

$h_i = 0.6$ m

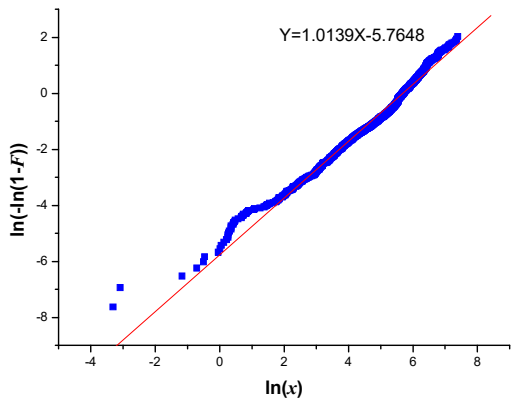

$h_i = 0.7$ m

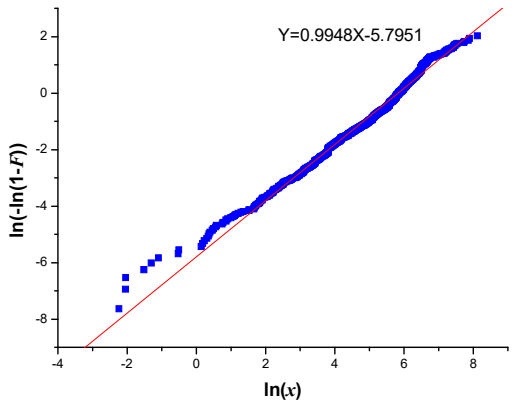

$h_i = 0.8$ m

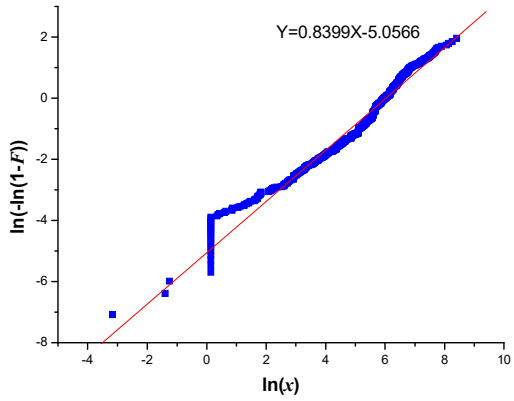

$h_i = 0.9$ m

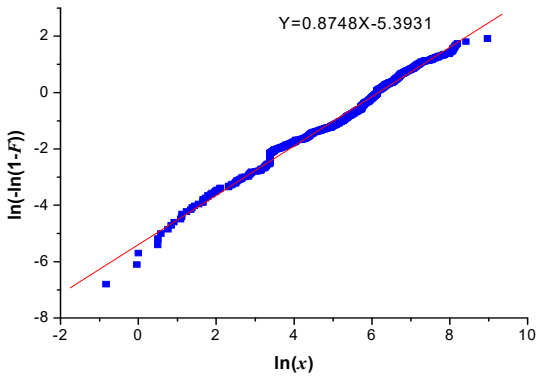

$h_i = 1.0$ m

Fig. 4.22 The calculated load peak distribution in ridged ice fields and fitted line of Weibull distribution in the level ice thickness from 0.2 m to 1.0 m.

The statistical distribution parameters of numerical load peaks are shown in Table 4.1 in different ice conditions. Considering the different ship models used in the field measurements and numerical simulations, the shape parameter values of the simulated peaks are located in a reasonable range 0.7618 <k < 1.1826, compared to statistical analysis of field measurement data $0.7 < k < 1.0$ [55].

Table 4.1 Distribution parameters of the Weibull model for load peaks of various ice thicknesses in ridged ice fields

h_i	Shape parameter k	Scale parameter ε
0.2 m	1.1826	22.2031
0.3 m	0.8374	37.7919
0.4 m	0.7618	117.6024
0.5 m	0.8877	179.1001
0.6 m	0.9144	244.3113
0.7 m	1.0139	294.7143
0.8 m	0.9948	338.8530
0.9 m	0.8399	411.8340
1.0 m	0.8748	475.7856

4.4 Summary

A numerical model is developed to calculate both global and local ice loads in ridged ice fields, in which a semi-empirical method is introduced to develop a numerical model of ship–ice interaction in level ice and the consolidated layer in ice ridges. A modified Rankine's plasticity model is applied to calculate ice loads caused by ridge keels, considering effects of ship movement and inertia force of ice accumulation in front of the ship bow. Multiple simulations of ship transiting ridged ice in different ice conditions are conducted under randomly generated ridge-field profiles. Ship performance can be well reproduced using the numerical method. Computed results confirm that ice ridges can engender high loads levels, causing the ship speed to slow dramatically when sometimes rams might have to be required. Although the ridge keel factor contributes much to global ice loads, the keel effect is not great for local frame loads: in fact, it is negligible in cases of high level ice thickness. The simulated global and local ice-induced loads compare well with published results of model tests and field measurements in ridged ice fields. The local load peaks can be modeled as a Weibull distribution, although some deviations exist in cases of low ice thickness. The shape parameters of the Weibull model representing numerical ice loads process agree well with statistical results of field measurement data. This agreement makes it possible to apply the model for practical use for route planning in ice or for evaluating a ship's operability and structural safety in given ice conditions.

Chapter 5

Numerical Model of Ship Operating in Pack Ice Fields

In managed ice fields and marginal ice zones, a continuous ice sheet has been broken into smaller ice floes by icebreakers or wave actions. These types of ice cover are discontinuous in nature and can be idealized as a composition of distinct ice pieces. In broken ice fields, occasional ship–ice collisions may occur, rather than continuous icebreaking process in level ice. In this chapter, a 2D DEM numerical model is developed for simulating the interaction between drifting ice floes and a moving ship. The ice floes are represented as hundreds of circular disks with random sizes and positions. Both the ship–ice collisions and ice–ice contacts are modeled, and a viscous-elastic rheology is applied at contacts. The ice loads in different ice conditions (ice thickness and ice concentration) can be determined from a series of simulations. The numerical results are compared with published simulated results in pack ice fields.

5.1 Ship–ice interaction mechanics in pack ice fields

5.1.1 Contact detection

Since a large number of ice floes are incorporated in a calculation domain, the DEM model requires an efficient computer algorithm to detect the ice–ice contacts and ship–ice contacts, which is done by using a cell structure to identify neighboring disks. The cells are squares with their edges parallel to the global x and y coordinates, as shown in Fig. 5.1. The dimensions of the cell domain should slightly exceed those of the ice domain to enable inclusions of disks located on the boundary.

In order to ensure that each cell contain only a few disks, the dimension of a cell should be larger than that of disks. Consequently, the side length of cells a and maximum disk radius $R_{\max}$ in the ensemble are chosen to satisfy a ratio as

$$\frac{a}{2R_{\max}} > 1 \tag{5.1}$$

In most cases, it is beneficial to choose the ratio slightly above 1.

The location of the current disk with center coordinates (x_i, y_i) is computed in two steps. First the integer cell numbers in the x and y directions are computed by

$$I_x = NCELL_x \bullet \mathrm{int}[(x_i - x_{\min}) / (x_{\max} - x_{\min})] + 1 \tag{5.2}$$

$$I_y = NCELL_y \bullet \mathrm{int}[(y_i - y_{\min}) / (y_{\max} - y_{\min})] + 1 \tag{5.3}$$

where $x_{\min}$ and $x_{\max}$ are the coordinates of extreme points of the cell domain on the x axis, $NCELL_x$ represents the number of cells in the x direction. The definitions of terms in y direction are analogous.

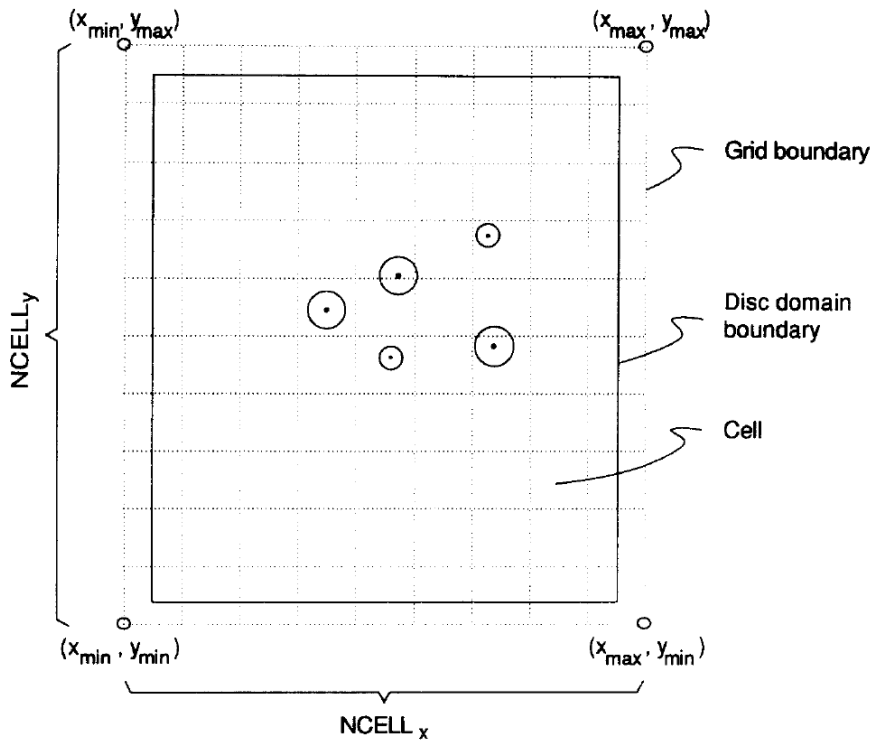

Fig. 5.1 Cell structures in a computation domain [70].

The cell number of the current disk, *ICELL*, can be calculated as follows.

$$ICELL = (I_y - 1) \bullet NCELL_x + I_x \tag{5.4}$$

The cell number of disk i is stored in an array CELLNO (i) and the disk number, i, is stored in the two-dimensional array DISCNO (*ICELL*, j), where j is the first vacant element of the actual row *ICELL*. The number of occupied elements in one row corresponds to the number of disks in the same cell.

Ice–ice contacts are primarily defined by the distance between two disks. A solid contact can be logged when overlapping between ice floes occurs, as presented in Fig. 5.2. The ship waterline is represented as a polygon, including nodes and line segments. In the simulation, each segment has to be checked for contact with the disks. A case of

collision between ship segments and ice floes is illustrated in Fig 5.3.

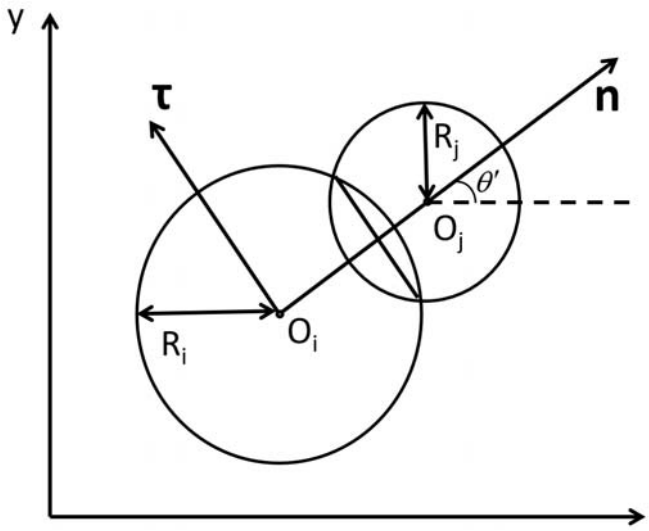

Fig. 5.2 Collision between two circular ice floes.

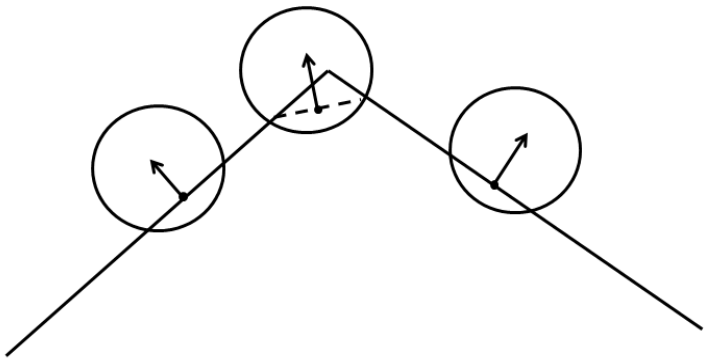

Fig. 5.3 Collision between ship and ice floe.

With the cell structures, it is sufficient to scan only eight adjacent cells and the same cell to the current cell of a disk or hull segments when identifying possible ice–ice contacts and ship–ice contacts. The computation time can be significantly saved.

5.1.2 Contact force

5.1.2.1 Ice–ice contact

The contact force is simple to analyze. Ice floes are modelled as soft particles with finite stiffness in this method. A local coordinate system, $n-\tau$, which is associated along with each collision incident, is introduced, as portrayed in Fig. 5.2. n denotes the normal direction and τ represents the tangential direction. The ice motion information would be transformed into the $n-\tau$ reference frame. When the elements are interacting with each other, it is supposed that there are two components of contact force on the contact zone, i.e. the normal force and the tangential force. The $n-\tau$ coordinate system with the origin O_i is defined as below.

$$\vec{n} = \frac{\overrightarrow{O_iO_j}}{\left|O_iO_j\right|} = (\cos\theta', \sin\theta') \tag{5.5}$$

$$\vec{\tau} = (-\sin\theta', \cos\theta') \tag{5.6}$$

where O_i and O_j are the centers of the two contact disks, $\vec{n}$ and $\vec{\tau}$ are the unit vectors of the normal axis and tangential axis respectively, θ' is the angle from x-axis to the vector $\vec{n}$.

The relative velocity at the point of contact is given by

$$\dot{\overrightarrow{O_iO_j}} = \dot{O}_i - \dot{O}_j + (R_i\omega_i + R_j\omega_j)\vec{t} \tag{5.7}$$

In that equation, $\dot{O}_i$ and $\dot{O}_j$ stand for the linear velocity for the two disks, ω_i and ω_j are the angular velocities, R_i and R_j signify the radius of disks i and j, respectively. The relative displacement rate in normal and tangential directions can be obtained by projecting the relative velocity onto the n−t unit axial vectors.

The normal force is represented as a sum of elastic and damping terms. These two components have a direction opposite to the penetration. Consequently,

$$F_{\mathrm{n}}^{i} = -K_{ne}\delta_{\mathrm{n}}^{i} - K_{nv}\dot{\delta}_{\mathrm{n}}^{i} \tag{5.8}$$

Therein, the superscript i denotes the current time step, K_{ne} represents the normal contact stiffness, K_{nv} stands for the normal contact viscosity, $\dot{\delta}_n^i$ signifies the relative velocity of the two disks at normal direction, δ_n^i is the normal indentation of overlap, which can be determined as

$$\delta_n^i = R_i + R_j - \Delta_{ij} \tag{5.9}$$

where Δ_{ij} is the distance between the two disk centers.

The tangential force is treated as linear-elastic, i.e. the incremental change in the tangential force due to friction is proportional to the relative tangential velocity.

$$F_{\tau}^{i*} = F_{\tau}^{i-1} - K_{\mathrm{te}}\dot{\delta}_{\mathrm{t}}^{i}\delta t \tag{5.10}$$

where the superscript i-1 denotes the previous time step, K_{te} stands for the tangential contact stiffness, $\dot{\delta}_t^i$ represents the relative velocity of the two disks at tangential direction.

Nevertheless, based on the Coulomb friction law, the Coulomb friction limit is the upper limit of the tangential force, and thus the tangential force can be expressed as

$$F_{\tau}^{i} = \min(F_{\tau}^{i*}, \mathrm{sign}(F_{\tau}^{i*})\mu_i F_{\mathrm{n}}^{i}) \tag{5.11}$$

5.1.2.2 Ship–ice contact

For ship-ice collision, the calculation method of the contact force is similar to that of ice-ice collision. In this study, referring to Feng and Owen [71], the middle point of the contact line is identified as the reference contact point where the normal force should be applied, and the contact normal direction is defined as perpendicular to the line that passes through the two intersecting points between the ship waterline and ice floe, by which no directional jump occurs at the corner when the ice floe continuously moves from the left position to the right, as shown in Fig. 5.3. The total contact forces acting on ship hull and each ice floe are calculated as a sum of contact force induced by all the ship–ice collisions and ice–ice collisions.

5.1.3 Motion of ice floes

In Chapter 2, we addressed the solution of ship motions using a step-by-step integration method. In the cases of pack ice fields, ice floes could be driven to move by ship advancing and current forces. It is assumed that the disks do not rotate, and there is no layering. The disks only move translationally in horizontal plane. In each time step, the motion of each ice floe needs to be solved. The motions of ice floes follow the Newton's second law, and can be solved by the assumption of linear acceleration as well.

When an ice floe moves with an acceleration, its inertia force increases significantly and can be achieved with the additional mass method. The additional mass M_a is given by [28]

$$M_a = C_m \rho_w V_{\text{sub}} \frac{d(|\boldsymbol{V}_i - \boldsymbol{V}_w|)}{dt} \tag{5.12}$$

where C_m is the additional mass coefficient, V_{sub} represents the submerged area of the floe, $\boldsymbol{V}_i$ and $\boldsymbol{V}_w$ are the velocity vectors of ice floe and water respectively.

Owing to the effect of current, sea ice is subjected to the water drag force, which can be expressed as [72]

$$F_d = \frac{1}{2} C_d \rho_w A_f (v_w - v_i) |v_w - v_i| \tag{5.13}$$

$$M_d = -\frac{1}{2} C_d' (R)^2 \rho_w A_f \omega |\omega| \tag{5.14}$$

Therein, F_d and M_d are the water drag force and rotational drag moment, C_d denotes the drag coefficient of water, A_f stands for the ice floe area, C_d' represents the rotational drag coefficient, ω signifies the floe rotational velocity.

5.2 Numerical results of ice loads in pack ice fields

5.2.1 Global ice loads and ship performance

A rectangular simulation domain is used to model the pack ice field with a dimension of 600 m×250 m. The radius of ice floes is set to be in the range from 2 m to 10 m randomly, with a specified ice concentration. In this study, ship navigates with a constant thrust. Periodic boundary conditions are adopted, in this case, the disks leaving the ice domain will be reintroduced on the opposite boundary with their momentum unchanged, so as to ensure the ice concentration in the simulation domain to be constant. Some computational parameters about ice floe properties are presented in Table 5.1.

Table 5.1 Ice floe properties

Normal contact stiffness K_{ne}	587 KN/m
Tangential contact stiffness K_{te}	352 KN/m
Normal contact viscosity K_{nv}	5.87 KN·s/m
Added mass coefficient C_m	0.15
Normal drag coefficient C_d^n	0.6
Tangential drag coefficient C_d^τ	0.06
Rotational drag coefficient C_d'	0.6

Fig. 5.4 shows the ship runs into the ice field with ice concentration of 60% from the left side, and travels out from the right side. The navigation route seems nearly an inclined straight line, although the initial speed of ship is parallel to the x axis. This is due to the asymmetric distribution of ice floes on the starboard side and larboard side of ship model, which causes asymmetric forces on these two sides.

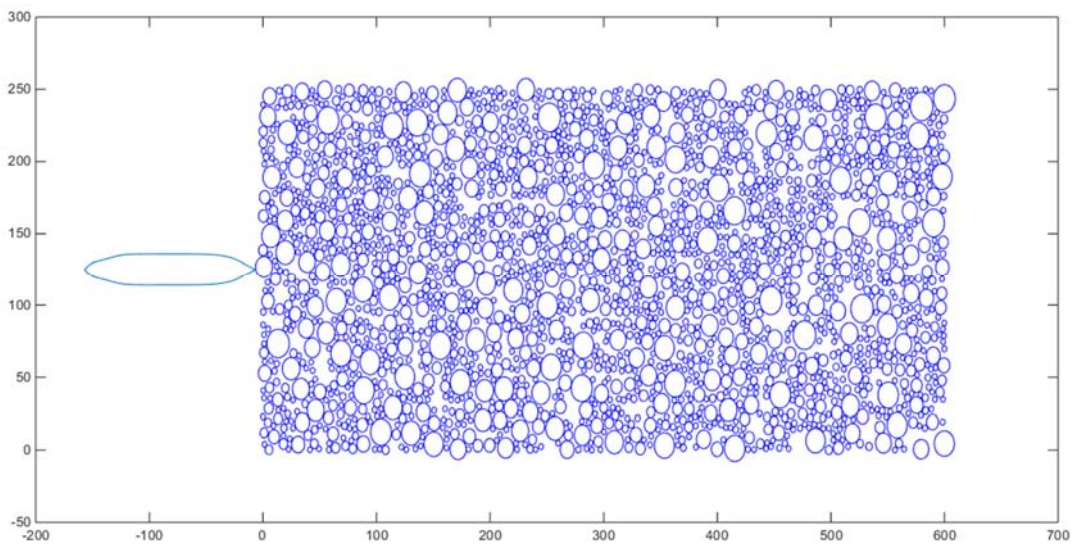

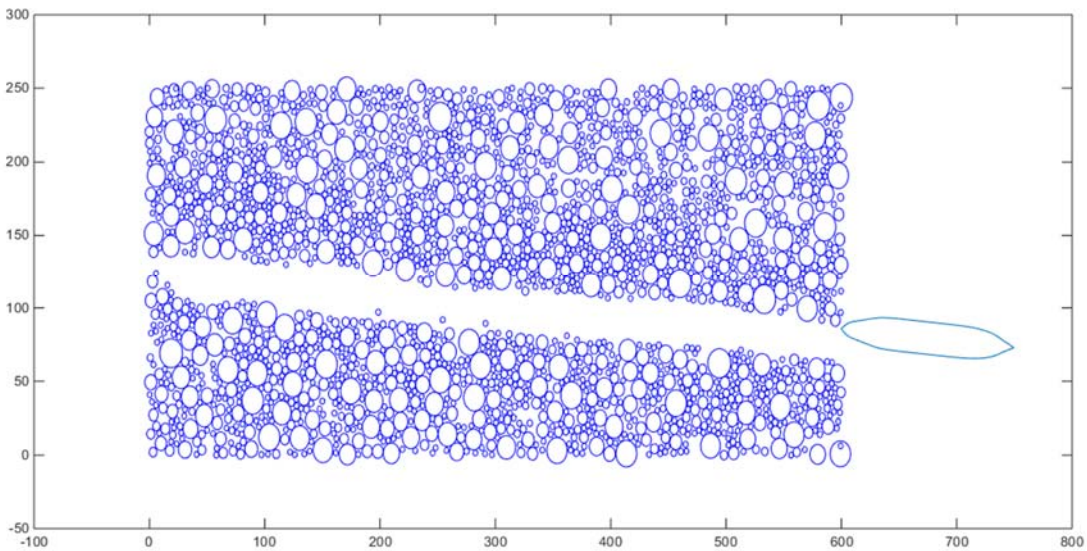

Fig. 5.4 Ship navigation process through ice floes domain.

In order to verify the simulation procedure, two comparisons are made between the present numerical results and the earlier studies conducted by Ji et al. [28] and Daley et al. [30]. Ji et al. [28] performed the numerical simulation of ship operating with a constant speed of 4.0 m/s in 0.6 m thick ice under ice concentration of 60%. The obtained maximum and mean ice loads are 1479 kN and 440 kN, respectively. Fig. 5.5 presents the time history of ice loads with the same conditions, except the constant thrust. The numerical maximum and mean loads values are 1850 kN and 442 kN, which compare well with Ji's results.

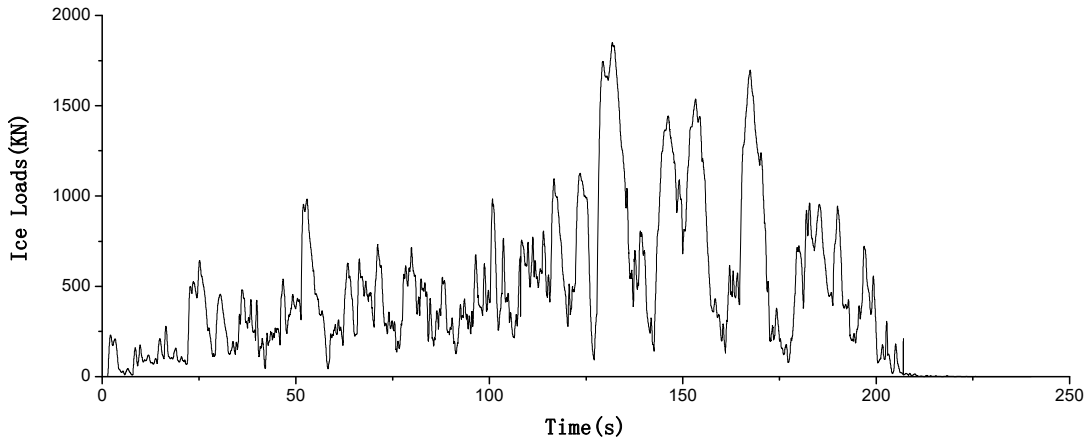

Fig. 5.5 Time history of ice loads calculated by the numerical simulation (Ice thickness = 0.6 m, Ice concentration = 60%).

Daley et al. [30] adopted the GEM simulation approach to calculate the ice loads by a constant thrust in a series of various ice conditions. The numerical results in an individual run performed under 0.5 m thick ice and 40% ice coverage can be found in the list of result values. The maximum and mean ice loads are 1152 kN and 78 kN respectively. The calculated ice loads by the present numerical model are shown in Fig. 5.6. The simulated maximum and mean values are 1303 kN and 279 kN. By comparison,

the maximum values are in the same order of magnitude, whereas, a higher mean value is found in this study.

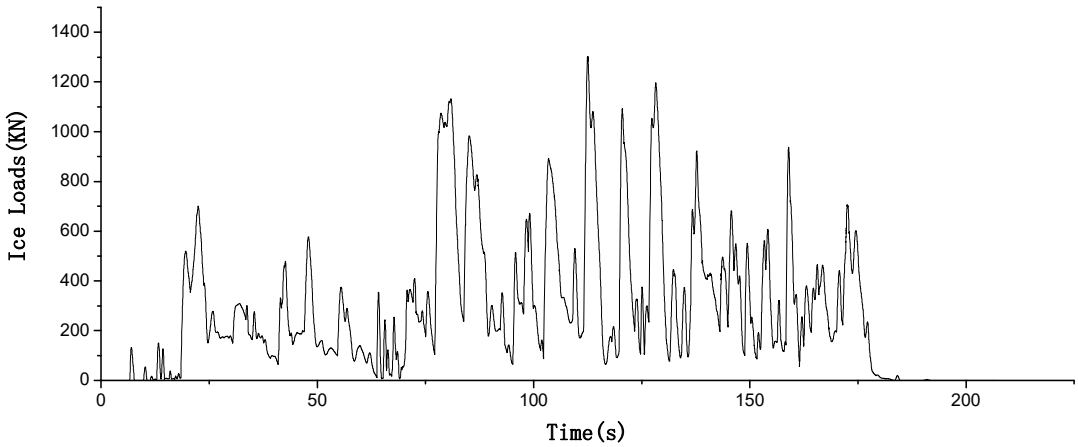

Fig. 5.6 Time history of ice loads calculated by the numerical simulation (Ice thickness = 0.5 m, Ice concentration = 40%).

The simulated speed time series under 0.2 m thick ice and 60% ice coverage is portrayed in Fig. 5.7. It can be observed that as the ship travels into the ice floes region, a nearly steady speed can be achieved, although still with fluctuations. The fluctuations can be attributed to the ice impulse loads.

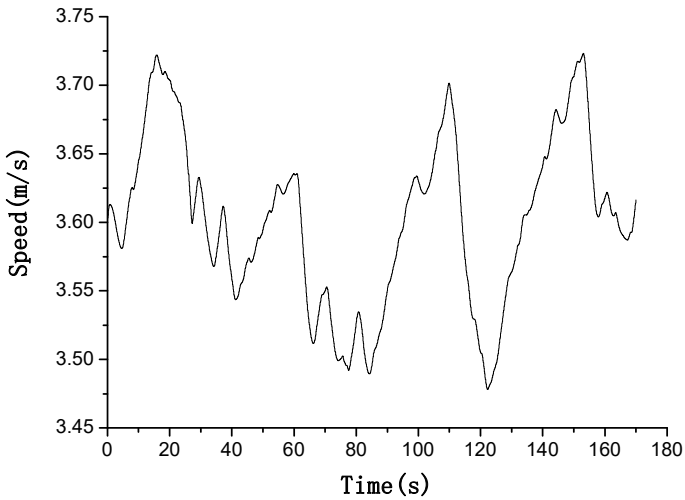

Fig. 5.7 Simulated speed time series (Ice thickness = 0.2 m, Ice concentration = 60%).

Ice thickness, ice concentration and floe size are important parameters affecting the ice loads significantly. The influences of these parameters on ice resistance are analyzed, which are illustrated in Figs. 5.8, 5.9 and 5.10 respectively. The figures show that the ice loads generally increase with the increasing ice thickness, however, some deviations can be observed even under the same ice floe distribution, such as the case in 0.4 m thick ice with 40% ice coverage. This might be because the collisions between ship and ice floes are very sensitive to the ice thickness. Also, the growth rate of ice resistance with the increase of ice thickness is not high. As for the influence of ice concentration, it is clear that ice resistance is greater under higher ice concentration. The different floe

sizes are modeled in the simulations, and the resistance increases with the increasing floe radius. It might be because the inertial force and drag force are greater of larger floes.

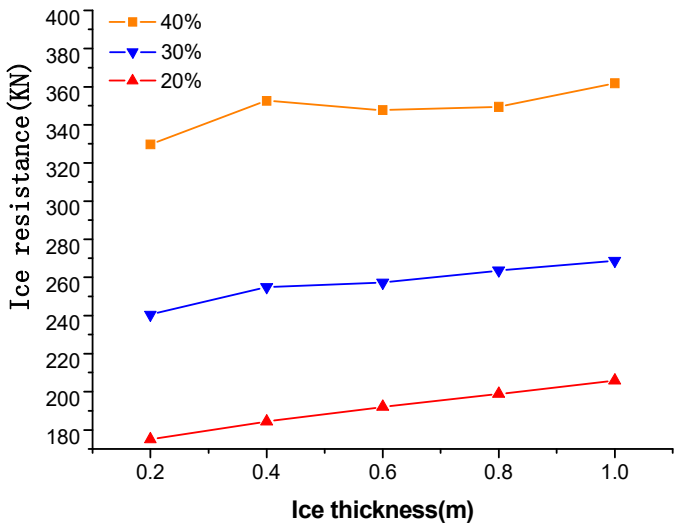

Fig. 5.8 Influence of ice thickness on ice resistance.

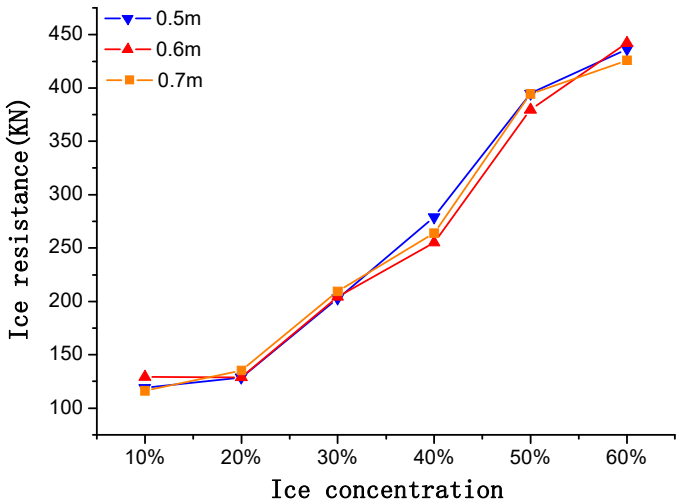

Fig. 5.9 Influence of ice concentration on ice resistance.

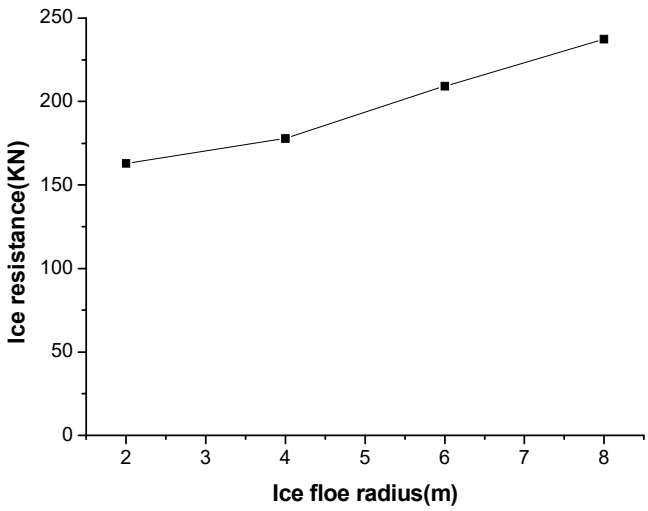

Fig. 5.10 Influence of ice floe size on ice resistance.

5.2.2 Statistical analysis of local ice-induced loads

Considering the random nature of pack ice fields, 10 simulations were performed for each ice condition (ice thickness and ice concentration). After Rayleigh separation, the ice load peaks on a specified frame in different ice conditions are plotted in the Weibull distribution. An example of plotting results of load peaks under 20% ice coverage is shown in Fig. 5.11. The peak values are observed to form nearly a straight line, which means that the ice load peaks of the numerical simulation fit the Weibull distribution well.

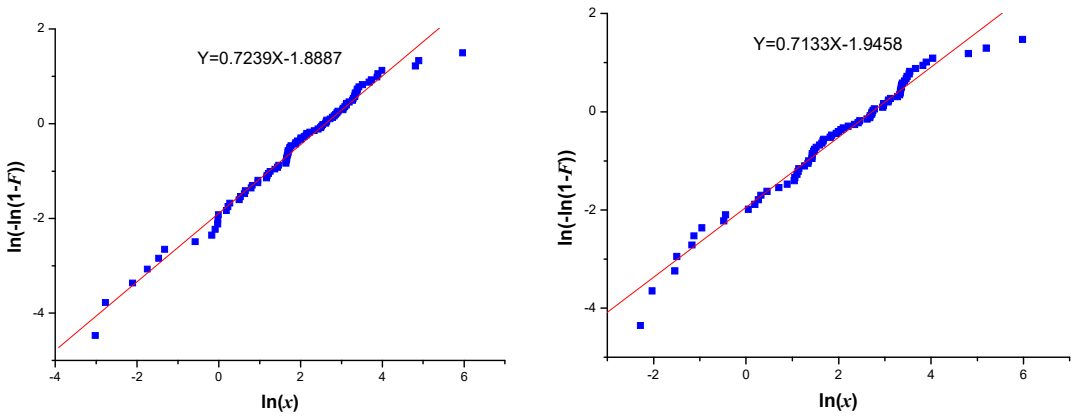

$h_i = 0.2$ m $h_i = 0.3$ m

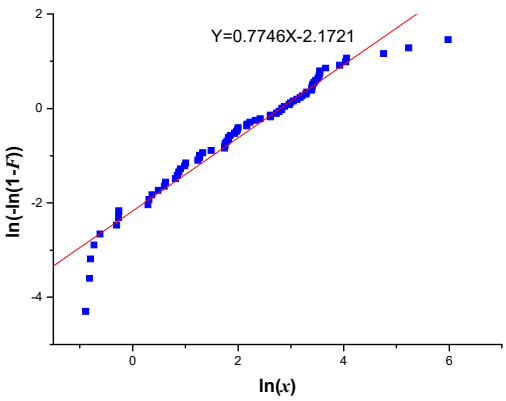

$h_i = 0.4$ m

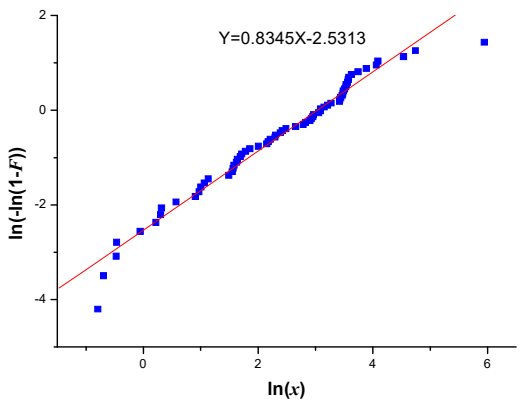

$h_i = 0.5$ m

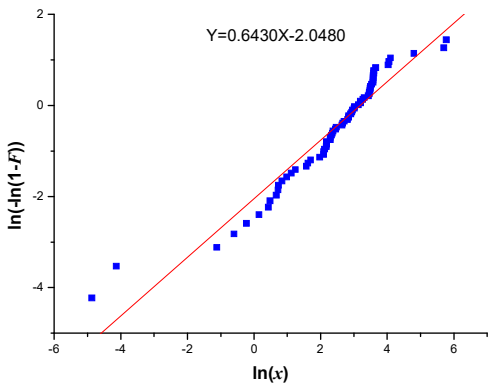

$h_i = 0.6$ m

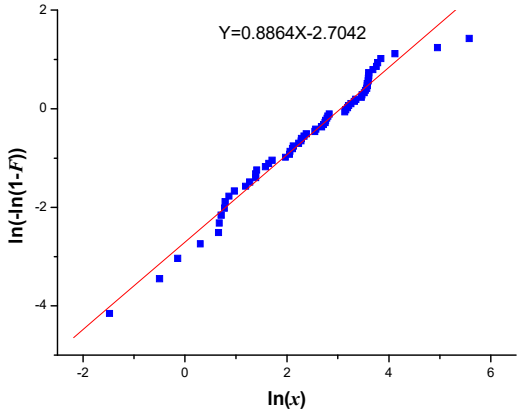

$h_i = 0.7$ m

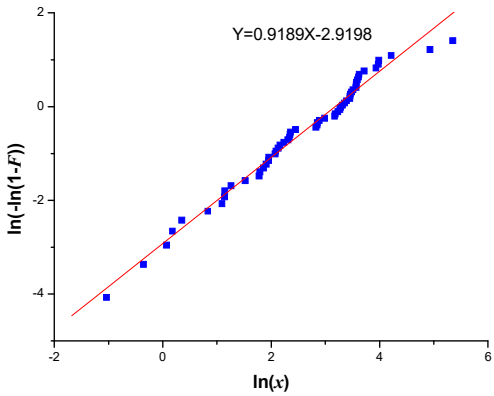

$h_i = 0.8$ m

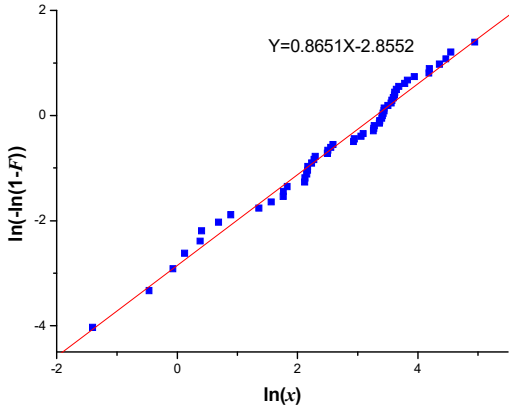

$h_i = 0.9$ m

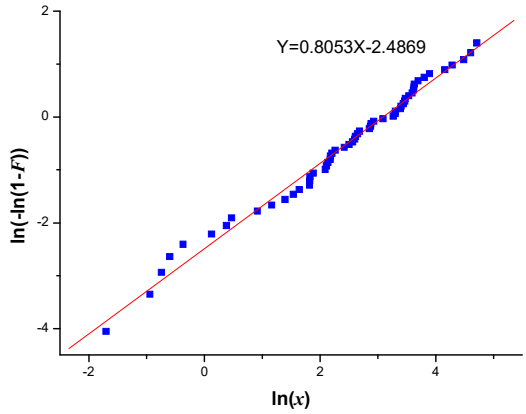

h_i = 1.0 m

Fig. 5.11 The calculated load peak distribution and fitted line of Weibull distribution (Ice concentration = 20%).

The statistical distribution parameters of numerical load peaks are shown in Table 5.2 in different ice conditions. Considering the different ship models used in the field measurements and numerical simulations, the shape parameter values of the simulated peaks are located in a reasonable range, compared to statistical analysis of field measurement data [54], in which the shape parameter of 0.75 is used to fit the ice loads of MS Kemira during the winters 1987 and 1988 in different ice conditions, including level ice and deformed ice.

Table 5.2 Distribution parameters of the Weibull model for load peaks of various ice thicknesses and concentration

(1) 10% ice coverage

h_i	Shape parameter k	Scale parameter θ
0.2 m	0.7918	9.4452
0.3 m	0.7984	9.8150
0.4 m	0.9991	11.5578
0.5 m	0.7340	13.7408
0.6 m	0.8141	15.1213
0.7 m	0.8754	17.6305
0.8 m	0.7748	19.2877
0.9 m	0.5333	21.4010
1.0 m	0.8261	23.7457

(2) 20% ice coverage

h_i	Shape parameter k	Scale parameter θ
0.2 m	0.7239	13.5872
0.3 m	0.7133	15.3001
0.4 m	0.7746	16.5144
0.5 m	0.8345	20.7616
0.6 m	0.6430	24.1658
0.7 m	0.8864	21.1347
0.8 m	0.9189	23.9889
0.9 m	0.8651	27.1232
1.0 m	0.8053	21.9414

(3) 30% ice coverage

h_i	Shape parameter k	Scale parameter θ
0.2 m	0.9815	20.2858
0.3 m	0.9053	20.4412
0.4 m	0.9506	22.5106
0.5 m	0.9460	22.4789
0.6 m	0.8711	22.0377
0.7 m	0.7841	25.7816
0.8 m	0.8485	28.8845
0.9 m	0.9741	31.0879
1.0 m	0.9195	31.2612

(4) 40% ice coverage

h_i	Shape parameter k	Scale parameter θ
0.2 m	0.8768	27.4936
0.3 m	0.8378	29.3960
0.4 m	0.9344	36.6771
0.5 m	0.8676	36.4964
0.6 m	0.8553	33.6466
0.7 m	0.8767	34.9945
0.8 m	0.7868	33.0608
0.9 m	0.9586	36.2195
1.0 m	0.8431	38.2988

(5) 50% ice coverage

h_i	Shape parameter k	Scale parameter θ
0.2 m	0.8069	46.5420
0.3 m	0.8251	43.9443
0.4 m	0.8186	41.8472
0.5 m	0.9002	41.5944
0.6 m	0.8496	40.1006
0.7 m	0.8437	39.2490
0.8 m	0.8924	39.3633
0.9 m	0.8663	47.4892
1.0 m	0.8566	41.8823

(6) 60% ice coverage

h_i	Shape parameter k	Scale parameter θ
0.2 m	0.7706	71.1344
0.3 m	0.7518	75.2874
0.4 m	0.8467	61.4169
0.5 m	0.7818	68.8881
0.6 m	0.7283	66.5824
0.7 m	0.8859	56.9650
0.8 m	0.7959	55.3336
0.9 m	0.8755	60.5783
1.0 m	0.8402	55.2167

5.3 Summary

A 2D DEM numerical model is developed for simulating the interaction between drifting ice floes and a moving ship. The ice floes are represented as hundreds of circular disks with random sizes and positions. The navigation process through pack ice can be well reproduced by this procedure. The numerical results are comparable to those simulated in earlier studies. Ship speed remains relatively steady during the transiting process. In general, ice resistance increases with the increasing ice thickness and concentration. The local frame loads can be modeled according to the Weibull distribution, and the shape parameters are consistent with those obtained based on field measurements.

Chapter 6

Fatigue Damage Calculation

Ice-going ships are operating under cyclic impact loads caused by the ice in the process of navigating through ice-covered waters. Micro-cracks due to repeated ice loads may lead to a fatigue failure, which can pose a threat to structural safety and contaminant to the environment. Therefore, fatigue assessment of ship hull attributable to ice action is essentially required. A ship can be expected to travel in widely diverse conditions of ice. Ice loads of different ice conditions can be ascertained from a series of numerical simulations as discussed in previous chapters. The structural fatigue stress is found using structural beam theory. A Weibull statistical model is applied to represent the ice-induced stress process. According to ice condition distribution (ice thickness, ice concentration, ridge properties, etc.) and a proper S-N curve, fatigue damage can be estimated based on the Palmgren–Miner cumulative damage rule. An example of fatigue damage calculation is presented. The calculated fatigue damage results are compared with that by field measurements.

6.1 Fatigue damage calculation

Since a ship might encounter a range of different stationary conditions, the total fatigue damage D can be estimated by accumulating a number of fatigue damage contributions D_j in each stationary condition. A systematic procedure for fatigue damage assessment in relation to a local specified transverse frame extending between two decks would be outlined in the following sub-sections. The nominal stress in base metal of ordinary steel is used in the fatigue analysis based on modified Miner's rule. The flow chart of fatigue damage calculation is presented in Fig. 6.1.

6.1.1 Structural response

As discussed in the previous chapters, the ice loads resemble an impulse in level ice, ridged ice and pack ice. Thus, the stress amplitude is a vital parameter for fatigue damage due to ice actions, rather than stress cycles in the fatigue analysis due to wave actions. According to Finnish Maritime Administration [73], a beam model can be employed to evaluate the applied stress for the transverse frame due to an ice-induced load. The conversion from the load into the stress is a linear transformation, which can

be written as follows.

$$S = \frac{P_{\text{ice}} s l_f}{m_{\text{t}} Z} \times 10^3 \tag{6.1}$$

where P_{ice} represents the ice load [kN/m], s expresses the frame spacing, l_f is the frame span, and Z is the section modulus.

$$m_{\text{t}} = \frac{7 m_0}{7 - 5 h_l / l} \tag{6.2}$$

Therein, h_l denotes the height of the load area [m], m_0 incorporates boundary conditions. Values of m_0 are in Table 6.1. In this study, the value of 5.0 is selected, because transverse frames extending between two decks are taken as the target for fatigue calculation.

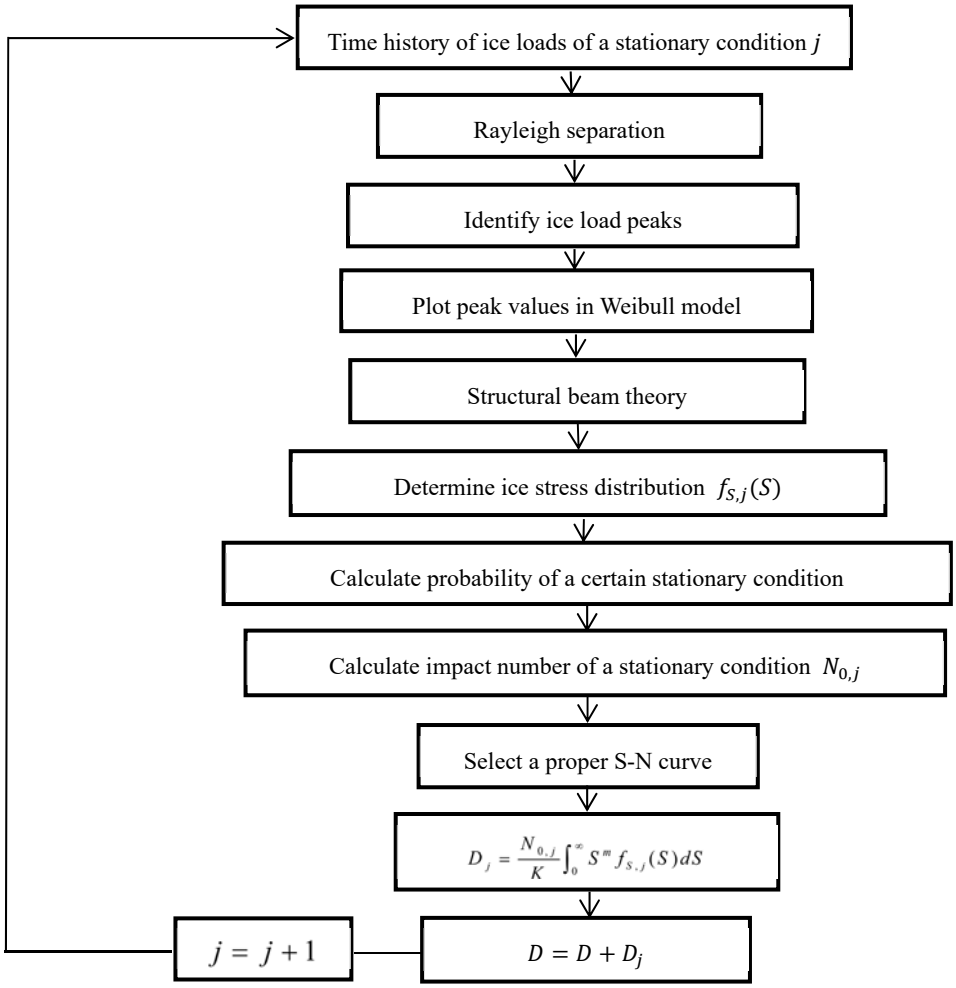

Fig. 6.1 Flow chart of fatigue damage calculation.

With regard to the load height, its calculation is dependent on ice types. For the stationary cases in level ice and pack ice, ship hull is in contact with the sea ice of constant thickness, and the load height is assumed to be the ice thickness for

simplification, whereas for the cases in ridged ice, ice thickness might be varied along the specified local frame, and thus the load height is calculated as the total contact area on a frame divided by the load length.

As presented in the previous chapters, the simulated ice-induced loads process can be modeled according to Weibull distribution. From the linear transformation between loads and stress, we infer that the ice-induced stress also follows the Weibull distribution. In fact, Suyuthi et al. [37] performed a probability plot for the ice-induced stress data obtained from full scale measurement, and it also seems that the Weibull distribution is still valid for representation of the ice-induced stress amplitudes.

Table 6.1 Boundary conditions of the structural beam [73]

Boundary Condition	m_0	Example
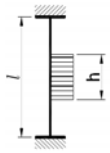	7.0	Frames in a bulk carrier with top wing tanks
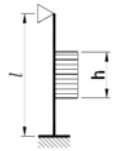	6.0	Frames extending from the tank top to a single deck
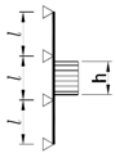	5.7	Continuous frames between several decks or stringers
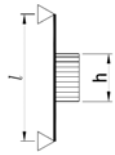	5.0	Frames extending between two decks only

6.1.2 Impact frequency

For each stationary traveling condition, the impact frequency usually varies from one realization to another. An approximate theoretical formulation can be applied, which provides an upper limit for the stress amplitude frequency based on the size of broken ice floe.

Bridges et al. [74] presented that the impact frequency to the hull structure per unit traveling distance is related to the equivalent ice thickness. It is assumed that the length of floe broken in bending is dependent on the ship speed, as shown by Varsta [51] and this is utilized to develop a formula for determining the frequency that reflects the ice

conditions.

$$\upsilon_d = \frac{1852}{10.4h_{eq}^{3/4} - 0.16v_{ow}(h_{eq} / h_L - 1)} \tag{6.3}$$

where υ_d stands for the number of events per nautical mile, h_{eq} represents the equivalent ice thickness, h_L is the ice thickness limit.

Suyuthi et al. [37] derived the frequency of impact per unit distance based on the inverse of the characteristic length of the ice plate, which is presented in Eq. (3.31). Assuming a 100 % concentration of level ice and no effect from relative speed on the broken ice floe length, the impact frequency can be given as

$$\upsilon_d = \frac{1852}{13.3617h_i^{3/4}} \tag{6.4}$$

Therefore, the total number of impacts in level ice can be determined from the impact frequency times sailed distance in ice, based on which the impact number in ridged ice and pack ice can be estimated. As the ship transits into an ice ridge, the keel loads on a frame increase continuously until reaching the maximum keel depth and then decrease gradually. For that reason, the number of ice impacts in ridged ice can be calculated roughly as that in level ice added to that in consolidated layer. The impact number in pack ice can be determined by the calculated number in level ice times the percentage of ice concentration.

6.1.3 Fatigue damage expression

The Palmgren–Miner's linear damage hypothesis is applied for fatigue damage calculation in a particular stationary condition D_j as

$$D_j = \sum_{i=1}^{n_s} \frac{n_i}{N_i} \tag{6.5}$$

where n_i represents the number of stress amplitudes, N_i stands for the number of amplitudes to failure for a constant stress S_i, and n_s is the number of stress magnitudes.

The probability of the stress magnitude S_i can be written in the following two forms:

$$P(S_i) = \frac{n_i}{N_0} = f(S_i)\Delta S \tag{6.6}$$

Therein, N_0 stands for the total number of stress amplitudes in each stationary condition, $f(S)$ represents the PDF of the Weibull distribution of stress amplitudes.

$$f(S) = \frac{q}{r}(\frac{S}{r})^{p-1} \exp\left\{-(\frac{S}{r})^{q}\right\} \tag{6.7}$$

In that equation, q and r are the shape parameter and scale parameter of the Weibull distribution of stress amplitudes.

Consequently, n_i can be given as

$$n_i = N_0 f(S_i)\Delta S \tag{6.8}$$

The relation between S_i, and N_i is an S–N curve expressed as

$$N_i S_i^m = K \tag{6.9}$$

where K and m are constants of S–N curve.

Then, N_i can be expressed as

$$N_i = K S_i^{-m} \tag{6.10}$$

Inserting Eqs. (6.8) and (6.10) into Eq. (6.5), the fatigue damage contribution is obtainable as

$$D_j = \frac{N_0}{K}\int_0^{\infty} S^m f(S) dS \tag{6.11}$$

Inserting Eq. (6.7) into Eq. (6.11), the fatigue damage in a particular stationary condition can be translated as

$$D_j = \frac{N_0}{K} r^m \Gamma(1+\frac{m}{q}) \tag{6.12}$$

where $\Gamma(\bullet)$ is the gamma function.

6.2 Case example

6.2.1 Ice data

In this case example, the contribution of the ice actions to the annual fatigue damage accumulation for a transverse frame of a ship hull is evaluated. The fatigue damage estimation requires knowledge of the ice conditions in the proposed area. Because of thermal and mechanical factors, the ice cover parameters of thickness and concentration vary greatly. The thermal factor is a continuous component and is related to changes in air temperature and snow cover above the ice surface. The mechanical factors are discrete components that are caused by the rafting, ridging, and opening of leads and

polynyas.

Spatial and temporal variation of sea ice thickness has always been of concern. In earlier studies, the ice thickness has been assumed to follow normal, log-normal or gamma distributions. In the present work, presumably, ice thickness follows a normal distribution. The PDF for ice thickness can be expressed as

$$P(h_i) = \int_{h_i-\frac{\delta h}{2}}^{h_i+\frac{\delta h}{2}} \frac{1}{\sqrt{2\pi}\sigma_t} \exp(-\frac{(x-\mu_t)^2}{2\sigma_t^{\,2}})dx \tag{6.13}$$

In that equation, δh equals 0.1 m in the calculation, μ_t denotes the mean value of ice thickness, σ_t is the standard deviation of ice thickness. The mean value and standard deviation are taken as 0.34 m and 0.109 m respectively, referring to Kujala [75].

The existing data of the ice concentration variations are very limited. An information of the mean value and standard deviation of ice concentration in Weddell region can be found in Worby et al. [76], however, the statistical model has not been provided. Numerical simulations in pack ice are conducted in the previous chapter with ice coverage from 10% to 60%. To enable most cases to be located in this range, herein, the distribution of ice concentration is assumed to follow a lognormal distribution. The mean value and standard deviation are respectively set as 38% and 36%. A random variable of ice concentration is denoted as C, which follows a lognormal distribution, then $Y = ln(C)$ follows a normal distribution, i.e. $Y \sim N(\mu_c, \sigma_c)$. The relationship of the mean value and the variance between C and Y can be derived as

$$E(C) = e^{\mu_c+\sigma_c^{\,2}/2} \tag{6.14}$$

$$D(C) = (e^{\sigma_c^{\,2}} - 1)e^{2\mu_c+\sigma_c^{\,2}} \tag{6.15}$$

The logarithmic function is a monotonic one, and therefore the possibility of ice concentration $P(c)$ equals to that of its logarithmic value, which can be determined by integration of the PDF of the normal distribution between $ln(c-\Delta c/2)$ and $ln(c+\Delta c/2)$.

$$P_C(c) = P_Y(ln(c)) = \int_{ln(c-\frac{\Delta c}{2})}^{ln(c+\frac{\Delta c}{2})} \frac{1}{\sqrt{2\pi}\sigma_c} \exp(-\frac{(y-\mu_c)^2}{2\sigma_c^{\,2}})dy \tag{6.16}$$

where Δc equals 10% in the calculation.

6.2.2 Fatigue damage calculation

6.2.2.1 Local ice-induced stress

Ice-induced loads in various ice conditions can be obtained by performing the numerical models presented in the previous chapters. Load peaks on a transverse frame can be transferred into stress amplitudes using structural beam model. In order to evaluate the fatigue damage, it is essential to define the distribution of stress amplitude for each stationary condition, which can be represented with a Weibull model. The

probability plot of ice-induced stress in level ice, ridge ice and pack ice against the Weibull fit are shown in Figs. 6.2, 6.3 and 6.4 respectively.

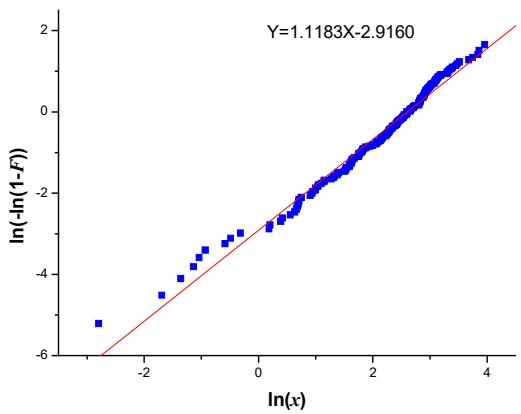

$h_i = 0.2$ m

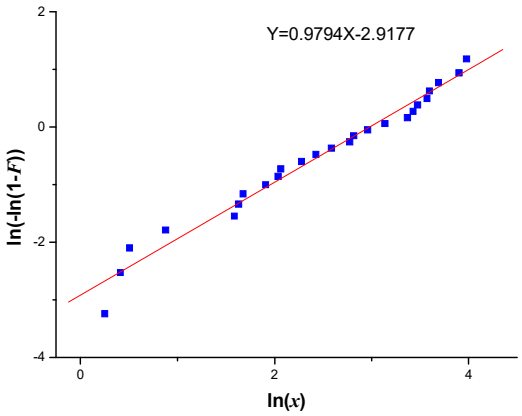

$h_i = 0.3$ m

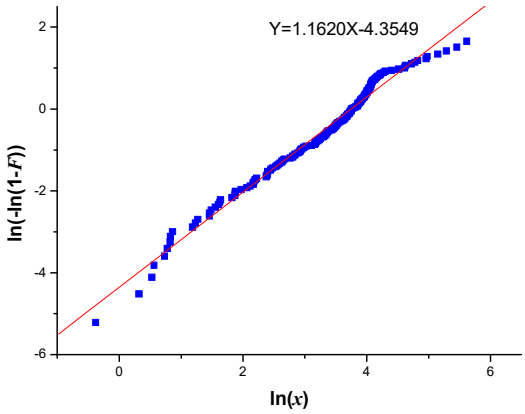

$h_i = 0.4$ m

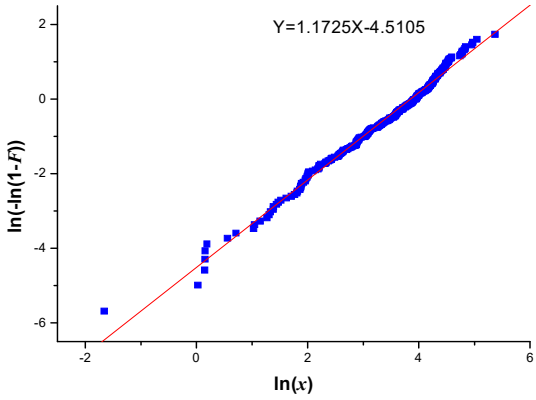

$h_i = 0.5$ m

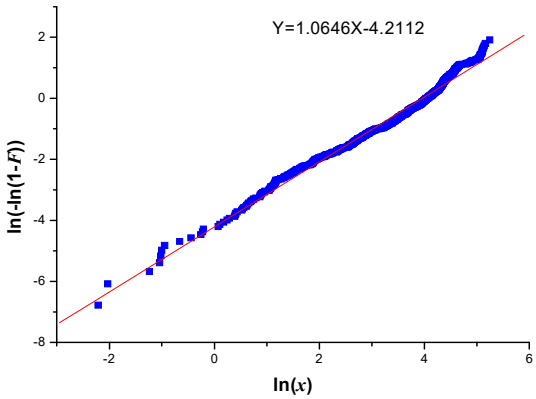

$h_i = 0.6$ m

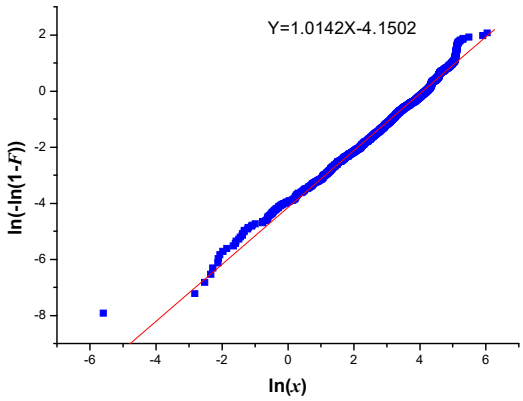

$h_i = 0.7$ m

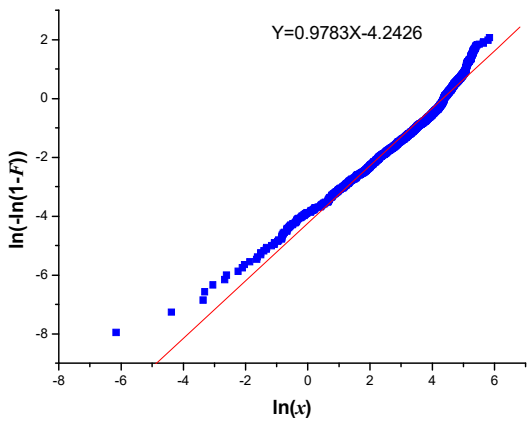

$h_i = 0.8$ m

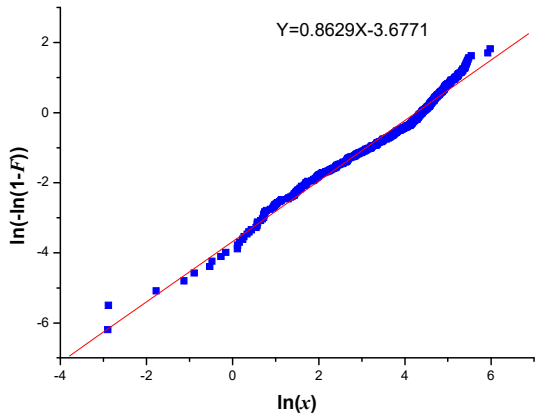

$h_i = 0.9$ m

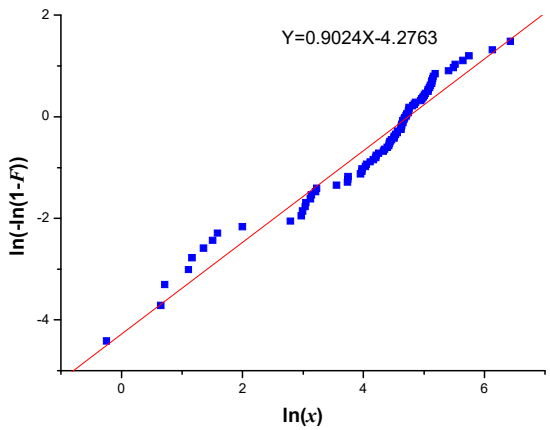

$h_i = 1.0$ m

Fig. 6.2 Probability plot of ice-induced stress in level ice (ice thickness: 0.2 m–1.0 m).

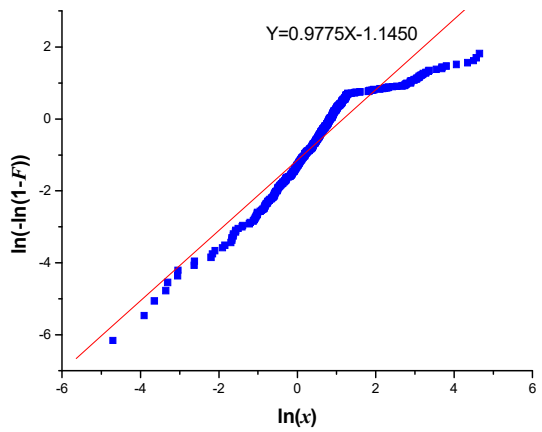

$h_i = 0.2$ m

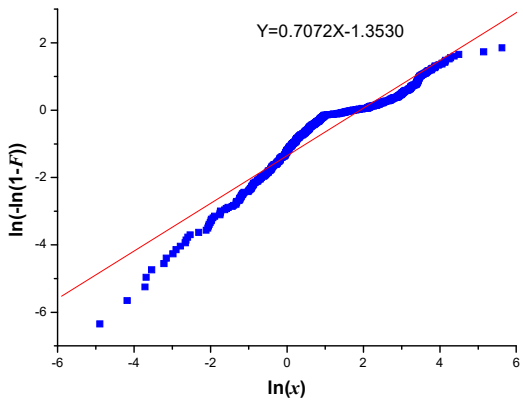

$h_i = 0.3$ m

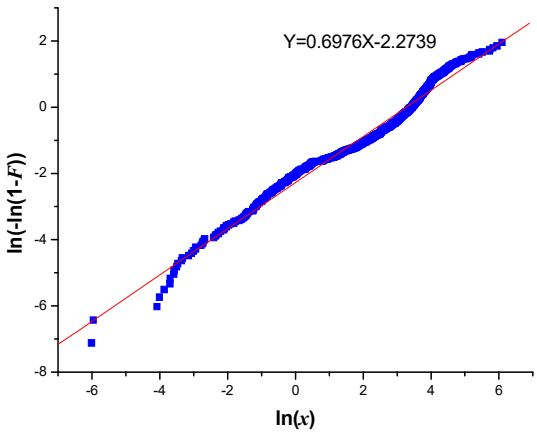

$h_i = 0.4$ m

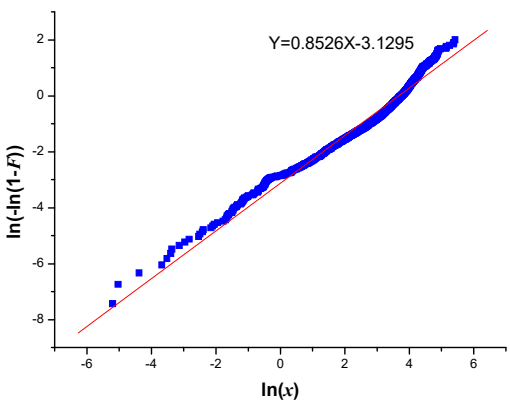

$h_i = 0.5$ m

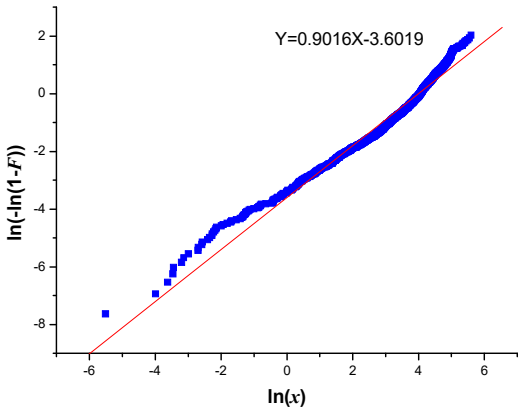

$h_i = 0.6$ m

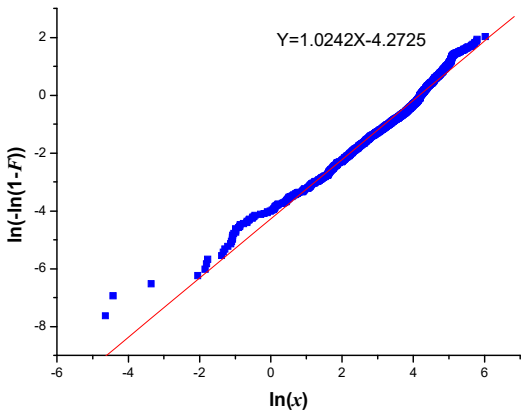

$h_i = 0.7$ m

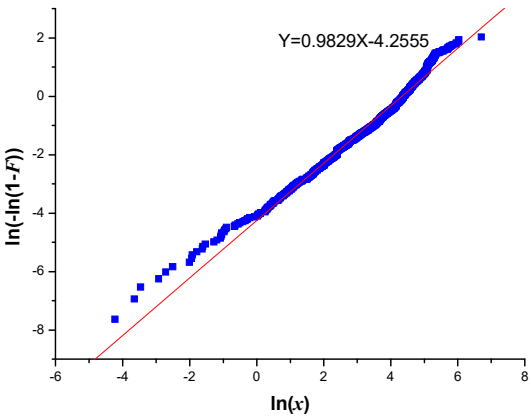

$h_i = 0.8$ m

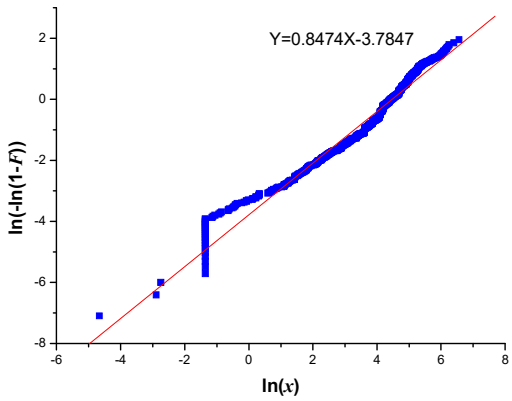

$h_i = 0.9$ m

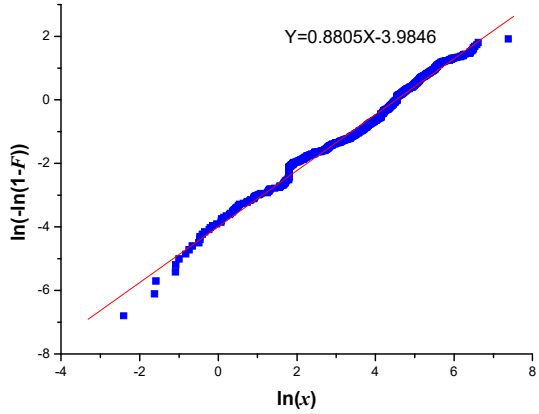

h_i = 1.0 m

Fig. 6.3 Probability plot of ice-induced stress in ridge ice (level ice thickness: 0.2 m–1.0 m).

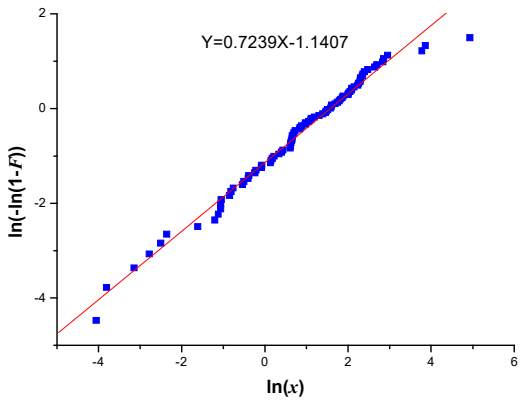

h_i = 0.2 m

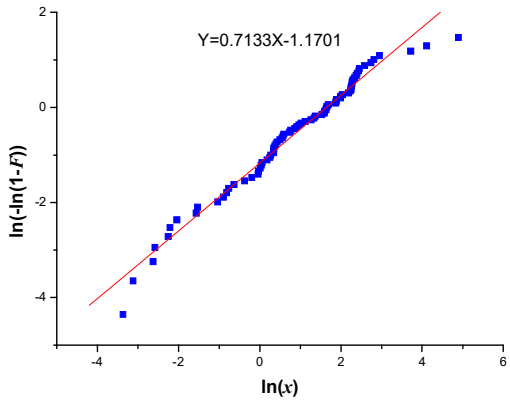

h_i = 0.3 m

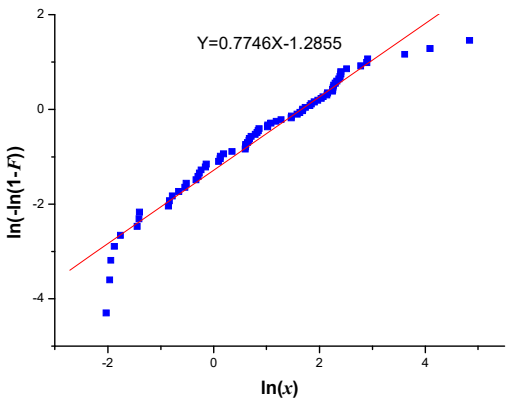

h_i = 0.4 m

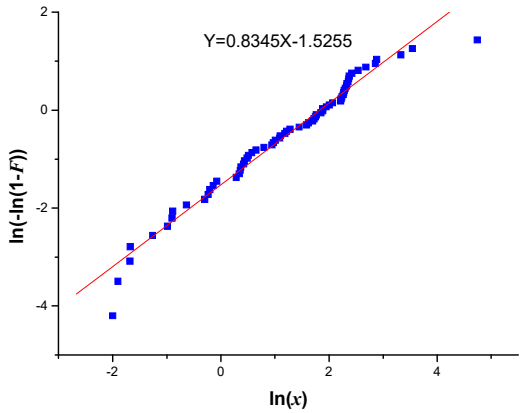

h_i = 0.5 m

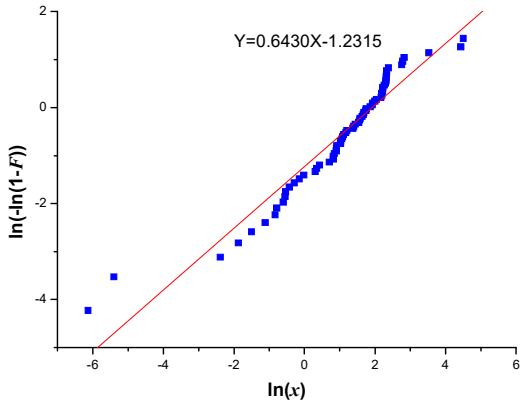

$h_i = 0.6$ m

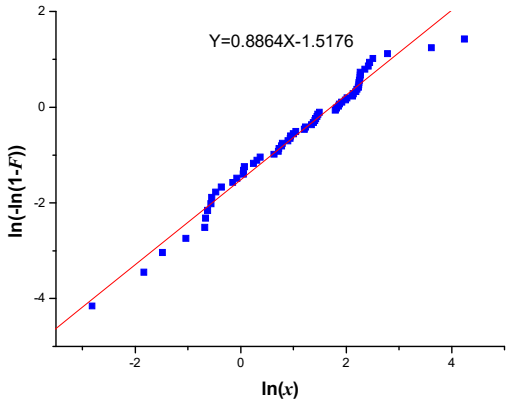

$h_i = 0.7$ m

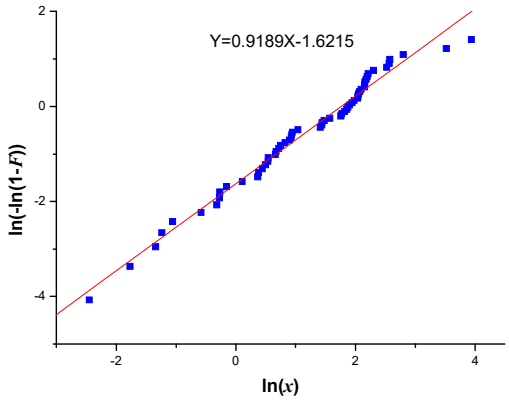

$h_i = 0.8$ m

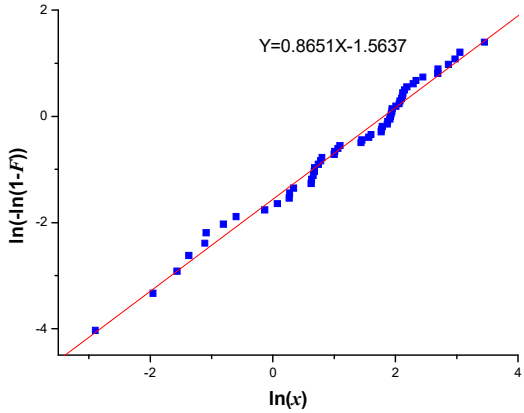

$h_i = 0.9$ m

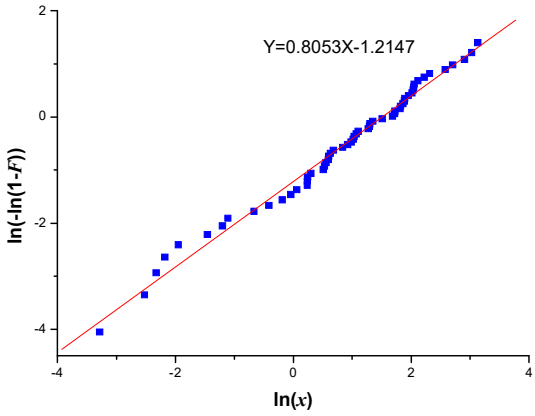

$h_i = 1.0$ m

Fig. 6.4 Probability plot of ice-induced stress in pack ice of 20% ice coverage (ice thickness: 0.2 m–1.0 m).

From these figures, it is clear that the discretized data points in different ice types form nearly a straight line, which means the stress amplitude is reasonable to be modeled with a Weibull distribution. The shape parameters of ice stress distributions in level ice and pack ice are identical to those of ice-induced loads, whereas different values are observed in ridge ice. It is for the reason that the load height can be assumed to be constant in level ice and pack ice, and consequently, according to Eq. (6.1) the shape

parameters of load and stress are of the same magnitude and the scale parameters are proportional to a certain factor. Nevertheless, the load height in ridge ice is time-varying, and thus these relationships cannot be found.

6.2.2.2 Calculation result of fatigue damage

In this study, the parameters of the S–N curve for base metal in the air or with cathodic protection [77] are used, given as m = 4.0, and K = 1.0E+15.117. Fatigue damage accumulates D_j of ice thickness from 0.2 m to 1.0 m in various ice types. The constants needed for the fatigue calculation are presented in Table 6.2. The travel distance per year is assumed to be 2500 nm. The calculation result of fatigue damage in level ice, ridge ice and pack ice are respectively presented in Tables 6.3, 6.4 and 6.5.

Table 6.2 Fatigue calculation constants

Frame Spacing s	0.35 m
Span of Frame l_f	1.5 m
Section Modulus Z	267 cm^3
Boundary Condition m_0	5.0
S–N curve parameter, K	1.0E+15.117
S–N curve parameter, m	4.0

Table 6.3 Fatigue damage calculation in level ice

h_i	$P(h_i)$	N_0/year	p	q	D_j
0.2	0.164	189638	1.1183	13.5645	6.35040E-05
0.3	0.332	283909	0.9794	19.6655	0.000883977
0.4	0.307	211833	1.1620	42.4227	0.005628186
0.5	0.129	75393	1.1725	46.8537	0.002857927
0.6	0.025	12579	1.0646	52.2409	0.001199854
0.7	2.143E-3	969	1.0142	59.8616	0.000209715
0.8	8.302E-5	34	0.9783	76.4713	2.43908E-05
0.9	1.431E-6	0.5367	0.8629	70.9104	6.76203E-07
1.0	1.091E-8	3.79E-03	0.9024	114.2924	2.32053E-08

Table 6.4 Fatigue damage calculation in ridge ice

h_i	$P(h_i)$	N_0/year	p	q	D_j
0.2	0.164	173016	0.9775	3.2265	3.95234E-07
0.3	0.332	258412	0.7072	6.7743	0.000158615
0.4	0.307	192579	0.6976	26.0364	0.029729759
0.5	0.129	68451	0.8526	39.2752	0.008899489
0.6	0.025	11570	0.9016	54.3172	0.003635926
0.7	2.143E-3	884	1.0242	64.8095	0.000248194
0.8	8.302E-5	31	0.9829	75.8926	2.09405E-05
0.9	1.431E-6	0.4886	0.8474	87.0297	1.60577E-06
1.0	1.091E-8	3.44E-03	0.8805	92.3255	1.07156E-08

Table 6.5 Fatigue damage calculation in pack ice

(1) 10% ice coverage

h_i	$P(h_i)$	N_0/year	p	q	D_j
0.2	0.164	786	0.7918	3.3606	1.00440E-08
0.3	0.332	1175	0.7984	3.3084	1.31305E-08
0.4	0.307	877	0.9991	3.6794	2.96330E-09
0.5	0.129	311	0.7340	4.1171	1.79739E-08
0.6	0.025	53	0.8141	4.2476	1.35249E-09
0.7	2.143E-3	4	0.8754	4.6222	8.19651E-11
0.8	8.302E-5	0.1409	0.7748	4.6955	8.30705E-12
0.9	1.431E-6	2.22E-03	0.5333	4.8092	1.27383E-11
1.0	1.091E-8	1.57E-05	0.8261	4.8914	6.30746E-16

(2) 20% ice coverage

h_i	$P(h_i)$	N_0/year	p	q	D_j
0.2	0.164	8197	0.7239	4.8344	1.03095E-06
0.3	0.332	12257	0.7133	5.1573	2.31531E-06
0.4	0.307	9147	0.7746	5.2574	8.49382E-07
0.5	0.129	3245	0.8345	6.2207	3.14094E-07
0.6	0.025	548	0.6430	6.7881	9.70347E-07
0.7	2.143E-3	42	0.8864	5.5409	1.61103E-09
0.8	8.302E-5	1.470	0.9189	5.8400	5.40737E-11
0.9	1.431E-6	2.32E-02	0.8651	6.0951	1.56277E-12
1.0	1.091E-8	1.64E-04	0.8053	4.5198	5.92351E-15

(3) 30% ice coverage

h_i	$P(h_i)$	N_0/year	p	q	D_j
0.2	0.164	15218	0.9815	7.2178	8.48720E-07
0.3	0.332	22756	0.9053	6.8903	1.79983E-06
0.4	0.307	16982	0.9506	7.1663	1.12822E-06
0.5	0.129	6024	0.9460	6.7353	3.22438E-07
0.6	0.025	1017	0.8711	6.1904	6.92764E-08
0.7	2.143E-3	78	0.7841	6.7592	1.76908E-08
0.8	8.302E-5	2.729	0.8485	7.0318	3.78316E-10
0.9	1.431E-6	4.30E-02	0.9741	6.9861	2.20767E-12
1.0	1.091E-8	3.04E-04	0.9195	6.4396	1.64552E-14

(4) 40% ice coverage

h_i	$P(h_i)$	N_0/year	p	q	D_j
0.2	0.164	15132	0.8768	9.7824	6.12254E-06
0.3	0.332	22627	0.8378	9.9088	1.36717E-05
0.4	0.307	16885	0.9344	11.6762	8.85838E-06
0.5	0.129	5990	0.8676	10.9352	4.09591E-06
0.6	0.025	1011	0.8553	9.4513	4.30323E-07
0.7	2.143E-3	77	0.8767	9.1746	2.42318E-08
0.8	8.302E-5	2.713	0.7868	8.0485	1.20530E-09
0.9	1.431E-6	4.28E-02	0.9586	8.1392	4.47835E-12
1.0	1.091E-8	3.02E-04	0.8431	7.8893	6.98283E-14

(5) 50% ice coverage

h_i	$P(h_i)$	N_0/year	p	q	D_j
0.2	0.164	11599	0.8069	16.5599	7.43184E-05
0.3	0.332	17345	0.8251	14.8127	5.91460E-05
0.4	0.307	12944	0.8186	13.3221	3.08308E-05
0.5	0.129	4592	0.9002	12.4627	4.04526E-06
0.6	0.025	775	0.8496	11.2642	7.00472E-07
0.7	2.143E-3	59	0.8437	10.2900	3.93874E-08
0.8	8.302E-5	2.080	0.8924	9.5828	6.81288E-10
0.9	1.431E-6	3.28E-02	0.8663	10.6717	2.05763E-11
1.0	1.091E-8	2.32E-04	0.8566	8.6274	6.76029E-14

(6) 60% ice coverage

h_i	$P(h_i)$	N_0/year	p	q	D_j
0.2	0.164	7880	0.7706	25.3100	0.000411969
0.3	0.332	11784	0.7518	25.3778	0.000781076
0.4	0.307	8794	0.8467	19.5522	7.41306E-05
0.5	0.129	3119	0.7818	20.6406	6.33434E-05
0.6	0.025	527	0.7283	18.7029	1.39788E-05
0.7	2.143E-3	40	0.8859	14.9346	8.20436E-08
0.8	8.302E-5	1.413	0.7959	13.4707	4.45733E-09
0.9	1.431E-6	2.23E-02	0.8755	13.6131	3.41790E-11
1.0	1.091E-8	1.57E-04	0.8402	11.3742	1.61393E-13

The values of calculated annual fatigue damage in level ice, ridge ice and pack ice are 1.087×10^{-2}, 4.270×10^{-2}, 1.557×10^{-3} respectively.

The accumulation value in ridge ice is greater than that in level ice, because of the high loads imparted by consolidated layer and ridge keels, although the ice impact number in ridge ice is slightly lower than that in level ice.

The fatigue damage in pack ice is smaller than that in level ice. It might be attributed to two factors: firstly, in pack ice fields, the distribution of ice floes is quite scattered, which will result in a remarkable decrease in the impact number between ship and sea ice. Secondly, ice floes in pack ice fields can be pushed away when the ship navigates through, and thus the magnitude of ice-induced loads is relatively lower.

Table 6.6 shows the comparison of fatigue calculation results based on numerical simulations against that based on field data by Suyuthi al et. [37]. The calculation result based on field measurements data is 5.826×10^{-4} [37]. Compared with the case study, the fatigue damage in this study is rather bigger. It might be because the ship model used in the calculation are different, and the values of ice loads in this study are much larger, especially when the ice thickness is relatively high.

Table 6.6 Comparison of numerical fatigue value with Suyuthi al et. [37]

	Sea	Ice condition	Duration	Ship model	Fatigue damage	Maximum local loads
Suyuthi al et. [37]	Arctic Sea	Real sea ice	1 year (2500 nm)	KV Svalbard icebreaker	5.836×10^{-4}	< 500 KN
Present study	Baltic Sea	Level ice	1 year (2500 nm)	Xuelong icebreaker	1.087×10^{-2}	1000-2000 KN
Present study	Baltic Sea	Ridge ice	1 year (2500 nm)	Xuelong icebreaker	4.270×10^{-2}	1000-2000 KN
Present study	Baltic Sea	Pack ice	1 year (2500 nm)	Xuelong icebreaker	1.557×10^{-3}	500-1000 KN

With the knowledge of proportions that different ice types account for in an ice region, the total fatigue damage can be calculated as an accumulation of the fatigue contribution in a certain ice type times the corresponding proportion.

$$D = P_{level} D_{level} + P_{ridge} D_{ridge} + P_{pack} D_{pack} \tag{6.17}$$

6.3 Summary

A probabilistic fatigue damage assessment of a transverse frame due to ice actions has been elaborated. The conversion from ice loads into ice stress can be made using structural beam theory. A Weibull model is useful to represent the stress amplitudes in different ice conditions. The shape parameters are identical between loads and stress in level ice and pack ice, however, different values are observed in ridge ice. According to ice data and a proper S-N curve, fatigue damage can be estimated based on the Palmgren–Miner's rule. The calculated fatigue value in level ice is lower than that in ridge ice, whereas higher than that in pack ice. To evaluate fatigue damage in an actual sea ice trial, numerical methods as combinations of simulation models, including level ice, ridge ice, pack ice, etc., can be adopted.

Chapter 7

Conclusions and Future Work

7.1 Conclusions

The present research deals with fatigue damage estimation based on numerical simulations in various ice conditions. In earlier studies, the evaluation of fatigue damage caused by ice-induced loads has been mostly conducted using field measurements, which are usually considerably limited and incomplete. Compared with the field measurements, ice conditions and ship hull can be easily varied in a numerical simulation. It is useful to complement the lack of ice load data in some regions, or to predict the fatigue life for new structural components or new ship routes. Ships navigating in ice-covered waters can encounter widely diverse ice conditions, that include pack ice, level ice, ridged ice, etc. The present thesis focuses on the numerical procedures developed to obtain the time history of ice-induced loads in these ice types, and estimates the fatigue damage based on the simulated results of ice loads.

The main contributions of the present work are summarized for each chapter as follows:

1) A general background on fatigue damage due to ice actions is addressed. As well, reviews of numerical models in level ice, ridge ice, pack ice and fatigue damage calculation cases are given respectively. Moreover, the objectives and organizations in relation to this study are discussed.

2) Ship motions are solved using a step-by-step numerical integration method (Newmark-beta method). Calculation formulas for external forces and moments, such as propeller and rudder forces, hydrodynamic forces, fictitious Euler forces and ice submergence forces are introduced. What's more, the coupling problem between ship motions and excitation forces is settled by iteration.

3) A semi-empirical numerical procedure is developed to model the continuous-mode icebreaking process in level ice in 6 DOFs. The repeating cycles of contact, crushing, and bending are assumed to constitute a continuous breaking process.

- Continuous ice loading processes can be well reproduced by the simulation program. Generally, ice loads in thicker ice conditions are higher, and show more irregularity. The mean values of ice loads are much lower than the peak values.
- Taking account of the larger scale of ship model used in this study, the present

numerical global ice loads and *h–v* curve seem reasonable with comparison against the related numerical results published by Su.

- The global ice loads and ship performance tend to be stable as the ship travels deep into ice sheet, and not significantly affected by the initial conditions.
- The fitted line of simulated ice resistance shows good agreement with that computed by Lindqvist empirical formula.
- Icebreaking pattern has a great effect on the ice loads, which might induce higher loads in thinner ice plate.
- Local ice-induced loads are sensitive to ice thickness and initial speed.
- The local load peaks can be modeled as a Weibull distribution. The shape parameters of the Weibull model representing numerical ice loads process agree well with statistical results of field measurement data.

4) Probabilistic ice fields are generated according to the statistical distributions of ridge heights and spacings. A modified Rankine's plasticity model is applied to achieve the keel loads, considering effects of ship movement and inertia force of ice accumulation in front of the ship bow. Modelling of interaction between ship and consolidated layer resembles that in level ice.

- For low ice thickness, the pure ice ridge force dominates, whereas for high ice thickness, the ice load induced by breaking the consolidated layer dominates
- Ice ridges can engender high loads levels, causing the ship speed to slow dramatically when sometimes rams might have to be required.
- Considering the different dimensions of ship models, the numerical load values transiting into a single ice ridge are of the same order of magnitude as the model test results.
- The present numerical values of mean speeds in various ice thickness agree well with those found from Kuuliala's study.
- The simulated local ice-induced loads are comparable to measurements published in the report of ARCDEV project.
- Keel effect is not important for local frame loads, even though keel loads contribute greatly to global ice loads.
- A Weibull model is useful to represent the local load peaks in ridge ice, although some deviations exist in cases of low ice thickness. The shape parameters are reasonable compared to field measurements.

5) A 2D DEM numerical model is developed for simulating the interaction between drifting ice floes and a moving ship. The ice floes are represented as hundreds of circular disks with random sizes and positions. Both the ship–ice collisions and ice–ice contacts are modeled, and a viscous-elastic rheology is applied at contacts.

- Ship navigation process through pack ice can be well reproduced by this procedure, and the numerical results are comparable to those simulated in earlier studies of Ji and Daley.
- A nearly steady speed can be achieved during transiting process, although still with fluctuations
- Ice resistance generally increases with the increasing ice thickness and concentration, although deviation found in some cases.
- The simulated local frame loads can be modeled according to the Weibull distribution, and the shape parameters are consistent with those obtained based on field measurements.

6) A probabilistic fatigue damage assessment of a transverse frame due to ice actions has been elaborated. The structural fatigue stress is found using structural beam theory. According to ice condition data and a proper S-N curve, fatigue damage can be estimated based on the Palmgren–Miner's rule.

- Numerical stress amplitudes can be modeled according to Weibull distribution. The shape parameters are identical between loads and stress in level ice and pack ice, however, different values are observed in ridge ice.
- The calculated fatigue value in level ice is lower than that in ridge ice, whereas higher than that in pack ice.
- With the knowledge of proportions that different ice types account for in an ice region, the total fatigue damage can be calculated as an accumulation of the fatigue contribution in a certain ice type times the corresponding proportion.

7.2 Future works

The following interesting and important issues in relation to the topic of this thesis are identified as possible subjects for further studies.

1) Although the proposed numerical model in level ice could address the ship motions in 6 DOFs, however, the contact detection between ship hull and ice plate is performed using a point-in-polygon computer geometric method. The case that the approximately vertical mid-ship hull contacts the bottom surface of ice sheet first due to the effect of roll movement, cannot be settled with this 2D method. Moreover, contact surface is assumed to remain flat during crushing, which cannot reflect the accurate contact area. Therefore, a 3D contact detection model should be developed in the future research, in order to incorporate all kinds of contact cases, and calculate the crushing force with higher accuracy.

2) A modified Rankine plasticity model is applied to achieve the keel loads in ridged ice fields, which regards ship hull as vertical and ridge surface as horizontal. Nevertheless, in practice, the contacts between ship hull and ice ridge are extremely

complicated because of the inclined surface of both hull and ridge. A 3D model could be developed to account for the tilted ship–ridge interaction, and some geometric algorithms should be carried out to predict the moving process of ice blocks. Another attempt to estimate the ridge breaking ability of ships by 3D DEM simulations could also be performed.

3) The developed numerical approach in pack ice fields is conducted by a simple 2D DEM model, in which ice floes are represented as simplest circular disks. A further realistic random polygons can be used to model the ice pieces in the future works. In addition, the 2D method in this study assumes the disks only move translationally in horizontal plane. Further studies should be carried out to investigate a 3D model, taking account of rotation and layering of ice floes.

4) In this study, structural beam theory is adopted to evaluate the ice-induced fatigue stress, which is merely a sort of linear transformation from load into stress. In order to obtain more accurate stress, a structural analysis based on FEM could be done in the future studies. Furthermore, a spectral-based method could be attempted to access the fatigue life of structural components. Proper ice condition data and S–N data at low temperature are also necessary.

5) Aside from level ice, ridge ice and pack ice, other ice types appear in ice-covered waters, such as channel ice and ice in wave, which should be involved in the fatigue damage calculation. Numerical models of ship operating in these ice conditions need to be developed in the future works.

ACKNOWLEDGEMENTS

First and foremost, I would like to express my deepest appreciation and sincerest gratitude to my advisors, Prof. Naoki Osawa and Assist. Prof. Junji Sawamura for their support during my PhD study. Prof. Naoki Osawa has given me many instructive and expertise suggestions on my thesis, and offered me many helps in the last three years. Assist. Prof. Junji Sawamura has provided continuous guidance and invaluable advice for my research. I appreciate all his contributions of time and ideas to make my PhD experience productive. The present work would not have been possible without the consistent instruction and support from him.

I owe a special debt of gratitude to my thesis committee: Prof. Masahiko Fujikubo, Assoc. Prof. Kazuhiro Iijima, and Prof. Akihisa Konno, not only for their insightful and constructive comments and encouragement, but also for the hard questions which incented me to widen my research from various perspectives.

Special thanks to Dr. Hanyang Gong, for her help with the reference papers which I needed, and her valuable suggestions on the research about ship–ice interaction model in ridge ice.

I deeply thank all the wonderful and friendly laboratory members. Special thanks go to Mr. Kim Hyoil, Mr. Keisuke Suga, Mr. Kensuke Imaki, Mr. Takaya Shiraishi, Ms. Shino Katayama, Ms. Phyo Myat Kyaw and everyone who had been very kind to help me whenever I was in difficulties. Their precious friendships are worth collection attentively for a lifetime.

I am grateful to all friends who accompany me and contribute to my meaningful life during the past three years. Many thanks to Ms. Jianping Ma, Ms. Ranwen Lu and Mr. Yingzhe Wang, for their help in my daily life and all the good memories we shared together. I gratefully thank Mr. Kang Ren, one of my best friends for ten years, for his support, encouragement and also some advice on my research.

I would like to warmly acknowledge the financial support of China Scholarship Council and Osaka University for my PhD research and living in Japan.

Last but definitely not the least, my appreciation and thanks would go to my beloved family, for their consistent and unconditional support, encouragement, and forever love. They give me the world.

REFERENCES

[1] G. W. Timco, K. Croasdale, and B. Wright, "An overview of first-year sea ice ridges," PERD/CHC report, 2000.

[2] E. Enkvist, "On the Ice Resistance Encountered by Ships Operating in The Continuous Mode of Icebreaking," Report No.24, The Swedish Academy of Engineering Science in Finland. Helsinki, Finland, 1972.

[3] J. W. Lewis, F. W. DeBord, and V. A. Bulat, *Resistance and Propulsion of Ice-Worthy Ships*. Transactions of SNAME, USA, 1982.

[4] G. Lindqvist, "A straightforward method for calculation of ice resistance of ships," in *Proceedings of the 10th International Conference on Port and Ocean Engineering under Arctic Conditions*, pp. 722–735, 1989.

[5] K. Riska, M. Wilhelmson, K. Englund, and T. Leiviska, "Performance of merchant vessels in ice in the Baltic," Technical Report 52, Helsinki University of Technology, Ship Laboratory, 1997.

[6] K. Izumiyama, H. Kitagawa, K. Koyama, and S. Uto, "A numerical simulation of ice–cone interaction," in *Proceedings of the 11th IAHR International Symposium on Ice*, pp. 188–199, 1992.

[7] S. Wang, *A dynamic model for breaking pattern of level ice by conical structures*. PhD thesis, Department of Mechanical Engineering, Helsinki University of Technology, Finland, 2001.

[8] D. T. Nguyen, A. H. Sørbø, and A. J. Sørensen, "Modelling and Control for Dynamic Positioned Vessels in Level Ice," in *Proceedings of 8th Conference on Manoeuvring and Control of Marine Craft* (*MCMC'2009*), pp. 229–236, 2009.

[9] J. Sawamura, K. Riska, and T. Moan, "Numerical simulation of breaking patterns in level ice at ship's bow," in *The Nineteenth International Offshore and Polar Engineering Conference*, International Society of Offshore and Polar Engineers, 2009.

[10] L. Zhou, B. Su, K. Riska, and T. Moan, "Numerical simulation of moored structure station keeping in level ice," *Cold Regions Science and Technology*, vol. 71, pp. 54–66, 2012.

[11] B. Su, K. Riska, and T. Moan, "A numerical method for the prediction of ship performance in level ice," *Cold Regions Science and Technology*, vol. 60, pp. 177–188, 2010

[12] B. Su, K. Riska, and T. Moan, “Numerical simulation of local ice loads in uniform and randomly varying ice conditions,” *Cold Regions Science and Technology*, vol. 65(2), pp. 145–159, 2011.

[13] X. Tan, B. Su, K. Riska, and T. Moan, “A six-degrees-of-freedom numerical model for ice–ship interaction,” *Cold Regions Science and Technology*, vol. 92, pp. 1–16, 2013.

[14] X. Tan, K. Riska, and T. Moan, “Effect of dynamic bending of level ice on ship's continuous-mode icebreaking,” *Cold Regions Science and Technology*, vol. 106, pp. 82–95, 2014.

[15] Q. Zhou, H. Peng, and W. Qiu, “Numerical investigations of ship–ice interaction and maneuvering performance in level ice,” *Cold Regions Science and Technology*, vol. 122, pp. 36–49, 2016.

[16] R. Lubbad, and S. Løset, “A numerical model for real-time simulation of ship–ice interaction,” *Cold Regions Science and Technology*, vol. 65, pp. 117–127, 2011.

[17] M. Lau, K. P. Lawrence, and L. Rothenburg, “Discrete element analysis of ice loads on ships and structures,” *Ships and Offshore Structures*, vol. 6(3), pp. 211–221, 2011.

[18] A. Keinonen, *An analytical method for calculating the pure ridge resistance encountered by ships in first year ice ridges*. PhD thesis, Helsinki University of Technology, Ship Hydrodynamics Laboratory, 1979.

[19] M. Mellor, “Ship resistance in thick brash ice,” *Cold Regions Science and Technology*, vol. 3(4), pp. 305–321, 1980.

[20] S. Malmberg, *Om fartygs fastkling i is* (*Of ship’s becoming beset in ice*). Master thesis, Helsinki University of Technology, 1983.

[21] B. Sand, and G. Horrigmoe, “Simulations of ice ridge forces on conical structures,” in *The Eleventh International Offshore and Polar Engineering Conference*, International Society of Offshore and Polar Engineers, 2001.

[22] Q. Hisette, A. Alekseev, and J. Seidel, “Discrete Element Simulation of Ship Breaking Through Ice Ridges,” in *The Twenty-seventh International Ocean and Polar Engineering Conference*, pp. 1401–1409, International Society of Offshore and Polar Engineers, 2017.

[23] H. Gong, A. Polojärvi, and J. Tuhkuri, “Preliminary 3D DEM Simulations on Ridge Keel Resistance on Ships,” in *Proceedings of the 24th International Conference on Port and Ocean Engineering under Arctic Conditions*, 2017.

[24] E. H. Hansen, and S. Loset, “Modelling floating offshore units moored in broken ice: model description,” *Cold Regions Science and Technology*, vol. 29, pp. 97–106, 1999.

[25] E. H. Hansen, and S. Loset, “Modelling floating offshore units moored in broken

ice: comparing simulations with ice tank tests," *Cold Regions Science and Technology*, vol. 29, pp. 107–119,1999.

[26] E. B. Karulin, and M. M. Karulina, "Numerical and physical simulations of moored tanker behavior," *Ships and Offshore Structures*, vol. 6(3), pp. 179–184, 2011.

[27] J. Dai, and H. Peng, "Discrete Element Modelling of Pack Ice Interaction with Floating Structures," in *ASME 2015 34th International Conference on Ocean, Offshore and Arctic Engineering*, American Society of Mechanical Engineers, 2015.

[28] S. Ji, Z. Li, C. Li, and J. Shang, "Discrete element modeling of ice loads on ship hulls in broken ice fields," *Acta Oceanologica Sinica*, vol. 32(11), pp. 50–58, 2013.

[29] C. Daley, S. Alawneh, D. Peters, B. Quinton, and B. Colbourne, "GPU modeling of ship operations in pack ice," in *International Conference and Exhibition on Performance of Ships and Structures in Ice*, pp.20–23, 2012.

[30] C. Daley, S. Alawneh, D. Peters, and B. Colbourne, "GPU-event-mechanics evaluation of ice impact load statistics," in *OTC Arctic Technology Conference*, Offshore Technology Conference, 2014.

[31] D. Zhan, D. Agar, M. He, D. Spencer, and D. Molyneux, "Numerical simulation of ship maneuvering in pack ice," in *ASME 2010 29th International Conference on Ocean, Offshore and Arctic Engineering*, American Society of Mechanical Engineers, 2010.

[32] D. Zhan, and D. Molyneux, "3-Dimensional Numerical Simulation of Ship Motion in Pack Ice," in *ASME 2012 31st International Conference on Ocean*, *Offshore and Arctic Engineering*, pp. 407–414, American Society of Mechanical Engineers, 2012.

[33] A. Konno, and T. Mizuki, "Numerical Simulation of Pre-Sawn Ice Test of Model Icebreaker Using Physically Based Modeling," in *Proceedings of the 18th IAHR International Symposium on Ice*, 2006.

[34] I. Metrikin, W. Lu, R. Lubbad, S. Løset, and M. Kashafutdinov, "Numerical Simulation of a Floater in a Broken-Ice Field: Part I—Model Description," in *ASME 2012 31st International Conference on Ocean*, *Offshore and Arctic Engineering*, American Society of Mechanical Engineers, 2012.

[35] I. Metrikin, A. Borzov, R. Lubbad, and S. Løset, "Numerical Simulation of a Floater in a Broken-Ice Field: Part II—Comparative Study of Physics Engines," in *ASME 2012 31st International Conference on Ocean*, *Offshore and Arctic Engineering*, American Society of Mechanical Engineers, 2012.

[36] S. Zhang, R. Bridges, and J. Tong, "Fatigue Design Assessment of Ship Structures Induced by Ice Loading-An introduction to the ShipRight FDA ICE Procedure," in *The Twenty-first International Offshore and Polar Engineering Conference*,

International Society of Offshore and Polar Engineers, 2011.

[37] A. Suyuthi, B. J. Leira, and K. Riska, "Fatigue damage of ship hulls due to local ice-induced stresses," *Applied Ocean Research*, vol. 42, pp. 87–104, 2013.

[38] M. R. Hwang, T. K. Lee, D. H. Kang, and Y. S. Suh, "A study on ice-induced fatigue life estimation based on measured data of the ARAON," in *The Twenty-sixth International Ocean and Polar Engineering Conference*, International Society of Offshore and Polar Engineers, 2016.

[39] T. I. Fossen, *Handbook of Marine Craft Hydrodynamics and Motion Control*. John Wiley & Sons, Ltd., Chichester, UK, 2011.

[40] N. M. Newmark, "A method of computation for structural dynamics," *Journal of Engineering Mechanics Division*, vol. 85(3), pp. 67–94, 1959.

[41] V. Bertram, *Practical Ship Hydrodynamics*. Butterworth-Heinemann, Oxford, UK, 2000.

[42] O.M. Faltinsen, *Sea Loads on Ships and Offshore Structures*. Cambridge University Press, Cambridge, UK, 1990.

[43] K. Riska, *Ship-ice interaction in ship design: theory and practice*. Encyclopedia of Life Support Systems (EOLSS), Developed under the Auspices of the UNESCO, Eolss Publishers, Oxford, UK, 2010.

[44] P. J. Schneider, and D. H. Eberly, *Geometric Tools for Computer Graphics*. Morgan Kaufmann Publishers, San Francisco, USA, 2002.

[45] F. P. Preparata, and M. I. Shamos, *Computational Geometry: An Introduction*. Springer Verlag, New York, 1985.

[46] T. J. Sanderson, *Ice Mechanics: Risks to Offshore Structures*. Graham and Trotman, London 272, 1988.

[47] D. M. Masterson, R. M. W. Frederking, B. Wright, T. Kärnä, and W. P. Maddock, "A Revised Ice Pressure–Area Curve," in *Proceedings of the 19th International Conference on Port and Ocean Engineering under Arctic Conditions*, 2007.

[48] A. Palmer, "Ice forces and ice crushing," in *Proceedings of the 11th International Conference on Port and Ocean Engineering under Arctic Conditions*, 1991.

[49] V. I Kashtelyan, "Priblizhennoye opredeleniye usiliy, razrushayushchikh ledyanoy pokrov (An approximate determination of forces which break up a floating ice plate)," *Problemy Arktiki i Antarktiki*, Vol. 5, pp. 31–37, 1960.

[50] A. D. Kerr, "The bearing capacity of floating ice plates subjected to static or quasi-static loads," *Journal of glaciology*, vol. 17(76), pp. 229–268, 1976.

[51] P. Varsta, "On the mechanics of ice load on ships in level ice in the Baltic Sea," Publications 11, Technical Research Centre of Finland, Espoo, Finland, 1983.

[52] P. Kujala, M. Suominen, and K. Riska, "Statistics of ice loads measured on MT Uikku in the Baltic," in *Proceedings of the 20th International Conference on Port and Ocean Engineering Under Arctic Conditions*, 2009.

[53] I. I. Gringorten, "A plotting rule for extreme probability paper." *Journal of Geophysical Research*, vol. 68(3), pp. 813–814, 1963.

[54] M. Suominen, and P. Kujala, "Analysis of short-term ice load measurements on board MS Kemira during the winters 1987 and 1988," Technical report, Aalto University, 2010.

[55] A. Suyuthi, B. J. Leira, and K. Riska, "Statistics of local ice load peaks on ship hulls," *Structural Safety*, vol. 40, pp. 1–10, 2013.

[56] L. Strub-Klein, and D. Sudom, "A comprehensive analysis of the morphology of first-year sea ice ridges," *Cold Regions Science and Technology*, vol. 82, pp. 94–109, 2012.

[57] B. Wright, J. Hnatiuk, and A. Kovacs, "Sea ice pressure ridges in the Beaufort sea," in *Proceedings of the 5th IAHR International Symposium on Ice*, 1978.

[58] K. V. Hoyland, A. Jensen, P. Liferov, J. Heinonen, K.U. Evers, S. Loset, and M. Määtänen, "Physical Modelling of First-Year Ice Ridges-Part I: Production, Consolidation and Physical Properties," in *Proceedings of the 16th International Conference on Port and Ocean Engineering Under Arctic Conditions*, 2001.

[59] E. Bailey, R. Taylor, and K. Croasdale, "Mechanics of ice rubble over multiple scales," in *ASME 2015 34th International Conference on Ocean*, *Offshore and Arctic Engineering*, American Society of Mechanical Engineers, 2015.

[60] D. La Prairie, M. Wilhelmson, and K. Riska, "A transit simulation model for ships in Baltic ice conditions," Technical Report, Helsinki University of Technology, Ship Laboratory, 1995.

[61] V. Kotovirta, R. Jalonen, L. Axell, K. Riska, and R. Berglund, "A System for Route Optimization In Ice-Covered Waters," *Cold Regions Science and Technology*, vol. 55(1), pp. 52–62, 2009.

[62] M. Leppäranta, "On the structure and mechanics of pack ice in the Bothnian Bay," Technical report 248, Finnish Marine Research, 1981.

[63] W. D. Hibler, W. F. Weeks, and S. J. Mock, "Statistical aspects of sea-ice ridge distributions," *Journal of Geophysical Research*, vol. 77(30), pp. 5954–5970, 1972.

[64] J. Knappett, *Craig's soil mechanics*. London, UK Spon Press, 2012.

[65] D. Myland, "Ships Breaking Through Sea Ice Ridges," *International Journal of Offshore and Polar Engineering*, vol. 24(01), pp. 28–34, 2014.

[66] L. Kuuliala, P. Kujala, M. Suominen, and J. Montewka, "Estimating operability of

ships in ridged ice fields," *Cold Regions Science and Technology*, vol. 135, pp. 51–61, 2017.

[67] M. Leppäranta, *The Drift of Sea Ice*, Springer, 2005.

[68] A. Keinonen, "Ship Performance and Resistance in Ice Ridges," in *The Seventh Graduate School on Ships and Structures in Ice*, 1983.

[69] ARCDEV Arctic Demonstration Voyage, "Final Public Report of the ARCDEV Project," European Commission Under the Transport RTD Programme of the Fourth Framework Programme, 1998.

[70] S. Løset, "Discrete element modelling of a broken ice field—Part I: model development," *Cold regions science and technology*, vol. 22(4), pp. 339–347, 1994.

[71] Y. T. Feng, and D. R. J. Owen, "A 2D polygon/polygon contact model: algorithmic aspects," *Engineering Computations*, vol. 21(2/3/4), pp. 265–277, 2004.

[72] L. Timokhov and D. Kheisin, *Dynamics of sea ice*. Leningrad: Hydrometeoizdat, 1987.

[73] Finnish Maritime Administration, *Ice class regulations 2008 (Finnish-Swedish ice class rules)*, Bulletin 10 / 10.12.2008, 2008.

[74] R. Bridges, K. Riska, and S. Zhang, "Fatigue assessment for ship hull structures navigating in ice regions," In *Proceedings of the Icetech*, 2006.

[75] P. Kujala, *On the Statistics of Ice Loads on Ship Hull in the Baltic*. PhD thesis, Ship Laboratory, Helsinki University of Technology, Finland, 1994.

[76] A. P. Worby, C. A. Geiger, M. J. Paget, M. L. Van Woert, S. F. Ackley, and T. L. DeLiberty, "Thickness distribution of Antarctic sea ice," *Journal of Geophysical Research: Oceans*, 113(C5), 2008.

[77] Det Norsk Veritas, *Fatigue assessment of ship structures*, Classification Notes No. 30.7, 2010.